

## Potentiometry on organic semiconductor devices

**Citation for published version (APA):**

Charrier, D. S. H. (2009). *Potentiometry on organic semiconductor devices*. [Phd Thesis 1 (Research TU/e / Graduation TU/e), Applied Physics and Science Education]. Technische Universiteit Eindhoven.  
<https://doi.org/10.6100/IR652483>

**DOI:**

[10.6100/IR652483](https://doi.org/10.6100/IR652483)

**Document status and date:**

Published: 01/01/2009

**Document Version:**

Publisher's PDF, also known as Version of Record (includes final page, issue and volume numbers)

**Please check the document version of this publication:**

- A submitted manuscript is the version of the article upon submission and before peer-review. There can be important differences between the submitted version and the official published version of record. People interested in the research are advised to contact the author for the final version of the publication, or visit the DOI to the publisher's website.
- The final author version and the galley proof are versions of the publication after peer review.
- The final published version features the final layout of the paper including the volume, issue and page numbers.

[Link to publication](#)

**General rights**

Copyright and moral rights for the publications made accessible in the public portal are retained by the authors and/or other copyright owners and it is a condition of accessing publications that users recognise and abide by the legal requirements associated with these rights.

- Users may download and print one copy of any publication from the public portal for the purpose of private study or research.
- You may not further distribute the material or use it for any profit-making activity or commercial gain
- You may freely distribute the URL identifying the publication in the public portal.

If the publication is distributed under the terms of Article 25fa of the Dutch Copyright Act, indicated by the "Taverne" license above, please follow below link for the End User Agreement:

[www.tue.nl/taverne](http://www.tue.nl/taverne)

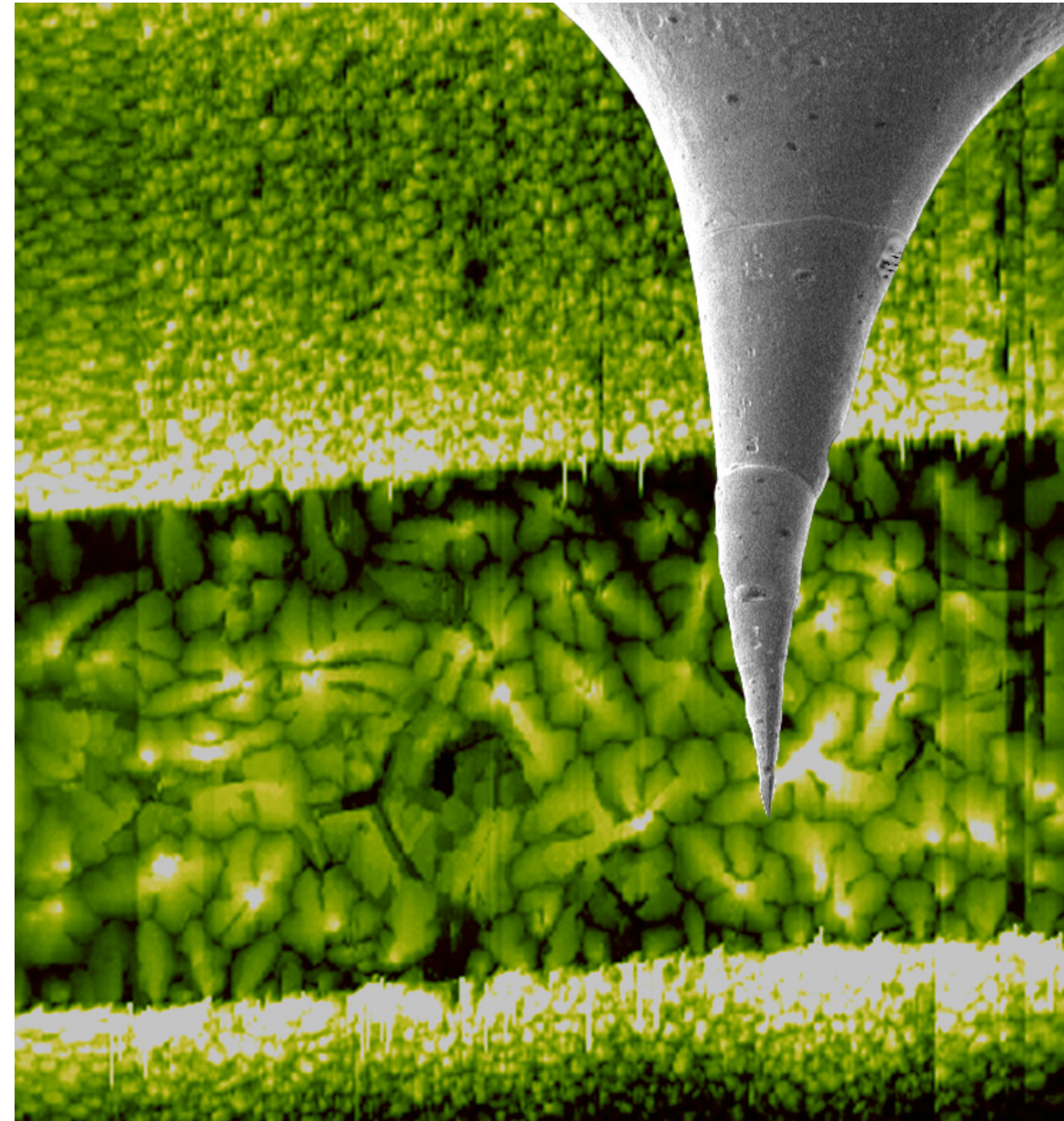
**Take down policy**

If you believe that this document breaches copyright please contact us at:

[openaccess@tue.nl](mailto:openaccess@tue.nl)

providing details and we will investigate your claim.

# Potentiometry on organic semiconductor devices



Dimitri Charrier

Potentiometry on organic semiconductor devices

Dimitri Charrier

## Uitnodiging

tot het bijwonen van de  
openbare verdediging  
van mijn proefschrift

Potentiometry on  
organic  
semiconductor  
devices

op dinsdag 29  
september 2009  
om 16 uur.

De promotie vindt plaats in  
het auditorium van de  
Technische Universiteit  
Eindhoven

Na afloop van de plechtigheid  
vindt er een receptie plaats  
waarvoor u ook van harte  
bent uitgenodigd.

Dimitri Charrier  
06-21626931  
dscharrier@free.fr

# Potentiometry on organic semiconductor devices

PROEFSCHRIFT

ter verkrijging van de graad van doctor  
aan de Technische Universiteit Eindhoven,  
op gezag van de rector magnificus,  
prof.dr.ir. C.J. van Duijn,  
voor een commissie aangewezen  
door het College voor Promoties  
in het openbaar te verdedigen  
op dinsdag 29 september 2009 om 16.00 uur

door

**Dimitri Sébastien Hans Charrier**

geboren te Privas, Frankrijk

Dit proefschrift is goedgekeurd door de promotor:

prof.dr.ir. R.A.J. Janssen

Copromotor:

dr.ir. M. Kemerink

A catalogue record is available from the Eindhoven University of Technology Library.

Charrier, Dimitri Sébastien Hans

Potentiometry on organic semiconductor devices / by Dimitri Charrier. - Eindhoven: Technische Universiteit Eindhoven, 2009. Proefschrift.

ISBN 978-90-386-2004-6

NUR 926

Trefwoorden: organische halfgeleiders / organische veld-effect transistor / potentiometrie / Kelvin scanning probe microscoop / modelleren / recombinatie breedte / overdracht functie / scanning tunneling microscoop / actuator

Subject headings: organic semiconductors / organic field effect transistor / potentiometry / scanning Kelvin probe microscope / modeling / recombination width / transfer function / scanning tunneling microscope / actuator

Printed by Gildeprint Drukkerijen in Enschede

This research was financially supported by NanoNed (NanoNed is the Dutch nanotechnology initiative by the Ministry of Economic Affairs).

# Contents

<b>1. Introduction</b>	<b>1</b>
1.1 Context	1
1.2 Materials used in this thesis	2
1.3 Organic field effect transistors	3
1.4 Scanning Kelvin probe microscopy	11
1.5 Scanning Kelvin probe microscopy on oFETs	14
1.6 Scopes of the thesis	17
1.7 References and notes	18
<b>2. Real versus measured surface potentials in scanning Kelvin probe microscopy</b>	<b>23</b>
2.1 Introduction	23
2.2 Experimental scanning Kelvin probe microscope results	24
2.3 Simulation of scanning Kelvin probe microscope	27
2.4 Conclusion	33
2.5 Materials and methods	33
2.6 References and notes	34
<b>3. On the width of the recombination zone in organic light emitting field effect transistors</b>	<b>37</b>
3.1 Introduction	37
3.2 Analytical model of recombination width	38
3.3 Recombination width of a NiDT field-effect transistor	42
3.4 Conclusion	44
3.5 References and notes	44
<b>4. Bimolecular recombination in ambipolar organic field effect transistors</b>	<b>47</b>
4.1 Introduction	47
4.2 Materials and methods	49
4.3 Results and discussion	51
4.4 Conclusion	54
4.5 References and notes	54

<b>5. Scanning tunneling microscopy via the accumulation layer of <i>p</i>-type organic field effect transistors</b>	<b>57</b>
5.1 Introduction . . . . .	57
5.2 Materials and methods . . . . .	58
5.3 Results and discussion . . . . .	60
5.4 Conclusion . . . . .	65
5.5 References and notes . . . . .	65
<b>6. Giant out-of-plane ambient actuation of poly(3,4-ethylenedioxythiophene) : poly(styrenesulfonate) thin films</b>	<b>67</b>
6.1 Introduction . . . . .	67
6.2 Results . . . . .	68
6.2.1 Out-of-plane actuation at the anode . . . . .	68
6.2.2 Depletion and morphology changes in the channel . . . . .	71
6.2.3 Lack of volume conservation . . . . .	73
6.2.4 Reversibility of actuation . . . . .	74
6.2.5 Role of humidity in actuation and stability . . . . .	76
6.2.6 Surface potential measurements . . . . .	78
6.3 Discussion . . . . .	80
6.4 Conclusion . . . . .	85
6.5 Experimental . . . . .	85
6.6 References and notes . . . . .	86
<b>Summary</b>	<b>89</b>
<b>Samenvatting</b>	<b>93</b>
<b>Acknowledgements</b>	<b>97</b>
<b>Curriculum Vitae</b>	<b>101</b>

## Chapter 1

# Introduction

### 1.1 Context

The field of organic electronics is rapidly maturing, as witnessed by, e.g., hundreds of organic transistors performing complex logical operations<sup>1,2</sup> and organic materials forming the heart of both rigid and flexible displays, based on various operational principles like e-ink<sup>3</sup> and fluorescence or phosphorescence.<sup>4</sup> Nevertheless, many important questions are still open and will likely require novel or improved measurement schemes to be answered. The goal of this chapter is to give a short introduction on the functioning and metrology of an important organic device, the organic field effect transistor (oFET), which is the building block of logical circuits.

Recent years showed an intense and competitive research on measuring and modeling the functionality of oFETs. The most commonly used technique, measurement of the transfer and output curves, suffers from the drawback that what goes on in the channel has to be deduced from the behavior at the terminals. In other words, there is a 'black box' problem, which evidently asks for ways to probe the operational channel. To physically access the channel, which is typically a few to a few tens of microns long, scarce technical options are available. Far-field optical methods are limited in lateral resolution by diffraction effects to at best half the wavelength used. Near-field optical techniques may have a sub-100 nm resolution, but do so at the cost of much weaker signals. In all cases, the most relevant information is electrical in nature, and the associated optical signatures are often very small but measurable. E.g. charge modulation spectroscopy can be used to probe the excitation at the dielectric/semiconductor interface through a transparent layer.<sup>5</sup> Also Stark shifts can also be measured in situ and yield information on (local) electric fields.<sup>6,7</sup> In comparison, scanning probe microscopy (SPM)

is usually far more accurate in terms of lateral resolution, which may be below the single atom level, depending on conditions, sample and probing scheme. Among the wide variety of SPM techniques, the most logical choice is scanning Kelvin probe microscopy or SKPM. This technique allows one to measure the local potential inside the oFET channel, which can quantitatively, and in principle directly, be compared to transport models. Moreover, SKPM is a standard option on most modern atomic force microscopes (AFM).

Not surprisingly, SKPM is nowadays the most commonly used tool for looking at the channel potential. However, the SKPM technique still suffers from limitations in resolution due to the intrinsic capacitive coupling between the entire probe, of which the tip apex is only the extreme part, and the entire device. As a consequence the measured surface potential needs deepened analysis before quantitative, or even qualitative, comparison to theoretical predictions can be made. In this thesis, such an analysis was performed which enabled us to use the SKPM technique to investigate the physics of oFETs.

## 1.2 Materials used in this thesis

The list of organic semiconductor materials that is used in the active layer of oFETs is virtually endless, and still growing. Of these, we focused on two prototypical materials, shown in Fig. 1 a) and b). Pentacene (PC) is taken as reference molecule because of its ubiquity and its high performance in *p*-type oFETs, see Fig. 1 a). The high performance in this context refers to the relatively high mobility of holes in the crystalline phase, which can be as high as  $1.4 \text{ cm}^2/\text{Vs}$ .<sup>8</sup> Thermally evaporated films are typically polycrystalline, with the grain boundaries reducing the mobility to typically  $0.1 \text{ cm}^2/\text{Vs}$ .<sup>9</sup> Nickel dithiolene (NiDT) is a small metalorganic dye that was recently found to show ambipolar behavior in oFETs on  $\text{SiO}_2$  substrates under ambient conditions, see Fig. 1 b).<sup>10</sup> Poly(3,4-ethylenedioxythiophene) : poly(styrenesulfonate) (PEDOT:PSS) (Fig. 1 c)) is a doped small-bandgap semiconductor and hence not applicable as active layer in an oFET, but it is the most likely candidate for replacing metal electrodes in all-plastic

and transparent devices because of its plasticity, transparency and its quasi metallic conductivity. Despite the fact that it is one of the most used materials in the field, it can still show very surprising behavior, as shown in Chapter 6.

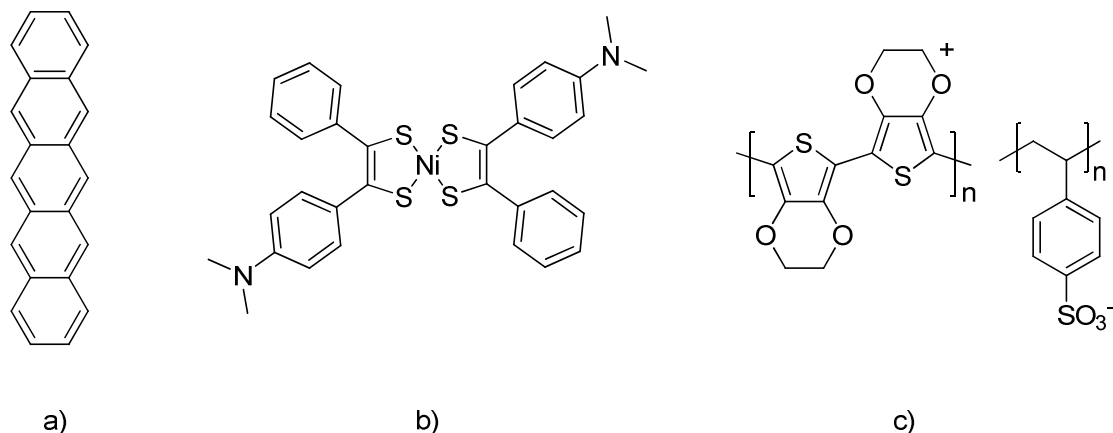


Fig. 1. Materials studied in this thesis, a) pentacene (PC), b) nickel dithiolenes (NiDT), and c) poly(3,4-ethylenedioxythiophene):poly(styrenesulfonate) (PEDOT:PSS).

### 1.3 Organic field effect transistors

One of the reasons motivating the effort put into improving performance and reliability of oFETs is the hope for lower production costs than Si technology as soon as large area devices can be produced in a roll-to-roll way. Another advantage may be the higher plasticity and robustness than amorphous Si (a-Si).

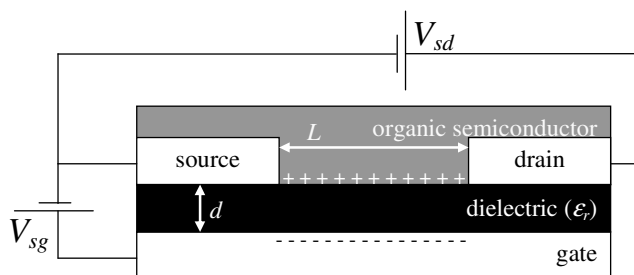


Fig. 2. Cross-section drawing of a typical organic field effect transistor (oFET), with an organic semiconductor, electrically driven by the source, drain, and gate electrodes. Positive charge (hole) accumulation occurs throughout the channel when  $|V_{sg}| > |V_{sd}|$  and  $V_{sg} < 0$ .

A potential application then is the backplane of active matrix displays, where organic circuitry should replace the already existing flexible a-Si. An oFET is formed by an organic semiconductor with three electrical terminals: a gate, a source and a drain, see Fig. 2. The space between source and drain, called the channel, has a length  $L$  and a width  $W$ . While the organic semiconductive layer is in direct contact with the source and drain electrodes, the gate electrode is connected to it via a dielectric spacer ( $\epsilon_r > 1$ ) of thickness  $d$ . When a gate bias is applied, charges accumulate at the organic semiconductor/dielectric interface, like in a capacitor. Since the carriers are mobile in the semiconductor, the channel becomes conductive. Then, at finite source-drain bias, a source-drain current will flow. The threshold voltage  $V_{th}$  defines the gate voltage at which a conductive channel between source and drain is formed.

The carrier density in the organic layer increases with the source-gate bias  $V_{sg}$  allowing an increasing source-drain current  $I_{sd}$  to flow at a fixed source-drain bias  $V_{sd}$ . When  $V_{sg} - V_{th} > V_{sd}$ , the transistor is in the linear regime. In this regime, the charge density in the accumulation layer is roughly constant, and the current is linear in both  $V_{sg}$  and  $V_{sd}$ .<sup>11</sup> When  $|V_{sg} - V_{th}| < |V_{sd}|$ , the transistor is in the saturation regime, which is characterized by  $I_{sd}$  being independent of  $V_{sd}$ . A depletion region is present at the drain side of the channel in this regime.

The field effect mobility  $\mu$  ( $\text{cm}^2/\text{Vs}$ ) is one of the main performance indicators of oFETs and can be extracted by means of transport measurements, e.g. via measurement of the transfer characteristic  $I_{sd}(V_{sg})$ . The mobility  $\mu$  in the linear regime can be written as  $\mu_{lin} = d / (\epsilon_0 \epsilon_r W^2) dI_{sd} / dV_{sg}$  where  $\epsilon_0 = 8.854 \times 10^{-12}$  F/m. In organic single crystals, mobilities above  $10 \text{ cm}^2/\text{Vs}$  have been achieved,<sup>8,12</sup> which surpass mobilities in amorphous silicon thin film transistors. The single crystals have the advantage to show the intrinsic mobilities while polycrystalline materials show a lower mobility ( $\sim 0.1 \text{ cm}^2/\text{Vs}$ ) that is limited by the grain boundaries. In that case, advanced four-point-probe measurements can still enable one to estimate the intrinsic mobility.<sup>9</sup> For polymer materials that show good ordering properties, the highest reported mobilities are around  $0.2 \text{ cm}^2/\text{Vs}$  for poly(3-hexylthiophene) (P3HT)<sup>13</sup> and  $0.72 \text{ cm}^2/\text{Vs}$  for poly(2,5-bis(3-alkylthiophen-2-yl)thieno[3,2-b]thiophene) (PBTTT).<sup>14</sup> In strongly disordered polymers like most poly(*p*-phenylene vinylene) (PPV) derivatives, mobilities are typically  $10^{-5}$

$\text{cm}^2/\text{Vs}$  and below.<sup>15</sup> To date, the record mobility in disordered polymers was obtained at  $0.85 \text{ cm}^2/\text{Vs}$  for poly{[*N,N'*-bis(2-octyldodecyl)-naphthalene-1,4,5,8-bis(dicarboximide)-2,6-diyl]-alt-5,5'-(2,2'-bithiophene)} (P(NDI2OD-T2)).<sup>16</sup>

The first polycrystalline (polythiophene) oFETs, as described by Tsumura *et al.*,<sup>17</sup> showed a relatively poor performance. Nevertheless they are very suited to gain understanding of the typical physical limitations of oFETs: contact resistance, gate dielectric problems, and a low intrinsic mobility. Below, these three issues will be discussed in more detail.

The *contact resistance*, i.e. the injection barrier between the metallic electrode and the semiconductor can be estimated by measuring the longitudinal resistance as a function of channel length. The resistance is then obtained by extrapolating the device resistance to channel length equal zero. Typically found contact resistances for sexithiophene (6 T) on Au electrodes are in the range of  $10^5$ - $10^6 \Omega$ .<sup>18</sup>

*Gate dielectric.* Since the flexible substrates are in state of development, most organic transistors use  $\text{SiO}_2$  ( $\epsilon_r = 3.9$ ) on highly doped Si as gate dielectric. This is, amongst others, due to an easier patterning of the metallic electrodes than on a polymer dielectric, although some organic dielectrics have a good dielectric constant and show low leakage currents to the gate.<sup>19</sup> The morphology of gate dielectric and the interfacial chemical interaction with the semiconductor play an important role in the apparent mobility. Hysteresis, charge trapping, and nonzero threshold voltages are commonly attributed to the gate dielectric. A lot of effort is given to improve the transport at the dielectric/semiconductor interface, which enabled a gain by several orders of magnitude in mobility.<sup>20</sup> Note that some free-dielectric ( $\epsilon_r = 1$ ) oFETs have also been realized, using vacuum as a spacer.<sup>21</sup> They have the advantage to circumvent the charge trapping at the organic semiconductor/dielectric interface.

*Low mobility.* From conjugated polymers to small molecules, the recent strategy to obtain high mobility and solution-processed oFETs is in general to have soluble materials, highly microcrystalline layers, and a high density of states. Sirringhaus<sup>22</sup> gives an overview of such high performance materials. The regioregular P3HT reaches high field effect mobilities  $0.1$ - $0.3 \text{ cm}^2/\text{Vs}$ .<sup>23,24</sup> Several routes allow small molecules to be solution processible such as precursor routes, side chain substitution and liquid crystalline

molecule. For instance, pentacene precursors showed mobilities from 0.01 to 0.8  $\text{cm}^2/\text{Vs}$ <sup>25,26</sup> after thermal conversion at 150-200 °C. The high density of states is obtained with well-designed materials leading to strong  $\pi$ - $\pi$  interchain interactions. The correlation between transport properties and morphology is often completed by X-ray diffraction giving molecular packing within the randomly oriented microcrystals.

### Channel potentials in unipolar oFETs

Before turning to the potential profile in the channel of an oFET, it is interesting to have a look at the potential on top of the gate dielectric in absence of the organic semiconductor. Like for the complete oFET, the potential profile is determined by the geometry and the boundary conditions set by  $V_{sg}$  and  $V_{sd}$ . However, the absence of the active layer prevents screening charges to enter the channel region. Hence, away from the source and drain contacts the potential is dominated by the (unscreened) gate potential. Fig. 3 shows 2D finite element calculations (COMSOL<sup>27</sup>) of such a potential profile.

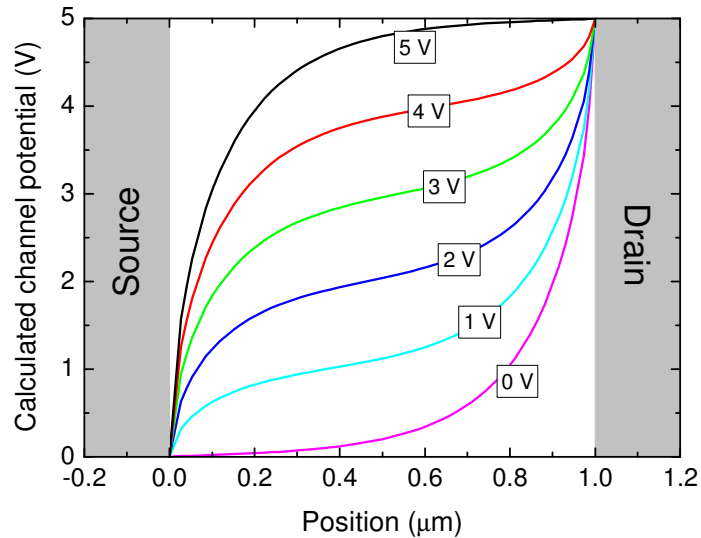


Fig. 3. Calculated channel potentials on the gate dielectric for a channel without semiconductor ( $d = 200$  nm,  $\epsilon_r = 3.9$ ,  $V_{sd} = 5$  V and  $L = 1$   $\mu\text{m}$ ) for different  $V_{sg}$ .

## 1. Introduction

As soon as a hole or electron transporting material is present, the gate bias causes accumulation of charges in the lowest unoccupied molecular orbital (LUMO) (for  $V_{sg} > 0$ ) or highest occupied molecular orbital (HOMO) (for  $V_{sg} < 0$ ) of the organic semiconductor. Making approximations,<sup>11</sup> such as the gradual channel approximation, no contact resistance, no depletion, no diffusion and assuming an exponential density of states, it is possible to calculate the analytical channel potential  $V(x)$  (Eq. (1)). The gradual channel approximation supposes the electric field induced by the gate is much larger than the field induced by the electrodes. In practice, this is valid for large channel lengths. In oFETs, an exponential density of states is commonly assumed<sup>28</sup> and has the advantage to be analytically treatable. From the current continuity equation one then obtains:

$$V(x) = V_{sg} - V_{th} + \left\{ (-V_{sg} + V_{th})^\beta - x/L [(-V_{sg} + V_{th})^\beta - (V_{sd} - V_{sg} + V_{th})^\beta] \right\}^{1/\beta} \quad (1)$$

with  $\beta = 2T_0/T$ .  $T_0$  is a measure of the width of the exponential density of states and  $T$  is the absolute temperature.

In case depletion regions are present, analytical calculations are no longer possible and numerical models are required to calculate the channel potential. Within our group a program (DriftKicker) has been developed which enables numerical calculations of channel and surface potentials (the difference will be discussed below) on basis of the coupled drift/diffusion (Eq. (2)) and Poisson (Eq. (3)) equations. In 1 dimension, these are:

$$j_{total} = j_{el} + j_{hole}$$

$$j_{el} = qn\mu_{el}E + qD_{el} \frac{dn}{dx} \quad (2)$$

$$j_{hole} = qp\mu_{hole}E - qD_{hole} \frac{dp}{dx}$$

$$\frac{dE}{dx} = -\frac{d^2V}{dx^2} = \frac{\rho}{\epsilon_0\epsilon_r} \quad (3)$$

where  $j_{el}$  and  $j_{hole}$  are respectively the electron and hole current densities,  $q$  is the positive elementary charge,  $n$  and  $p$  are the electron and hole densities,  $\mu_{el}$  and  $\mu_{hole}$  the electron and hole mobilities,  $D_{el}$  and  $D_{hole}$  the diffusion coefficients. The electric field  $E$  and the potential  $V$  are related to the carrier concentration  $\rho$  via the Poisson equation (3).

The input of DriftKicker calculations are the geometrical and physical parameters of the sample. Taking realistic values of a single crystal transistor, Fig. 4 shows the potential in the channel for different  $V_{sg}$ .

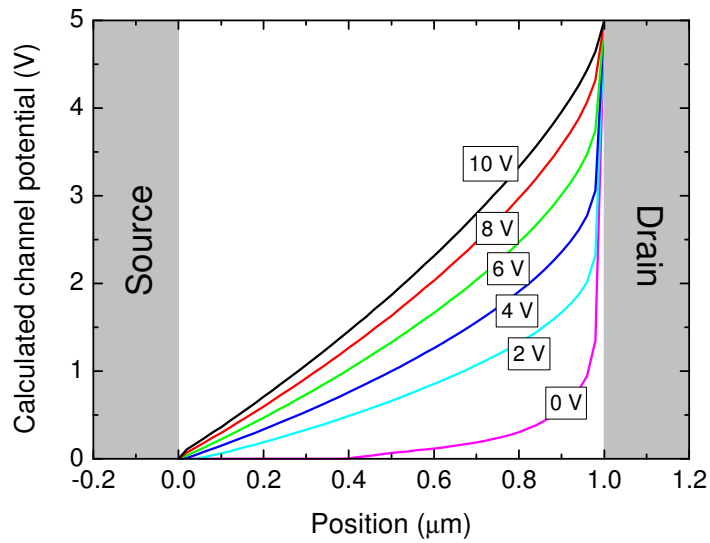


Fig. 4. Calculated channel potentials in the accumulation layer in the channel of a  $n$ -type oFET ( $d = 200$  nm,  $\epsilon_r = 3.9$ ,  $V_{sd} = 5$  V,  $L = 1$   $\mu\text{m}$  and  $\mu_e = 1$   $\text{cm}^2/\text{Vs}$ ) for different  $V_{sg}$ .

At  $V_{sg} = 0$ , the differences between Fig. 3 and 4 are relatively small which can be understood by the insulating behavior of the semiconductor in absence of an accumulation layer. At  $0 \text{ V} < V_{sg} < 5 \text{ V}$  (saturation), the differences are more pronounced, with the potential dropping mainly in the region where the semiconductor is depleted, i.e. in the vicinity of the drain. At  $V_{sg} > 5 \text{ V}$ , an accumulation layer is present in the entire channel, and a more gradual channel potential results. Note that this potential can be described by Eq. (1) by setting  $\beta = 1$ .

### Channel potentials in ambipolar oFETs

Under appropriate source-gate and source-drain biases, the electrostatic potential allows the presence of both holes and electrons. In general, this regime is reached when the gate potential is in between the source and drain potentials, i.e. for electron (hole) accumulation near the source (drain), e.g. see Fig. 5. Materials allowing the presence of mobile carriers of both signs are called ambipolar.

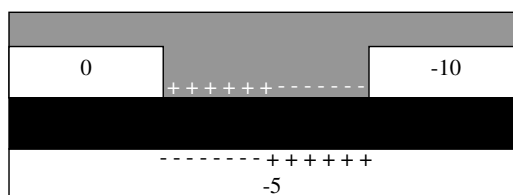


Fig. 5. Distribution of charges at  $V_{sd} = -10 \text{ V} < V_g - V_{th} = -5 \text{ V} < 0$  leading to a *pn* junction in the oFET channel.

Recently, it turned out that many conjugated polymers allow ambipolar transport provided a proper gate dielectric is used.<sup>29</sup> Previously, the main limitation for ambipolar transport in oFETs was due to an *n*-type problem encountered at the  $\text{SiO}_2$ /semiconductor interface. Fourier-transform infrared (FTIR) spectrometry on operational oFETs showed that SiOH groups quench the *n*-channel oFET activity due to the formation of  $\text{SiO}^-$ . Consequently, it could be shown that the electron trapping due to hydroxyl groups can be overcome by using a hydroxyl-free gate dielectric like BCB (a divinyltetramethylsiloxane-bis(benzocyclobutene) derivative), thereby allowing ambipolar transport.<sup>29</sup> The NiDT system discussed in Chapters 3 and 4 has the special property that it shows stable ambipolar behavior on the  $\text{SiO}_2$  dielectric under ambient conditions.<sup>30</sup>

The transport of holes and electrons in ambipolar devices can quantitatively be described by the drift and diffusion equations introduced above and using the continuity equation:

$$\begin{aligned}
dp/dt &= -e^{-1} dj_{hole} / dx + G - R \\
dn/dt &= -e^{-1} dj_{electron} / dx + G - R
\end{aligned} \tag{4}$$

$G$  and  $R$  are the generation and recombination rates, respectively. At the border between  $n$ - and  $p$ -type regions, electron and hole currents meet. A consequence of having both carriers in close proximity is bimolecular recombination of electrons and holes. In the bimolecular-recombination plasma,  $R$  is usually assumed to be described by a Langevin-type equation:

$$R = \gamma p \tag{5}$$

where  $\gamma$  is the recombination prefactor. For Langevin recombination,  $\gamma$  is given by  $\gamma = q(\mu_{el} + \mu_{hole}) / \epsilon_0 \epsilon_r$ . Here,  $q$ ,  $\mu_{el}$  and  $\mu_{hole}$  are the elementary charge, and the electron and hole mobility, respectively. Using the same approximations as for unipolar oFETs and the current continuity equation, the ambipolar channel potential can be analytically calculated under the assumption of a zero recombination zone width, i.e.  $R$  is infinite.<sup>11</sup>

$$V(x) = V_{sg} - V_{th} - \left\{ (V_{sg} - V_{th})^{\beta_c} - x/x_0 (V_{sg} - V_{th})^{\beta_c} \right\}^{1/\beta_c} \tag{6}$$

for  $0 < x < x_0$

$$V(x) = V_{sg} - V_{th} + \left\{ (V_{sd} - V_{sg} + V_{th})^{\beta_h} - (L-x)(L-x_0)^{-1} (V_{sd} - V_{sg} + V_{th})^{\beta_h} \right\}^{1/\beta_h} \tag{7}$$

for  $x_0 < x < L$

where  $x_0$  is the  $pn$  meeting point. The infinitely large recombination rate  $R$  leads to a steplike increase in the potential which is, obviously, in reality not the case. Numerical calculations are needed to take a finite  $R$  into account.

To summarize, the drift/diffusion, Poisson, and Langevin equations are the theoretical basement to predict physical observables such as the channel potential. From surface potential measurements by SKPM, the width of the recombination zone in light-emitting oFETs (LEFETs) can be measured and compared to model predictions.

Recent Monte-Carlo studies were conducted to reconsider the recombination factor (also called rate constant) used in Langevin-type recombination. As discussed by Groves *et al.*,<sup>31</sup> deviations are reported between the exact Langevin value and measured values for the recombination factor  $\gamma$ . Differences amounting up to several orders of magnitude are reported.

So far, the only physical observables that have been used to study the recombination in LEFETs are the surface potential and the light emitted from the exciton recombination at the p-n interface described above. LEFETs based on ambipolar single crystals have been reported but no further studies on their recombination width are reported. Ambipolar polymers FETs are reported to emit visible<sup>32</sup> or infrared<sup>33,34</sup> light. Although optical techniques enable the direct reading of the light intensity, the lateral accuracy is intrinsically limited by the wavelength. Moreover, in thin polymer films, waveguiding effects by the layer may cause an apparent broadening of the recombination zone. No optical reconstruction has been reported to deduce the real light emission width.<sup>32,35</sup>

As discussed above, surface potential measurements are expected to give a much higher lateral resolution. SKPM was used to measure the surface potential on an ambipolar OFET based on NiDT.<sup>11</sup> In Chapters 3 and 4 these results are analyzed in detail in order to make quantitative statements about the width of the recombination zone and the bimolecular recombination rate.

### 1.4 Scanning Kelvin probe microscopy

The channel potential is the potential located at the dielectric/semiconductor interface while the surface potential is the potential on the semiconductor/vacuum interface. In this chapter, the measurement of the surface potential  $V(x)$  by SKPM is discussed. As mentioned above, the most convenient technique to perform non-contact local potentiometry on organic semiconductors is SKPM. It is a non-destructive method, easily reproducible and possibly functioning in air. The Kelvin probe aims to approach a sharp metallic tip (probe) to a sample at distance  $d$ , as shown in Fig. 6 a).

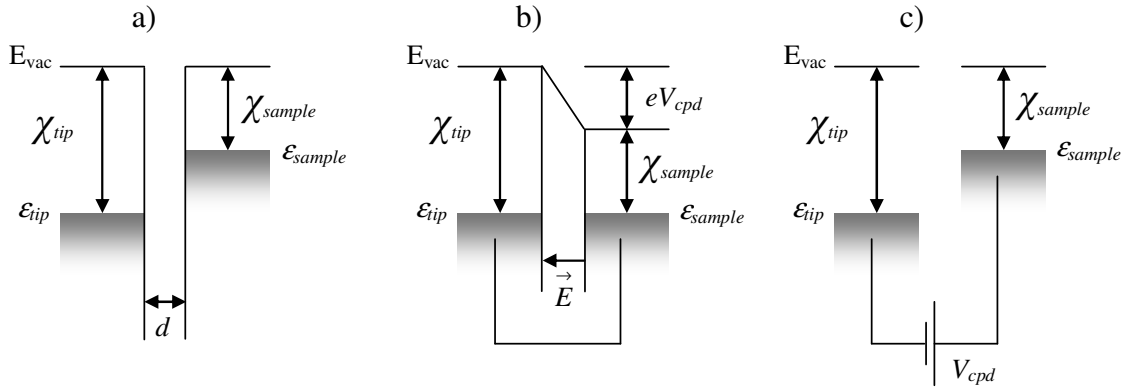


Fig. 6. Schematic of band diagrams of Kelvin probe.  $\chi_{tip}$  and  $\chi_{sample}$  are the work functions of tip and sample,  $\epsilon_{tip}$  and  $\epsilon_{sample}$  are their respective Fermi levels,  $d$  their separating distance.  $V_{cpd}$  is the contact potential difference. a) At proximity, the vacuum levels of tip and sample are aligned. b) At closed tip-sample circuit, their Fermi level are aligned creating a force, in order to nullify that force, the work function difference is applied in the circuit c).

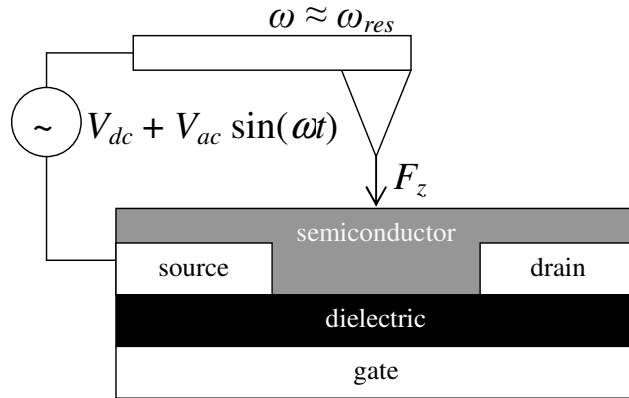


Fig. 7. Schematic of non-contact local potentiometry by SKPM. The local surface potential is deduced by nullifying the electrostatic force  $F_z$  between tip and sample when the condition  $V_{cpd} = V_{dc}$  is fulfilled.

At closed tip-sample circuit, see Fig. 6 b), the work function difference  $eV_{cpd}$  between the tip  $\chi_{tip}$  and sample  $\chi_{sample}$  creates a force  $F = e |\vec{E}| = eV_{cpd} / d = (\chi_{tip} - \chi_{sample}) / d$  between them that depends on the contact

potential difference  $V_{cpd}$ . Applying  $V_{cpd}$  in the circuit, as in Fig. 6 c), the force becomes zero.

In SKPM, a metallic AFM tip scans the sample at a fixed tip-to-sample distance. An AC bias  $V_{ac}$  at frequency  $\omega$  is applied between the tip and the sample in combination with a DC voltage  $V_{dc}$ , see Fig. 7. The force along the normal axis  $Oz$  is given by

$$F_z = -\frac{V^2}{2} \frac{dC}{dz} \quad \text{with } V = V_{dc} + V_{ac} \sin(\omega t) - V_{cpd} \quad \text{where } C \text{ is the total capacity between the}$$

entire tip and the surface and  $V_{cpd}$  is the contact potential difference.  $V_{cpd}$  contains the surface potential  $V(x)$  as  $V_{cpd} = V(x) - \chi_{sample} / e$ . By combining the two expressions, the

force at the resonant frequency becomes  $F_\omega = \frac{dC}{dz} V_{ac} (V_{cpd} - V_{dc})$ . Note that  $F_\omega$  is nullified

for  $V_{cpd} = V_{dc}$ , which is the condition that is sought for by the SKPM feedback system.

The map of  $V_{dc}$  vs. lateral position is usually referred to as the surface potential. The force

$F_\omega$  does not depend on the frequency  $\omega$  which seems to become a non-influencing

parameter. However, the choice of  $\omega$  is crucial for the final results. When a resonance

frequency is used, the sensitivity can be dramatically enhanced. When the 2<sup>nd</sup> harmonic is

used, topographic feedback can simultaneously be done on the ground harmonic, which

allows one to measure topography and surface potential simultaneously. In both cases the

technique is referred to as amplitude modulation (AM) SKPM. Using a frequency far

below the first resonance, the force gradient, instead of the force itself, can be used for

SKPM by having the feedback act on the resulting resonance frequency modulation. This

technique is referred to as frequency modulation (FM) SKPM, and yields a higher spatial

resolution (due to the strong distance dependence of  $d^2C/dz^2$  which reduces undesired

electrostatic coupling) at the cost of a reduced energetic sensitivity as compared to AM-

SKPM. FM-SKPM requires a high Q-factor of the tip resonance, for which reason this

technique is only applicable in vacuum conditions.

For all experiments described in this thesis SKPM measurements were conducted

in air using the AM technique with  $\omega$  at the first resonance. Hence, a two-pass ‘lift mode’

technique was used. In the first pass, the topography is measured by tapping mode (TM)

AFM while the tip remains grounded. In a second pass the tip is tracked at a fixed lift

height over the surface, using the height information obtained in the first pass. In this 2<sup>nd</sup> pass, the surface potential is measured.

The working tip-to-surface distance, i.e. the lift height, of the SKPM affects both resolution and sensitivity. Most AFM tips used in SKPM are made of silicon and are metal coated. Therefore the apex radius is usually not smaller than 10 nm, causing a first limitation to the spatial resolution at which the surface potential can be measured. Next, the cone of the tip and the cantilever also have a capacitive coupling to the surface, further reducing the resolution. A very small cone angle somewhat reduces the electrostatic coupling with the surrounding area, but the final spatial resolution of AM-SKPM is typically 100 nm or worse.

The tip-to-sample distance effect is analytically described in literature only for systems consisting of an apex + cone.<sup>36</sup> In this thesis, we have developed a 3D numerical model that enables to quantitatively predict the SKPM output for any probe, i.e. including cantilever, from a known potential distribution and geometry. The model is successfully compared to SKPM measurements performed on relevant test devices and will be discussed in Chapter 2.

## 1.5 Scanning Kelvin probe microscopy on oFETs

The previous paragraph described the surface potential mapping on metallic surfaces. In a situation where organic layers are sandwiched between a metal electrode and a metallic tip differences arise. On organic surfaces, the capacitive approach is still valid although several effects complicate the interpretation of the measurements. Hudlet *et al.*<sup>37</sup> gave the force expressions of a metallic tip above metallic and semiconductor surfaces. Fig. 8 shows the potential drop in the case of metallic (a) and semiconducting (b) surfaces. Due to the dielectric behavior of non-degenerately doped semiconductors, a potential drop may occur inside the semiconductor. The potential decrease inside the semiconductor can be described by the Debye screening length  $L_D = (\epsilon kT / 2N_D q^2)^{1/2}$  where  $N_D$  is the doping density,  $q$  the elementary charge,  $\epsilon$  the permittivity,  $k = 1.3806 \cdot 10^{-23}$  J/K the Boltzmann constant, and  $T$  the temperature. The potential drop

reflects the bending of both valence and conduction bands, or HOMO and LUMO levels in case of organic semiconductors.

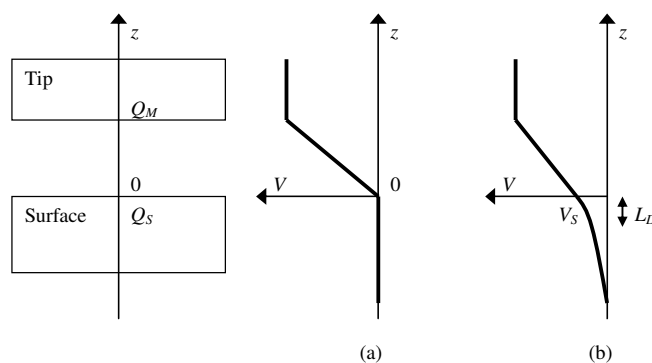


Fig. 8. Potential and charge distribution in the tip-surface system: (a) Metal tip/metal surface case, (b) metal tip/semiconductor surface case, see ref. [37].

As soon as the metallic tip is above an oFET, the whole electrostatic interaction becomes even more complex, so a number of simplifying assumptions is made:

1. The semiconductive layer above the accumulation layer is a perfect insulator, having dielectric properties.
2. The carrier accumulation layer is located near the dielectric and is only a few nanometers thick.
3. The metallic tip has a negligible effect on the field distribution and charge transport in the device.

The first assumption supposes that the active layer acts as a dielectric spacer and avoids the implementation of the Debye length  $L_D$ . For instance, for  $N_D = 10^{15} \text{ cm}^{-3}$  in PPV,<sup>38</sup> the Debye length at room temperature becomes  $L_D \approx 46 \text{ nm}$ , so it is reasonable to treat thin organic layers like a dielectric. Also other effects might cause a problem in measured surface potentials. Let us define  $l_{typ}$  as the size of a feature to be discerned in the potential trace on a polymer film of thickness  $d$ . Then, if  $L_D < d$  and  $l_{typ} < d$  the measured surface potential is smeared out by screening and geometrical (thickness) effects. Hence, the feature size  $l_{typ}$  should be larger than about 100 nm which is the case in this thesis. The validity of the second assumption follows from the calculations in Ref. 18, where the accumulation layer is shown to be around 1 nm thick for  $V_{sg} - V_{th} = 10 \text{ V}$  at

room temperature. The validity of the third assumption was numerically checked with DriftKicker. The physical reason for the lack of effect is that in SPKM the tip is at the potential that minimizes the interaction with the underlying sample; hence the difference with the channel potential in the tip vicinity is small.

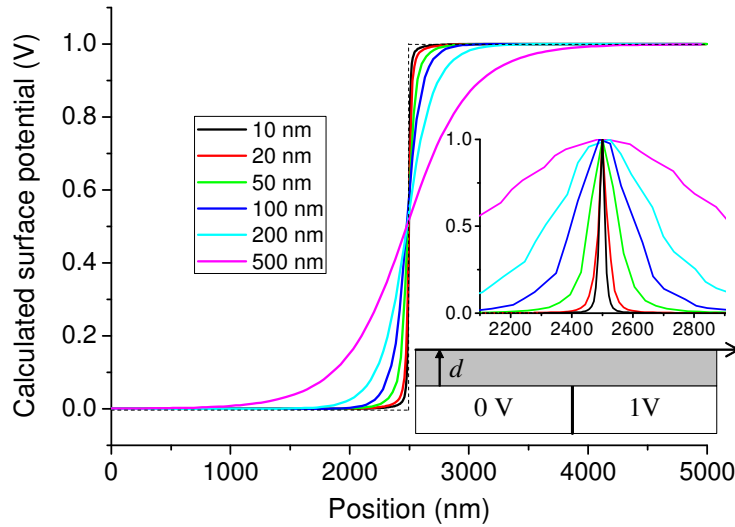


Fig. 9. Dashed line: potential drop located at position  $x = 2500$  nm with  $\Delta V = 1$  V. Continuous lines: calculated surface potentials above polymer layers ( $\epsilon_r = 3$ ) of different thicknesses  $d$ . Inset: first derivative of surface potential. Broadening due to the finite resolution of the SKPM technique has not been accounted for.

Under these three assumptions the potential at the sample surface, i.e. the surface potential, can be numerically calculated using DriftKicker. Note that due to the presence of the dielectric spacer, the surface potential is not identical to the channel potential, as illustrated in Fig. 9. The observed broadening of surface potential does not contain the SKPM tip-convolution effect depending on the layer thickness and lift height (Chapter 4). For a minimal lift height, the convolution is dominant for films thinner than thickness  $\sim 200$  nm.

On operational oFETs, SKPM measurements are reported commonly for unipolar materials.<sup>39,40,41,42,43</sup> So far, only Smits *et al.*<sup>11</sup> reported SKPM measurements on an ambipolar material (NiDT), see Fig. 10. In Ref. 11 the apparent mismatch between the experiments (symbols) and the theoretical prediction (lines) is tentatively attributed to

diffusion currents, electrostatics, and a finite recombination rate. In Chapters 3 and 4 these issues will be discussed in detail.

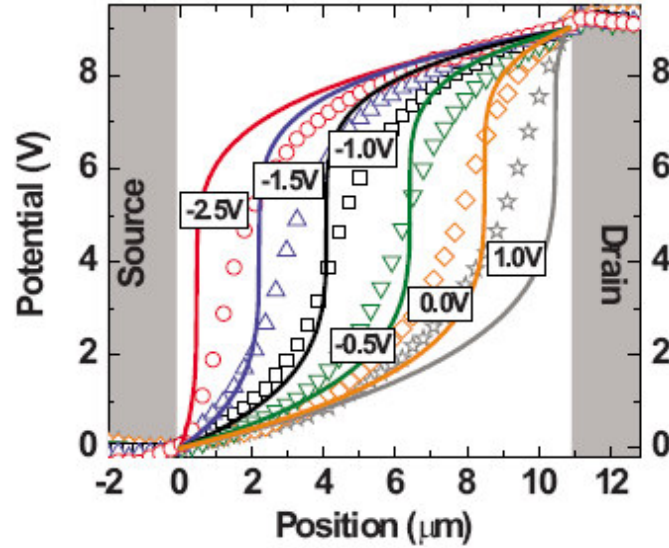


Fig. 10. Theoretical surface potentials of an ambipolar material according to an analytical drift model. Symbols: SKPM measurements above ambipolar oFET for different  $V_{sg}$ , see ref. [11].

### 1.6 Scope of the thesis

As explained above, the AM-SKPM technique suffers from the drawback that experimentally obtained curves do not reflect the true potential profile in the device due to non-local coupling between the probing tip and the device. In this thesis, several approaches are followed to deal with this problem.

In Chapter 2, the experimental SKPM response to a theoretically known surface potential is quantitatively predicted using a numerical 3D finite element method. In particular, the model quantitatively explains the effects of the tip-to-sample distance and the dependence on the orientation of the probing tip with respect to the device. Unfortunately, these numerical calculations require long calculation times.

In Chapter 3, the SKPM response model developed in Chapter 2 is successfully applied to measured channel potentials in an ambipolar oFET. An analytical model for

the recombination profile is derived and used for comparison. Assuming Langevin recombination, the recombination zone width  $W_{rec}$  is found to be given by  $W_{rec} = \sqrt{4.34d\delta}$  with  $d$  and  $\delta$  the gate dielectric and accumulation layer thicknesses, respectively. From this analysis, we find that the actual recombination rate is two orders of magnitude below the value predicted by the Langevin model, yielding  $W_{rec} \sim 0.5 \mu\text{m}$ .

In Chapter 4, a method based on (de)convolution with an experimentally calibrated transfer function containing the electrostatic tip-sample coupling is developed, which also allows reconstructing the real surface potential from a measured SKPM response. Using this method we determined a recombination zone width of again  $0.5 \mu\text{m}$  for a NiDT ambipolar oFET. The (de)convolution methods are more flexible than the finite element method and require negligible calculation times.

In Chapter 5, we aim at implementing a scanning-tunneling microscope-based method, STM potentiometry (STP), to measure potentials with potentially sub-nm resolution. In order to perform STM-potentiometry on operational oFETs in a controlled atmosphere, a dedicated ultra high vacuum STM has been designed and built. Using scanning tunneling spectroscopy, this instrument should also allow a direct measurement of the density of states in the accumulation layer of an oFET. We demonstrate that it is possible to do STM on oFETs provided that an accumulation layer of sufficient conductivity is present in the sample, which is an important step towards STP.

Finally, in Chapter 6 we demonstrate and model a giant out-of-plane actuation under ambient conditions in thin films of the oxidatively doped conjugated polymer blend poly(3,4-ethylenedioxythiophene) : poly(styrenesulfonate) (PEDOT:PSS) spin cast between interdigitated gold electrodes on glass substrates.

## 1.7 References and notes

- [1] A. Dodabalapur, *Materials Today* **9**, 24 (2006).
- [2] E.C.P. Smits, S.G.J. Mathijssen, P.A. van Hal, S. Setayesh, T.C.T. Geuns, K.A.H.A. Mutsaers, E. Cantatore, H.J. Wondergem, O. Werzer, R. Resel, M. Kemerink, S.

Kirchmeyer, A.M. Muzafarov, S.A. Ponomarenko, B. de Boer, P.W.M. Blom, and D.M. de Leeuw, *Nature* **455**, 956 (2008).

[3] B. Comiskey, J.D. Albert, H. Yoshizawa, and J. Jacobson, *Nature* **394**, 253 (1998).

[4] T. Sekitani, H. Nakajima, H. Maeda, T. Fukushima, T. Aida, K. Hata, and T. Someya, *Nature Mater.* **8**, 494 (2009).

[5] Y.Y. Deng, and H. Sirringhaus, *Phys. Rev. B* **72**, 045207 (2005).

[6] J. Cabanillas-Gonzalez, T. Virgili, A. Gambetta, G. Lanzani, T. D. Anthopoulos, and D.M. de Leeuw, *Phys. Rev. Lett.* **96**, 106601 (2006).

[7] H. Tsuji, and Y. Furukawa, *Mol. Cryst. Liq. Cryst.* **455**, 353 (2006).

[8] C. Goldmann, S. Haas, C. Krellner, K.P. Pernstich, D.J. Gundlach, and B. Batlogg, *J. Appl. Phys.* **96**, 2080 (2004).

[9] R. Matsubara, N. Ohashi, M. Sakai, K. Kudo, and M. Nakamura, *Appl. Phys. Lett.* **92**, 242108 (2008).

[10] T.D. Anthopoulos, S. Setayesh, E. Smits, M. Cölle, E. Cantatore, B. de Boer, P.W.M. Blom, and D.M. de Leeuw, *Adv. Mater.* **18**, 1900 (2006).

[11] E.C.P. Smits, S.G.J. Mathijssen, M. Cölle, A.J.G. Mank, P.A. Bobbert, P.W.M. Blom, B. de Boer, and D.M. de Leeuw, *Phys. Rev. B* **76**, 125202 (2007).

[12] O.D. Jurchescu, M. Popinciuc, B.J. van Weeks, and T.T.M. Palstra, *Adv. Mater.* **19**, 688 (2004).

[13] G. Wang, J. Swensen, D. Moses, and A.J. Heeger, *J. Appl. Phys.* **93**, 6137 (2003).

[14] I. McCulloch, M. Heeney, C. Bailey, K. Genevicius, I. MacDonald, M. Shkunov, D. Sparrowe, S. Tierney, R. Wagner, W. Zhang, M.L. Chabinyc, R.J. Kline, M.D. McGehee, and M.F. Toney, *Nature Mater.* **5**, 328 (2006).

[15] W. Geens, D. Tsamouras, J. Poortmans, and G. Hadziioannou, *Synth. Met.* **122**, 191 (2001).

[16] H. Yan, Z. Chen, Y. Zheng, C. Newman, J.R. Quinn, F. Dötz, M. Kastler, and A. Facchetti, *Nature* **457**, 679 (2009).

[17] A. Tsumura, H. Koezuka, and T. Ando, *Synth. Met.* **25**, 11 (1988).

[18] G. Horowitz, M.E. Hajlaoui, and R. Hajlaoui, *J. Appl. Phys.* **87**, 4456 (2000).

- [19] M.-H. Yoon, H. Yan, A. Facchetti, and T.J. Marks, *J. Am. Chem. Soc.* **127**, 10388 (2005).
- [20] M.-H. Yoon, C. Kim, A. Facchetti, and T.J. Marks, *J. Am. Chem. Soc.* **128**, 12851 (2006).
- [21] E. Menard, V. Podzorov, S.-H. Hur, A. Gaur, M.E. Gershenson, and J.A. Rogers, *Adv. Mater.* **16**, 2097 (2004).
- [22] H. Sirringhaus, *Adv. Mater.* **17**, 1 (2005).
- [23] Z. Bao, A. Dodabalapur, and A.J. Lovinger, *Appl. Phys. Lett.* **69**, 4108 (1996).
- [24] H. Sirringhaus, N. Tessler, and R.H. Friend, *Science* **280**, 1741 (1998).
- [25] G.H. Gelinck, T.C.T. Geuns, and D.M. de Leeuw, *Appl. Phys. Lett.* **77**, 1487 (2000).
- [26] A. Afzali, C.D. Dimitrakopoulos, and T.L. Breen, *J. Am. Chem. Soc.* **124**, 8812 (2002).
- [27] <http://www.comsol.com/>
- [28] M.C.J.M Vissenberg, and M. Matters, *Phys. Rev. B* **57**, 12964 (1998).
- [29] L.-L. Chua, J. Zaumseil, J.-F. Chang, E.C.-W. Ou, P.K.-H. Ho, H. Sirringhaus, and R.H. Friend, *Nature* **434**, 194 (2005).
- [30] T.D. Anthopoulos, G.C. Anyfantis, G.C. Papavassiliou, and D.M. de Leeuw, *Appl. Phys. Lett.* **90**, 122105 (2007).
- [31] C. Groves, and N.C. Greenham, *Phys. Rev. B* **78**, 155205 (2008).
- [32] J. Zaumseil, R.H. Friend, and H. Sirringhaus, *Nature Mater.* **5**, 69 (2006).
- [33] E.C.P. Smits, S. Setayesh, T.D. Anthopoulos, M. Buechel, W. Nijssen, R. Coehoorn, P.W.M. Blom, B. de Boer, and D.M. de Leeuw, *Adv. Mater.* **19**, 734 (2007).
- [34] L. Bürgi, M. Turbiez, R. Pfeiffer, F. Bienewald, H.-J. Kirner, C. Winnewisser, *Adv. Mater.* **20**, 2217 (2007).
- [35] J.S. Swensen, J. Yeun, D. Gargas, S.K. Buratto, and A.J. Heeger, *J. Appl. Phys.* **102**, 013103 (2007).
- [36] C. Argento, and R.H. Friend, *J. Appl. Phys.* **80**, 6081 (1996).
- [37] S. Hudlet, M. Saint Jean, B. Roulet, J. Berger, and C. Guthmann, *J. Appl. Phys.* **77**, 3308 (1994).

- [38] S.C. Jain, W. Geens, A. Mehra, V. Kumar, T. Aernouts, J. Poortmans, and R. Mertens, and M. Willander, *J. Appl. Phys.* **89**, 3804 (2001).
- [39] L. Bürgi, T.J. Richards, R.H. Friend, and H. Sirringhaus, *J. Appl. Phys.* **94**, 6129 (2003).
- [40] K.P. Puntambekar, P.V. Pesavento, and C.D. Frisbie, *Appl. Phys. Lett.* **83**, 5539 (2003).
- [41] Y. Luo, F. Gustavo, J.-Y. Henry, F. Mathevet, F. Lefloch, M. Sanquer, P. Rannou, and B. Grévin, *Adv. Mater.* **19**, 2267 (2007).
- [42] V. Palermo, M. Palma, and P. Samori, *Adv. Mater.* **18**, 145 (2006).
- [43] W.R. Silveira, and J.A. Marhon, *Phys. Rev. Lett.* **93**, 116104 (2004).



## Chapter 2

# Real versus measured surface potentials in scanning Kelvin probe microscopy

### 2.1 Introduction

In recent years the potential mapping on organic semiconductor devices has been steadily gaining momentum. Scanning Kelvin probe microscopy (SKPM) and electric force microscopy (EFM) both offer unique opportunities to measure local surface potentials with ~100 nm resolution on operational devices. Since the measured surface potential seems to reflect the actual potential in the active layer, and this information is otherwise unattainable, these techniques are becoming more and more popular for characterizing physical aspects of organic thin films devices<sup>1</sup> such as charge transport in polymer transistors<sup>2</sup> and charge generation in organic solar cells.<sup>3</sup>

As a consequence, the resolution of the SKPM measurements is an important issue. Several experimental and theoretical studies have identified the tip-to-sample distance<sup>4-14</sup> and the tip radius<sup>15-16</sup> as the limiting parameters. Actually, the lateral resolution is affected by the capacitive coupling between the entire tip, including apex, cone and lever, and the device. Due to this complex geometry, the problem is three dimensional and so far, no predictive model has been reported in literature. The two dimensional simulations that have been reported<sup>17-20</sup> do not account for the asymmetric influence of the lever,<sup>6,21</sup> which causes the problem to become truly three dimensional. We used a standard organic transistor layout without active layer, see Figure 1, as a relevant test system to quantify the electrostatic tip-sample interaction. It appears that the measured potential profile between ‘source’ and ‘drain’ electrodes strongly depends on whether the tip is parallel or orthogonal to the channel. Moreover, only a fraction (from

50 % to 90 %) of the applied voltage is observed in measured potential traces. It would seem, therefore, that further investigations are needed to quantify and understand the non-negligible influence of the entire tip-sample interaction. This paper describes a numerical tool, enabling the quantitative prediction of the surface potential as measured by SKPM without the use of any fitting parameters.

The rest of this chapter is organized as follows. In the first part we will describe the principle of the surface potential measurements which allows us to show the experimental resolution problem in detail. In the second part we will describe the three dimensional SKPM simulations and we will confront them with the measurements on the test devices.

## 2.2 Experimental SKPM results

SKPM combines the classical Kelvin probe technique with atomic force microscopy (AFM). Ideally, SKPM probes the electrochemical potential of the sample under the tip apex, which in case of a metallic tip and sample with work function  $\chi_{tip}$  and  $\chi_{sample}$ , respectively, is equivalent to a measurement of the contact potential difference  $V_{cpd} = (\chi_{tip} - \chi_{sample})/e$ , where  $e$  is the electron charge.

The SKPM measurements are performed on a commercial AFM system (Dimension 3100 connected to a Nanoscope IIIa controller equipped with a Quadrex module, Veeco Instruments) using metallized cantilevers (OMCL-AC240TM), Olympus, resonant frequency  $\sim 70$  kHz, spring constant  $\sim 2$  N/m, lever thickness  $2.8 \mu\text{m}$ , lever length  $240 \mu\text{m}$ , lever width  $30 \mu\text{m}$ . The tip height is around  $14 \mu\text{m}$  and the tip radius  $\sim 30$  nm. Potential maps are taken in interleave mode in which the potential is measured at each scan line in a second pass at a predefined lift height  $\Delta z$ . An AC bias  $V_{ac}$  at frequency  $\omega$  close to the AFM tip resonance frequency is applied between the tip and the sample, in combination with a DC voltage  $V_{dc}$ . The force along the  $z$  axis is given by  $F_z = -\frac{V^2}{2} \frac{dC}{dz}$  with  $V = V_{dc} + V_{ac} \sin(\omega t) - V_{cpd}$  where  $C$  is the entire capacity between tip and surface. By introducing the latter expression into the force expression, the force at the resonant

## 2. Real versus measured surface potentials in scanning Kelvin probe microscopy

frequency becomes  $F_\omega = \frac{dC}{dz} V_{ac} (V_{cpd} - V_{dc})$ . The force  $F_\omega$  is nullified by setting  $V_{cpd} = V_{dc}$ , and does not depend on the resonant frequency  $\omega$  which becomes a non-influencing parameter. Strictly spoken, this is only valid for a metal/metal configuration of two infinite plates, for the metal/semiconductor case  $V_{cpd}$  is different and is extensively described by Hudlet *et al.*<sup>22</sup>

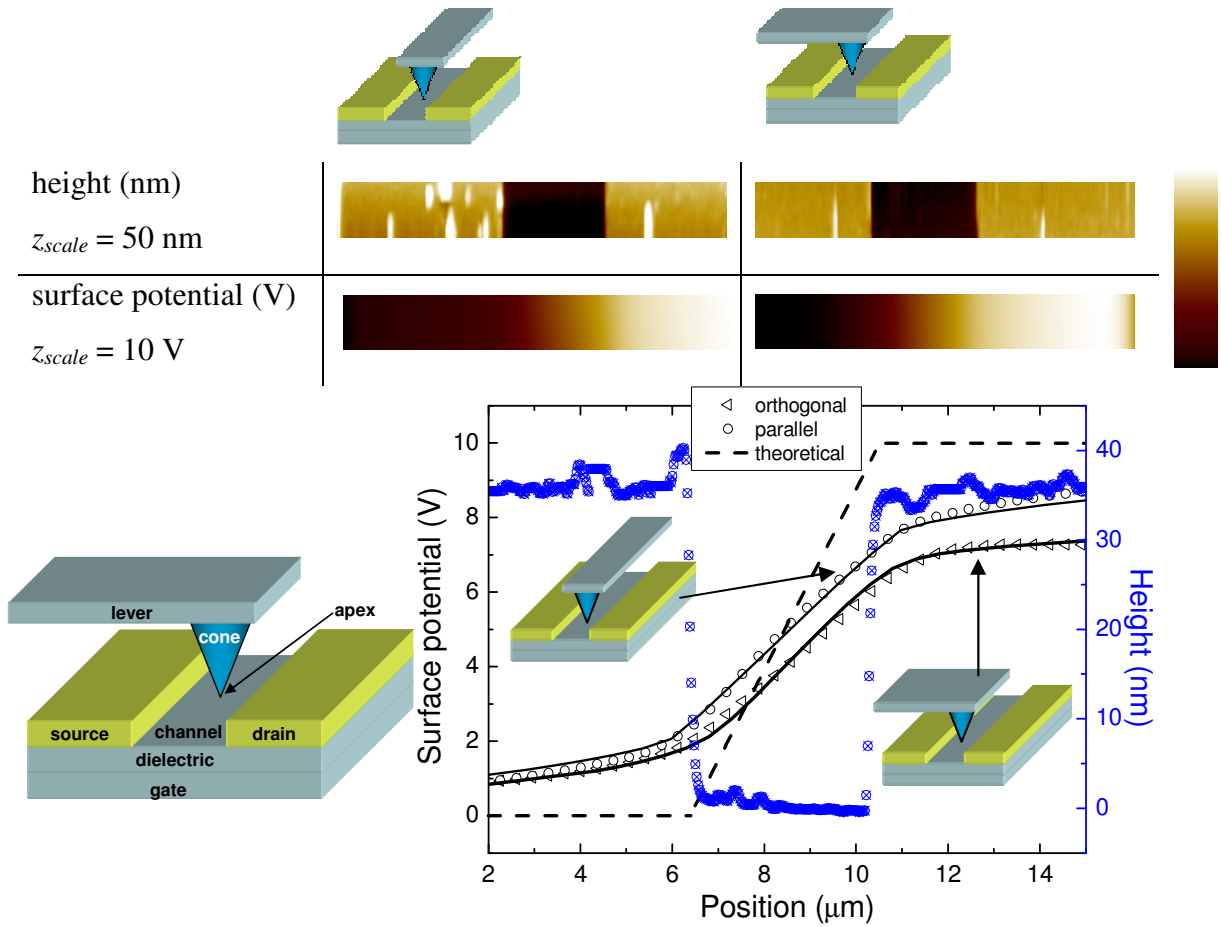


Fig. 1. Top: Table showing topography and surface potential measured on a test device in two different orientations: tip parallel to the channel and tip perpendicular to the channel. Bottom left: schematic view of the probe area. Bottom right: Potential profile as measured by SKPM. The symbols (lines) denote experimental data (numerical simulations), done at 0 nm lift height. The applied potential profile is shown as dashed line. Note the difference in potential profile depending on the cantilever orientation. The insets show the tip and sample orientation. The blue dotted line shows a topography line section.

We performed SKPM measurements on bottom-contact, bottom gate transistor substrates while applying a source-drain voltage of 10 V. Because of the absence of an active layer, the naively expected potential profile is a plateau at 0 V over the source and a plateau at 10 V over the drain, linked by a straight line in the channel, as indicated by the dotted line in Fig. 1. The SKPM result obtained for  $\Delta z = 0$  nm is shown in Figure 1. Wu *et al*<sup>23</sup> remarked that due to the oscillation amplitude,  $\Delta z = 0$  nm corresponds at a tip-to-sample distance around 30 nm. Clearly, several deviations from the expected behavior are visible. The potential profile is not constant over the electrodes, the highest curvature does not occur at the channel edge, and the full bias of 10 V is not visible. In literature, several reports described the same behavior.<sup>22,25-28</sup> Moreover, depending on the tip-to-channel orientation (orthogonal or parallel) the surface potential is dramatically different. A second observation is the strong influence of the tip-to-sample distance, which was discussed before<sup>4-14</sup> as being a limiting parameter. Figure 2 shows a set of data for different  $\Delta z$  (0, 100, and 1000 nm). These observations have strong impact on the applicability of SKPM for the investigation of (organic) transistors and other devices, since the models to which the measured potential profiles are compared do not take these limitations into account. It should be emphasized that even for the smallest lift height, the error is non-negligible, as witnessed by Figs. 1 and 2. In order to overcome this problem, the raw data are often rescaled to the expected values,<sup>29-30</sup> although this is not common practice.<sup>31-32</sup> The rescaling procedure does not solve the problem for both mathematical and practical reasons and deletes part of the information. In our case, such rescaling does not remove the rounding in the experimental curves, nor does it repair the geometry-induced asymmetry. In order to quantify these problems and to come to a workable link between device model and SKPM response, we developed a fully 3D SKPM modeling. The simulations that will be discussed in the next sections excellently fit the experimental data, as shown by the continuous lines in Figs. 1 and 2.

## 2. Real versus measured surface potentials in scanning Kelvin probe microscopy

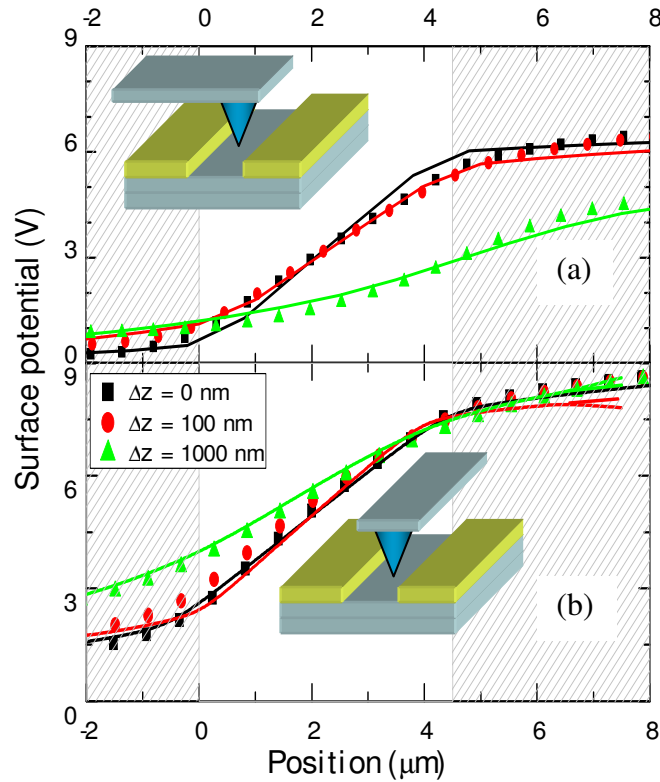


Fig. 2. Experimental (symbols) and modeled (lines) surface potentials for three different tip-surface distances  $\Delta z$  over a  $4.5 \mu\text{m}$  long channel.  $\Delta z = 0 \text{ nm}$  (squares),  $100 \text{ nm}$  (circles) and  $1000 \text{ nm}$  (triangles). (a) With the tip orthogonal to the channel. (b) With the tip parallel to the channel. In both cases, the measured voltage difference is decreasing with the lift scan height. The insets show the tip and sample orientation.

### 2.3 Simulation of SKPM

In order to simulate the SKPM technique, we used a commercial finite-element package which allows one to draw and subsequently simulate realistic tip and device shapes, see Figure 3 (a) and (b). An additional organic layer, which would be present in an actual organic field effect transistor, can be easily added in a future work. A meshing procedure fills the entire space with tetrahedrons while conserving continuity at their

interfaces and builds up all object as compositions of tetrahedrons, see Fig. 3 (b). The discrete filling of tetrahedrons causes a limitation in resolution if the meshing density is low. The software tool used allows one to control the meshing in some detail, which is crucial for reducing the numerical scatter to an acceptable level. The issue of numerical noise is further addressed below in the discussion of Fig. 5. It is important to point out that the model described above does not have any fitting parameters, i.e. all parameters are known prior to the simulation.

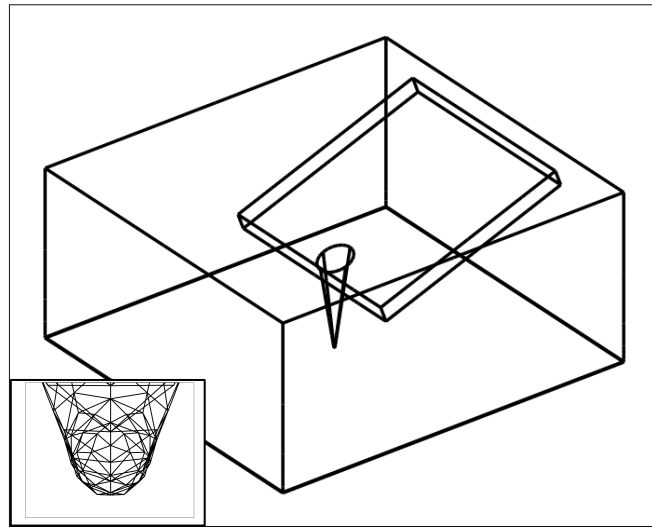


Fig. 3. Three-dimensional drawing of the tip - consisting of lever, cone and apex - into a vacuum box which determines the calculation space. The box size is  $50 \mu\text{m} \times 65 \mu\text{m}$  (surface)  $\times 25 \mu\text{m}$  (height). The drawn tip is not an exact replica of the tip used in the experiments but all characteristic features (cone angle and height, apex radius, width and tilt of the lever) are reproduced. The inset is a zoom on the tip meshing, showing that the apex is defined as a combination of tetrahedrons which can lead to a limitation in resolution, see text.

Subsequently the SKPM response  $V_{SKPM}$  is calculated as follows: for a given tip-to-sample distance and lateral tip position, the vertical force between the tip and the surface is calculated as a function of  $V_{dc}$ . The force  $F_z$  versus  $V_{dc}$  is a parabola as expected

## 2. Real versus measured surface potentials in scanning Kelvin probe microscopy

from simple electrostatics, of which the potential  $V_{SKPM}$  that is measured by SKPM is the maximum, see Fig. 4.

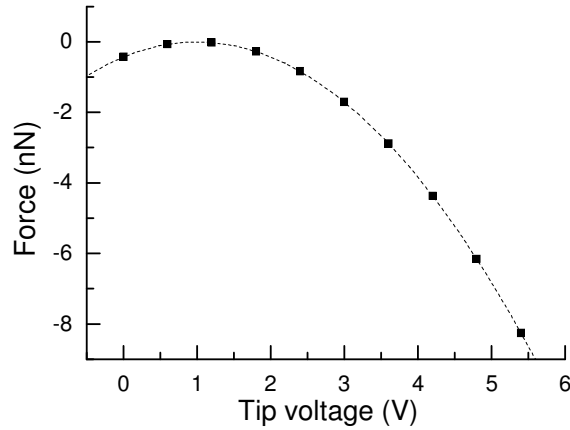


Fig. 4. Vertical force between the probe (including cone, apex and cantilever) and the entire device versus bias applied to the probe. Since the SKPM technique nullifies this force, the voltage at the extreme of the parabola equals the SKPM output  $V_{SKPM}(x)$ . The calculation is done in the channel close to the source.

Then, for each new geometry the force between tip and surface as a function of tip-to-sample distance is calculated. Figure 5 shows the force for both tip-to-channel orientations. The curves are not smooth since the meshing procedure creates a slightly different distribution of tetrahedrons after every change in geometry. However, once proper settings are found, a relatively smooth curve with few deviating points is obtained. In the subsequent calculation of lateral SKPM profiles the particular tip-to-sample distances at which scatter occurs are avoided. To check if the simulated downward force is reasonable, a comparison with analytical expressions given in literature for a system consisting of an apex plus cone<sup>16</sup> is made. We find that both the order of magnitude and the behavior at small separation are similar, whereas the height dependence at larger separation is weaker in the present case because of the (almost constant) coupling of the relatively large lever to the sample, which is not present in the analytical expressions.

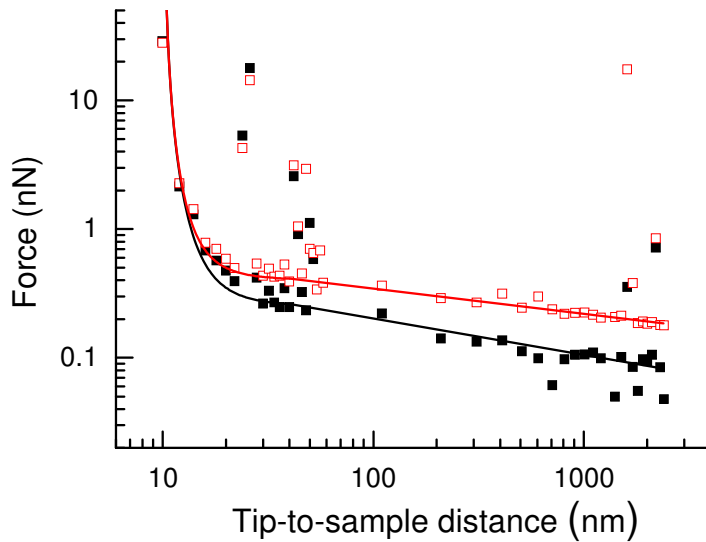


Fig. 5. Vertical (downward) force between the tip and the surface versus their separating distance. The calculations were done in the middle of channel. Empty squares (full squares) correspond to the tip orthogonal (parallel) to the channel. The thin lines are a guide to the eye.

Figure 2 (a) and (b) show the experimental and simulated surface potentials for three different lift scan heights, 0 nm, 100 nm and 1000 nm, in the orthogonal and parallel configuration. Clearly, all characteristic features in the experimental traces like the non-constant signal above the electrodes and the loss of resolution with increasing height are well reproduced by the calculations. Also the dependence on tip-to-channel orientation is correctly described by the model. As anticipated, the (lack of) symmetry of the experimental situation with respect to the middle of the channel in the (anti) parallel situation results in (a)symmetric SKPM traces. Obviously, the real electrostatic potential profile is symmetric in both cases. We attribute the small differences between the experimental and modeling curves to slight differences between the modeled and true tip. In particular, the inclination of the cantilever is known to be around  $35^\circ$  with errors in fabrication. The cone height ranges between 9 and 19  $\mu\text{m}$  due to fabrication margins.

Having established the model, it is worthwhile to briefly point out some ‘scaling’ properties of SKPM measurements. Figure 6 shows three different biasing configurations that are possible with the tip orthogonal to the channel. Electrostatically, these situations

## 2. Real versus measured surface potentials in scanning Kelvin probe microscopy

are equivalent. Therefore, provided that the shape of the potential distribution  $V(x)$  is independent of the magnitude of the bias, as is the case in our test devices, one may anticipate that all SKPM curves can be rescaled to one ‘master curve’ that only depends on the geometry. Obviously, the same holds for the tip parallel to the channel. For the simulations, this result implies that per geometry only one calculation is needed and that  $V_{SKPM}(x)$  of configurations with different biases on the ‘source’ and ‘drain’ electrodes can be obtained by simple rescaling. Note, however, that in many ‘real’ devices like FETs outside the linear regime, the shape of  $V(x)$  is not independent of source-drain bias.

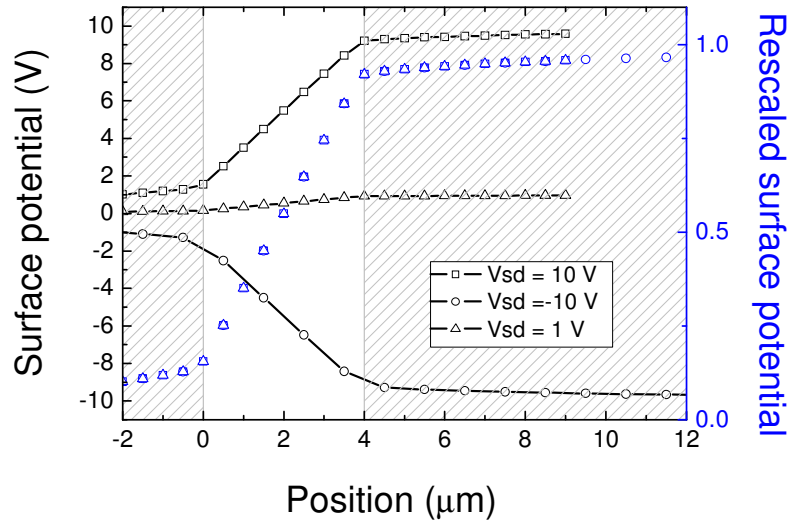


Fig. 6. (a) Potential profiles for three different source-drain potentials  $V_{sd} = 10$  V, 1 V and -10 V (top to bottom). (b) as (a), after rescaling the curves in panel (a) by dividing them by the applied source-drain bias.

In order to qualitatively estimate the contribution of different tip parts, Figure 7 shows the experimental potential profile in the geometry with the lever orthogonal to the channel and three different modeling curves. The solid black line is calculated for the full 3D probe consisting of apex, cone and lever. Calculations for a probe consisting of cone + apex (red dashed line) and only a single apex (blue dotted line) are also shown. A few comments can be given. As soon as the lever disappears to leave only the apex + cone, the full potential difference at the electrodes becomes 20% higher. Moreover the non-

symmetric potential profile that is calculated with the full tip becomes symmetric upon removal of the lever, reflecting the increased symmetry of the ‘reduced’ probes. When also the cone is removed from the calculation, the potential profile becomes virtually identical to the true surface potential. The minor deviations in the present calculation are due to the limited number of calculated lateral points. From a comparison of these three situations, it follows that the optimal geometry for a practical probe is one where (a) the cone is long –to reduce the coupling between the sample and the lever– and slender –to minimize the coupling between the sample and the cone itself and (b) the lever is narrow –again to avoid undesired coupling to the sample. Moreover, to avoid asymmetry, the lever is preferably kept parallel to the channel.

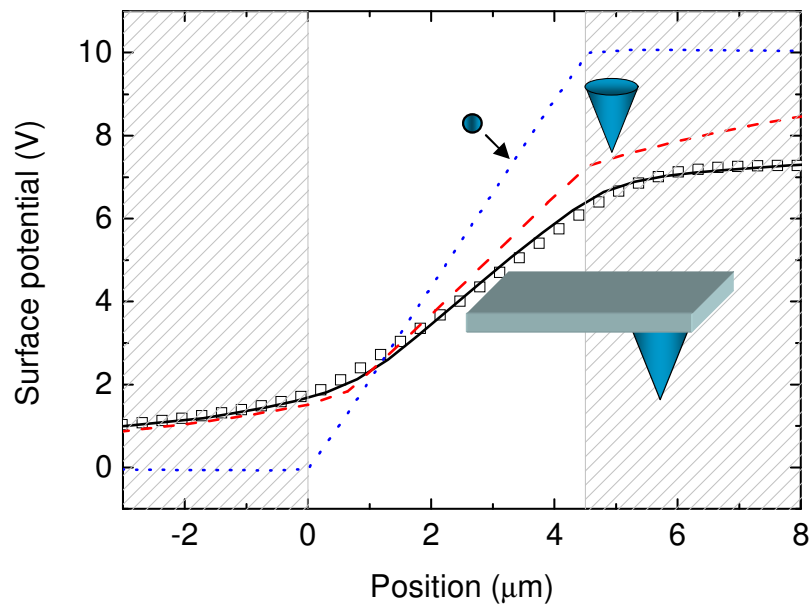


Fig. 7. Experimental potential profile in the situation with the lever orthogonal to the channel (squares) and modeling for a full 3D tip (black line) containing the apex, cone and lever. The red dashed line is the simulation for a probe consisting only of cone + apex, the blue dotted line for a probe consisting of only an apex.

## 2. Real versus measured surface potentials in scanning Kelvin probe microscopy

### 2.4 Conclusion

Summarizing, we have shown that the potential profiles that are measured by scanning Kelvin probe microscopy do not purely reflect the electrostatic potential under the tip apex, but are strongly affected by the electrostatic coupling between the *entire* probe and the *entire* device, even at small tip-sample separation. We have developed a 3D numerical model that enables one to quantitatively predict the SKPM output from a known potential distribution and geometry. The model is successfully compared to SKPM measurements performed on relevant test devices.

### 2.5 Materials and methods

The used samples were typical bottom contact and bottom gate transistor substrates defined using UV lithography and lift-off, i.e. a device structure that is commonly used in organic semiconductor research and technology. The structures were fabricated on  $n^+$  - Si wafers with a thick (1  $\mu\text{m}$ ) thermally grown  $\text{SiO}_2$  oxide layer ( $\epsilon_r = 3.9$ ). The source and drain electrodes consisted of 25 nm Au on top of a 5 nm Ti adhesion layer, and were shaped either as interdigitated fingers or as concentric rings, both with various  $W/L$  ratios. For the present work, no substantial differences between interdigitated and ring geometries were found.

Numerical simulations were performed using COMSOL 3.2b in combination with MatLab 7.1 running on a desktop pc with 2 GB of internal memory. In the simulations the entire system was split into three blocks, being the tip containing a semi-spherical apex, a cone and a parallelepiped lever, the surrounding vacuum block and a block representing the substrate surface and contacts (Fig. 3). Once the geometry was drawn, the subdomain settings had to be defined, the subdomains being blocks. The tip was defined as platinum, the space around the tip was air. An organic layer, if present, was a dielectric layer defined with a dielectric constant  $\epsilon_r$ . In order to simplify the geometry and avoid the need of re-meshing for each lateral tip position, the electrodes were assumed to

have zero height, so their potential can be analytically defined via boundary condition settings. The order of error of this assumption had not been strictly checked, since the calculations would require a huge amount of memory which was out of our computational possibility. However, we expected that the error was confined to a narrow region with a width that was comparable to the electrode height, i.e. a few tens of nm. In the modeling we assumed zero contact resistance which is the case in most devices in this thesis. The implementation of contact resistance is possible by accordingly including the potential steps at the electrodes.

The boundary settings were a DC potential  $V_{dc}$  on the tip, continuity for all the interior boundaries and electric insulation for the exterior boundaries. The surface potential  $V_{cpd}(x)$  from which the SKPM response  $V_{SKPM}$  was to be determined was defined as a boundary condition for the potential of the bottom surface, using an equation function of coordinates (Oxyz). By defining the surface potential on top of the gate oxide, the underlying bulk layers, i.e. the dielectric  $\text{SiO}_2$  and gate  $n^+$ -Si, needed not to be defined anymore since the surface potential boundary condition contained their contribution and (by definition) screens everything underneath. Instead of moving the tip, which required re-meshing and caused significant numerical noise, the channel was analytically moved along the  $x$  axis. Moreover, COMSOL offered the possibility to increase locally the meshing quality when the parameters by defaults gave a non-optimized resolution between the apex and the surface. The ‘Maximum element size’ parameter specified the maximum allowed element size, which by default was 1/10th of the maximum distance in the geometry. The apex had a Maximum element size equal to 0.09 in COMSOL unit, corresponding to 18 nm. The ‘Element growth rate’ determined the maximum rate at which the element size can grow from a region with small elements to a region with larger elements. The value must be greater or equal to one. In our calculation we took the Element Growth Rate at 1.7.

## 2.6 References and notes

- [1] S. Palermo, M. Palma, and P. Samorì, *Adv. Mater.* **18**, 145 (2006).

## 2. Real versus measured surface potentials in scanning Kelvin probe microscopy

- [2] L. Bürgi, T. Richards, M. Chiesa, R.H. Friend, and H. Sirringhaus, *Synth. Met.* **146**, 297 (2004).
- [3] D.C. Coffey, and D.S. Ginger, *Nature Mater.* **5**, 735 (2006).
- [4] Z. Weng, T. Kaminsky, G.E. Bridges, and D.J. Thomson, *J. Vac. Sci. Technol. A* **22**, 948 (2004).
- [5] G.M. Sacha, and J.J. Sáenz, *Appl. Phys. Lett.* **85**, 2610 (2004).
- [6] G. Koley, G. Spencer, and H.R. Bhangale, *Appl. Phys. Lett.* **79**, 545 (2001).
- [7] A. Gil, J. Colchero Gómez-Herrero, and A.M. Baró, *Nanotechnology* **14**, 332 (2003).
- [8] T. Takahashi, and S. Ono, *Ultramicroscopy* **100**, 287 (2004).
- [9] S. Belaidi, P. Girard, and G. Leveque, *J. Appl. Phys.* **81**, 1023 (1997).
- [10] O. Vatel, and M. Tanimoto, *J. Appl. Phys.* **77**, 2358 (1995).
- [11] R. Shikler, and Y. Rosenwaks, *Appl. Surf. Sci.* **157**, 11041 (2000).
- [12] S. Hudlet, M. Saint Jean, C. Guthmann, and J. Berger, *Eur. Phys. J. B* **2**, 5 (1998).
- [13] A.S. Foster, L.N. Kantorovich, and A.L. Shluger, *Appl. Phys. A* **72**, 59 (2001).
- [14] E. Bonaccorso, F. Schönfeld, and H.-J. Butt, *Phys. Rev. B* **74**, 085413 (2006).
- [15] G.M. Sacha, A. Verdaguer, J. Martinez, J.J. Sáenz, D.F. Ogletree, and M. Salmeron, *Appl. Phys. Lett.* **86**, 123101 (2005).
- [16] C. Argento, and R.H. French, *J. Appl. Phys.* **80**, 6081 (1996).
- [17] E. Tevaarwerk, D.G. Keppel, P. Rugheimer, M.G. Lagally, and M.A. Eriksson, *Rev. Sci. Instrum.* **76**, 053707 (2005).
- [18] H.O. Jacobs, P. Leuchtman, O.J. Homan, and A. Stemmer, *J. Appl. Phys.* **84**, 1168 (1998).
- [19] T.S. Gross, C.M. Prindle, K. Chamberlin, N. bin Kamsah, and Y. Wu, *Ultramicroscopy* **87**, 147 (2001).
- [20] S. Belaidi, F. Lebon, P. Girard, G. Leveque, and S. Pagano, *Appl. Phys. A* **66**, 239 (1998).
- [21] T. Hochwitz, A.K. Henning, C. Levey, C. Daghljan, and J. Slinkman, *J. Vac. Sci. Technol. B* **14**, 457 (1996).
- [22] S. Hudlet, M. Saint Jean, B. Roulet, J. Berger, and C. Guthmann, *J. Appl. Phys.* **77**, 3308 (1995).
- [23] Y. Wu, and M.A. Shannon, *Rev. Sci. Instrum.* **77**, 043711 (2006).

- [24] J.A. Nichols, D.J. Gundlach, and T.N. Jackson, *Appl. Phys. Lett.* **83**, 2366 (2003).
- [25] K. Müller, A. Goryachko, Y. Burkov, C. Schwiertz, M. Ratzke, J. Köble, J. Reif, and D. Schmeißer, *Synth. Met.* **146**, 377 (2004).
- [26] C.H. Lei, A. Das, M. Elliot, and J.E. Macdonald, *Nanotechnology* **15**, 627 (2004).
- [27] U. Zerweck, C. Loppacher, T. Otto, S. Grafström, and L.M. Eng, *Phys. Rev B* **71**, 125424 (2005).
- [28] Y. Luo, F. Gustavo, J.-Y. Henry, F. Mathevet, F. Lefloch, M. Sanquer, P. Rannou, and B. Grévin, *Adv. Mater.* **19**, 2267 (2007).
- [29] K.P. Puntambekar, P.V. Pesavento, and C.D. Frisbie, *Appl. Phys. Lett.* **83**, 5539 (2003).
- [30] E.C.P. Smits, S.G.J. Mathijssen, M. Cölle, A.J.G. Mank, P.A. Bobbert, P.W.M. Blom, B. de Boer, and D.M. de Leeuw, *Phys. Rev B* **76**, 125202 (2007).
- [31] W.R. Silveira, and J.A. Marohn, *Phys. Rev. Lett.* **93**, 116104 (2004).
- [32] L. Bürgi, H. Sirringhaus, and R.H. Friend, *Appl. Phys. Lett.* **80**, 2913 (2002).

## Chapter 3

# On the width of the recombination zone in organic light emitting field effect transistors

### 3.1 Introduction

The recent realization of bipolar currents in organic field effect transistors has enabled the fabrication of organic light emitting field effect transistors (LEFET).<sup>1</sup> The high current densities in these devices<sup>2</sup> as compared to those in diode-type devices may help to reach population inversion which is a prerequisite for an electrically driven organic laser.<sup>3</sup> Apart from the possible use in an organic lasing device, LEFET may offer significant advantages over conventional organic light emitting diodes (OLED). Not only the high current density, but also the possibility to shift the recombination zone away from the metallic contacts and the fact that all free carriers contribute to exciton formation can lead to increased brightness and efficiency.<sup>1,4</sup> However, the high carrier and exciton densities in LEFET may also enhance exciton quenching, reducing the internal quantum efficiency.<sup>2,4,5</sup>

Since exciton-exciton and exciton-carrier quenching rates are strong functions of the exciton and carrier density, both the maximum attainable exciton density and the in- and external quantum efficiency of LEFET strongly depend on the width of the recombination zone. So far, the actual value of the recombination zone width  $W$  has received surprisingly little attention. In theoretical works,  $W$  is commonly taken to be zero, i.e. an infinite bimolecular recombination rate  $R$  is assumed.<sup>6,7,8</sup> Experimentally, both confocal optical<sup>9</sup> and electrostatic<sup>10</sup> methods have been employed to resolve the

recombination profile, yielding values for  $W$  in the micrometer range. However, both techniques suffer from a non-negligible finite spatial resolution.

Here, we present an analytical model for the width and shape of the recombination profile in ambipolar transistors, including LEFET.<sup>11</sup> The results compare favorably to numerical calculations and indicate that  $W \approx 100$  nm for typical organic LEFET when  $R$  is taken equal to the Langevin rate. This observation is supported by a detailed analysis of surface potential profiles as measured by scanning Kelvin probe microscopy (SKPM).

### 3.2 Analytical model of recombination width

With the analytical model, one allows to calculate the recombination of electrons and holes in the recombination zone of a LEFET. For this, we divide the device in three regions as illustrated in Fig. 1. In the regions between the source and drain contacts and the recombination zone we apply the gradual channel approximation<sup>12</sup>, i.e. the hole and electron densities are given by  $p = C(V(x) - V_g)$  and  $n = C(V_g - V(x))$ , with  $V(x)$  and  $V_g$  the (local) channel and gate potential, respectively.  $C = \epsilon_0 \epsilon_r / d$  is the gate capacitance with  $\epsilon_r$  and  $d$  the relative dielectric constant and thickness of the gate insulator. Inside the recombination zone we assume that the carrier densities are determined by the recombination process only. Assuming further a constant electrostatic field  $F$ , the hole and electron drift current densities are  $j_h = qp\mu_h F$  and  $j_e = qp\mu_e F$  with  $q$  the elementary charge,  $p$ ,  $n$  the hole and electron density and  $\mu_h$ ,  $\mu_e$  the hole and electron mobility, respectively. Using a Langevin-type recombination rate  $R = \gamma np$  one finds for the hole and electron density

$$\frac{dp}{dt} = \frac{dp}{dx} \frac{dx}{dt} = \frac{dp}{dx} v_h = -\gamma np = \frac{dn}{dx} v_e = \frac{dn}{dt} \quad (1)$$

where  $v_h = \mu_h F$  and  $v_e = -\mu_e F$  are the hole and electron drift velocities. In (1) diffusion effects are tacitly ignored, which will be justified below.

### 3. On the width of the recombination zone in organic light emitting field effect transistors

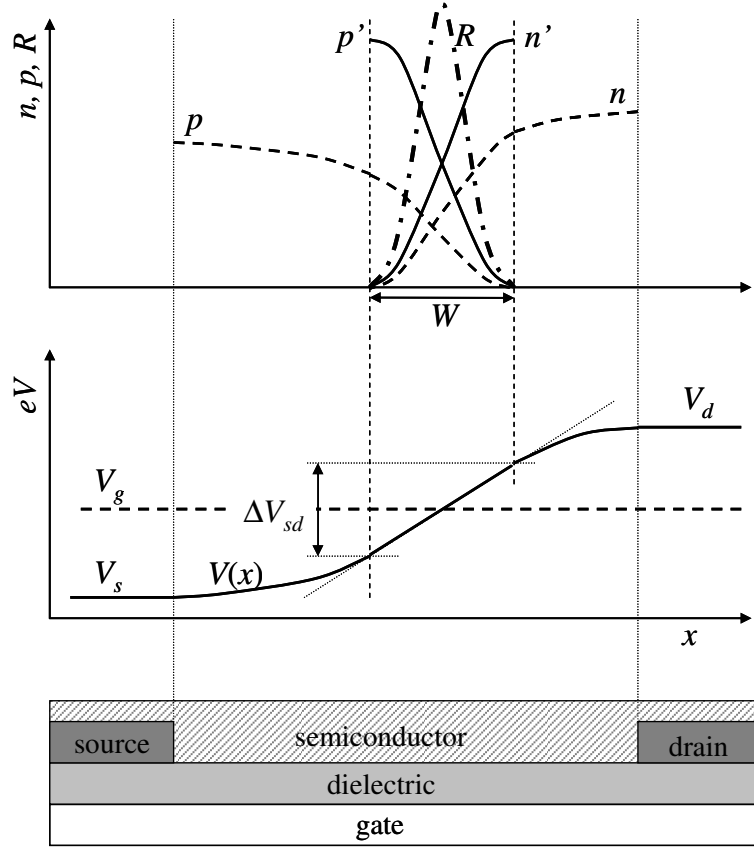


Fig.1. Schematic layout of the LEFET as assumed in the analytical model. The top panel shows carrier densities and recombination vs. position in the LEFET channel. The middle panel shows the potential profile and the bottom panel the device layout. Parameters are explained in the text. Note that  $n', p'$  are symmetric, whereas  $n, p$  are not.

Defining effective densities  $p' \equiv \mu_h p$  and  $n' \equiv \mu_e n$  current conservation demands that the limiting values of  $p', n'$  on either side of the recombination zone are equal, i.e.  $p'_0 = n'_0 = j/qF$ . For a given source-drain voltage  $V_{sd}$ , this condition fixes the gate voltage to  $-V_{sg} = V_s - V_g = V_{sd} / (1 + \mu_h / \mu_e)$ , to be used later. Moreover, one has  $p'(x) + n'(x) = p'_0 = n'_0$  everywhere in the recombination zone. With these definitions one easily arrives at the following differential equations

$$\frac{dp'}{dx} = -\alpha p'(p'_0 - p') \quad \text{and} \quad \frac{dn'}{dx} = \alpha n'(n'_0 - n') \quad (2)$$

with  $\alpha \equiv \gamma/\mu_h\mu_e F$ . Taking the source (drain) on the left (right) and for the source ( $V_s$ ), gate ( $V_g$ ) and drain ( $V_d$ ) voltages  $V_s > V_g > V_d$  as in Fig. 1, the solution of (2) is

$$p' = \frac{p'_0}{\exp[p'_0\alpha(x-x_0)]+1} \quad \text{and} \quad n' = \frac{n'_0 \exp[n'_0\alpha(x-x_0)]}{\exp[n'_0\alpha(x-x_0)]+1} \quad (3)$$

with  $x_0$  the position of the center of the recombination zone where  $p'(x_0) = n'(x_0) = \frac{1}{2}n'_0$ .

The recombination profile follows from  $R = \gamma np$ , i.e.

$$R = \frac{\gamma n_0'^2}{\mu_h\mu_e} \frac{\exp[n'_0\alpha(x+x_0)]}{(\exp[n'_0\alpha(x+x_0)]+1)^2}. \quad (4)$$

Taking  $W$  as the width at which  $R$  reaches  $1/e$  of its maximum value, one obtains  $W = 4.34/n'_0\alpha$ .

In order to apply the above to actual devices, estimates for the boundary conditions  $p'_0$ ,  $n'_0$  and the field  $F$  need to be made. Defining  $\Delta V_{sd}$  as the voltage drop over the recombination zone one finds from their definitions that  $\alpha \sim 1/F = W/\Delta V_{sd}$  and  $n'_0 \sim \Delta V_{sd}$ . Hence  $W = 4.34/n'_0\alpha$  becomes the square root of a constant, i.e. independent of  $\Delta V_{sd}$ . The full expression for  $W$  is easiest obtained by setting  $\Delta V_{sd} = V_{sd}$ , i.e.  $F = V_{sd}/W$ . The gate bias determines  $p_0$  according to  $p_0 = \frac{\epsilon_0\epsilon_r}{qd\delta}(V_s - V_g)$  with  $\delta$  the thickness of the accumulation layer. Using  $V_s - V_g = V_{sd}/(1 + \mu_h/\mu_e)$  as derived above from current conservation, and the Langevin<sup>13</sup> value for the recombination prefactor  $\gamma = q(\mu_h + \mu_e)/\epsilon_0\epsilon_r$ , one finally finds

$$W = \sqrt{4.34d\delta} \quad (5)$$

Typical values for  $\delta$  are around 1–10 nm,<sup>14</sup> and for  $d$  50 nm – 1  $\mu\text{m}$ , giving  $W$  values in the range 15 – 200 nm. The surprisingly few parameters in (5) reflect the cancellation of (a) the mobility dependence of the drift velocity and recombination rate,

### 3. On the width of the recombination zone in organic light emitting field effect transistors

(b) the dielectric constant dependence of the capacitance and recombination rate and (c) the bias dependence of the carrier density ( $\sim V_g$ ) and drift velocity ( $\sim V_{sd}$ ) since  $V_g$  and  $V_{sd}$  are linked by current conservation as discussed above.

Let us now briefly come back to the ignored effects of carrier diffusion. The broadening of the recombination profile due to diffusion can be estimated from  $W_{diff} \approx \sqrt{D\tau}$ . Here,  $D$  is the diffusion constant, linked to the mobility via the Einstein relation  $D = \mu k_B T / q$  with  $k_B$  the Boltzmann constant and  $T$  the absolute temperature. The recombination time constant  $\tau$  is estimated as  $\tau \approx 1/\gamma n_0$ . With this, the diffusion broadening becomes  $W_{diff} \approx W \sqrt{k_B T / q V_{sd}}$ . Since the square root term is much smaller than unity for all practical devices as  $k_B T / q \approx 25$  meV at room temperature, the diffusion broadening can indeed safely be ignored.

In Fig. 2, the predictions of Eqs. 3-5 are compared to numerical solutions of the coupled drift/diffusion and Poisson equations. The parameters used correspond to the nickel dithiolene (NiDT) devices described in Ref. 10. Clearly, both the height and shape of the recombination profile, and correspondingly the decay of the electron and hole density, are accurately reproduced by the analytical model. In the bottom panel of Fig. 2 the numerically and analytically calculated recombination profiles for three different accumulation layer thicknesses are compared. Indeed, the numerically obtained profile has a width that follows Eq. 5. It should be pointed out that the numerically calculated recombination profile is extremely sensitive to undersampling, i.e. a too coarse calculation grid will result in overestimation of  $W$ , usually without much effect on the calculated current densities. Likely, this explains the large differences between the present results and those in Ref. 15. Our calculated widths do match well with those found by Smith and Ruden.<sup>16</sup>

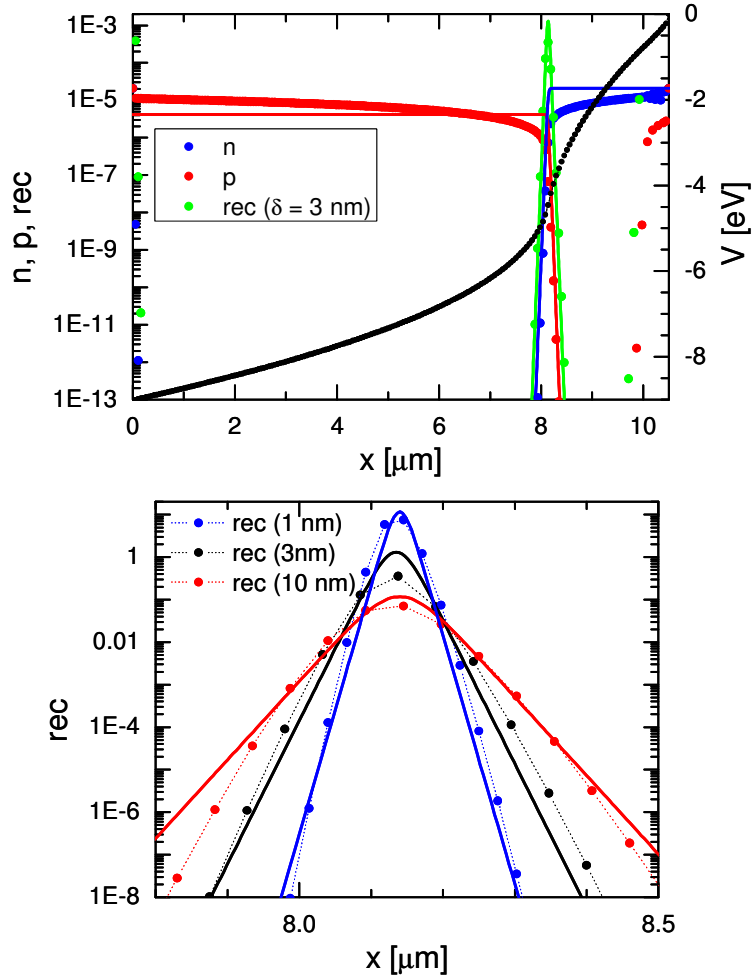


Fig. 2. Top: Electron, hole density and recombination (left axis) and potential (right axis) vs. position in the NiDT channel. Dots: numerical model, lines: Eqs. 3, 4.  $n$  and  $p$  are normalized to the density of states, hence recombination is in units of  $\text{s}^{-1}$ . Parameters used are  $\mu_h = 10^{-11} \text{ m}^2/\text{Vs}$ ,  $\mu_e = 2 \times 10^{-12} \text{ m}^2/\text{Vs}$ ,  $\epsilon_r = 3.6$ ,  $d = 240 \text{ nm}$ ,  $\delta = 3 \text{ nm}$ . Bottom: Zoom-in in the recombination profile for  $\delta = 1, 3$  and  $10 \text{ nm}$ . Symbols + dotted lines: numerical model, solid lines: Eq. 4.

### 3.3 Recombination width of a NiDT field-effect transistor

As mentioned above, the finite spatial resolution of experimental probes prevents a direct comparison with experiments. In particular, the SKPM response is not solely due

### 3. On the width of the recombination zone in organic light emitting field effect transistors

to the interaction between the tip apex and the underlying sample, but results from the complex 3D interaction between the entire probe, consisting of cantilever, cone and apex and the entire sample. We have used a recently developed model to take the full 3D electrostatics into account.<sup>17</sup> These calculations contain no free parameters, the main inputs being the (known) geometry of the tip and sample and the channel potential.

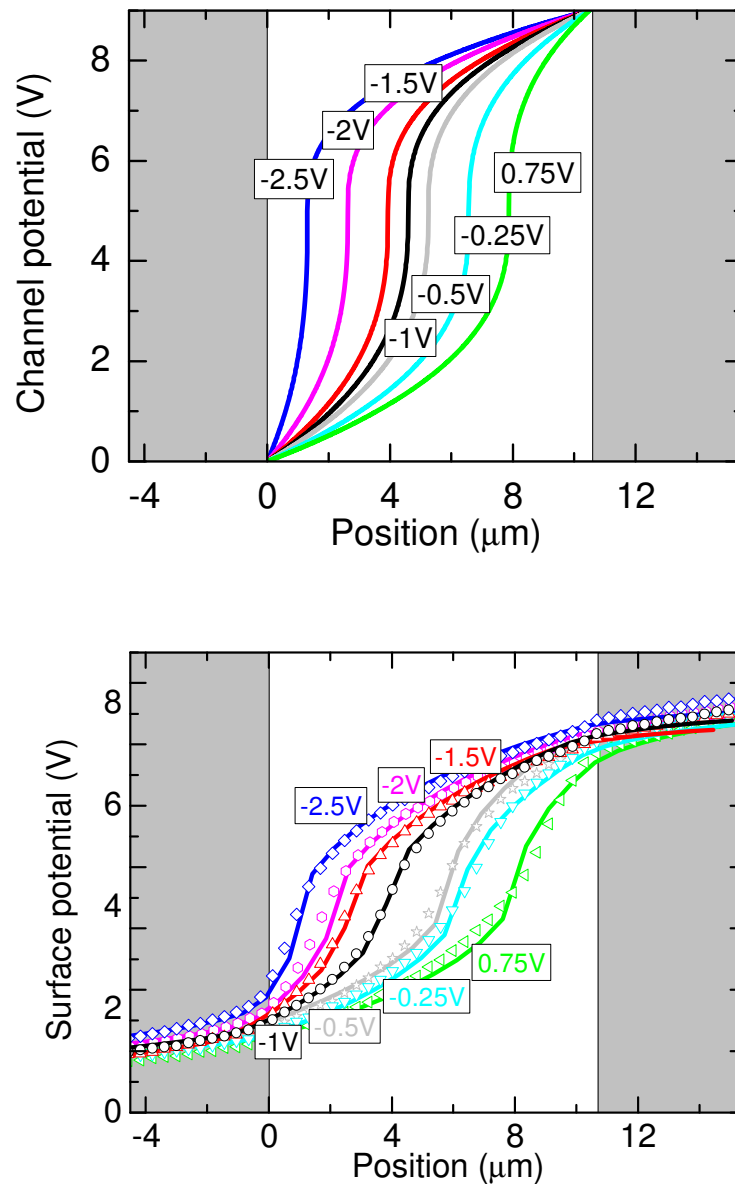


Fig. 3. (a) Potential profiles in the LEFET channel calculated from the analytical model and parameters of Ref. 10. The source-drain voltage is 9 V, the gate voltage is indicated at the corresponding curve. (b) Measured surface potential (symbols) and SKPM response calculated from the curves in (a) (lines).

As input for the channel potential we use the analytical expressions for  $V(x)$  as derived by Smits *et al.*, see Fig. 3a.<sup>10</sup> These calculations are based on variable range hopping in an exponential density of states, and assume  $W = 0$ . The calculation of the surface potential takes only parameters as inputs that are independently determined, i.e. the entire calculation is free of fitting parameters. The calculated surface potentials accurately match the measured ones, as shown in Fig. 3b. Within their error margins, the shapes of the experimental and numerical traces are equal. A detailed analysis of the calculated and measured surface potentials in the recombination region allows us to put an upper limit to the width of the actual recombination zone of less than 0.5  $\mu\text{m}$ .

In order to arrive at values for  $W$  that are in the  $\mu\text{m}$  range, as claimed by Swensen *et al.* on basis of confocal microscopy experiments<sup>9</sup>, the recombination prefactor needs to be set significantly below the Langevin value that is used in this paper. Reducing  $\gamma$  by a factor  $\beta$  ( $\beta < 1$ ) leads to an increase in  $W$  by a factor  $\beta^{1/2}$ .

### 3.4 Conclusion

Summarizing, we have presented an analytical model for the recombination profile in organic ambipolar FETs. The model only depends on experimentally easily accessible parameters and predicts a recombination zone width in the range 15 – 200 nm, which is confirmed by numerical calculations. A detailed analysis of the surface potential obtained by scanning Kelvin probe microscopy on nickel dithiolene LEFET supports the notion of a narrow recombination zone.

### 3.5 References and notes

[1] For a recent review see e.g. J. Zaumseil, and H. Sirringhaus, *Chem. Rev.* **107**, 1296 (2007).

### 3. On the width of the recombination zone in organic light emitting field effect transistors

- [2] T. Takenobu, S.Z. Bisri, T. Takahashi, M. Yahiro, C. Adachi, and Y. Iwasa, *Phys. Rev. Lett.* **100**, 066601 (2008).
- [3] For a recent review see e.g. I.D.W. Samuel, and G. A. Turnbull, *Chem. Rev.* **107**, 1272 (2007).
- [4] J. Zaumseil, R.H. Friend and H. Sirringhaus, *Nature Mater.* **5**, 69 (2006).
- [5] S. Verlaak, D. Cheyns, M. Debucquoy, V. Arkhipov, and P. Heremans, *Appl. Phys. Lett.* **85**, 2405 (2004).
- [6] D.L. Smith and P.P. Ruden, *Appl. Phys. Lett.* **89**, 233519 (2006).
- [7] E.C.P. Smits, T.D. Anthopoulos, S. Setayesh, E. van Veenendaal, R. Coehoorn, P.W.M. Blom, B. de Boer, and D.M. de Leeuw, *Phys. Rev. B* **73**, 205316 (2006).
- [8] R. Schmechel, M. Ahles and H. von Seggern, *J. Appl. Phys.* **98**, 084511 (2005).
- [9] J.S. Swensen, J. Yuen, D. Gargas, S.K. Buratto, and A.J. Heeger, *J. Appl. Phys.* **102**, 013103 (2007).
- [10] E.C.P. Smits, S.G.J. Mathijssen, M. Cölle, A.J.G. Mank, P.A. Bobbert, P.W.M. Blom, B. de Boer, and D.M. de Leeuw, *Phys. Rev. B* **76**, 125202 (2007).
- [11] For this problem, only the capture rate of positive and negative charges matters, the question whether subsequent recombination is emissive or not is irrelevant. Hence the model is valid for any ambipolar field effect transistor.
- [12] S.M. Sze, *Physics of Semiconductor Devices*, 2nd edition, Wiley, New York, 1981.
- [13] P. Langevin, *Ann. Chim. Phys., serie 7*, 433 (1903).
- [14] G. Horowitz, R. Hajlaoui and P. Delannoy, *J. de Physique III* **5**, 355 (1995).
- [15] G. Paasch, T. Lindner, C. Rost-Bietsch, S. Karg, W. Riess, and S. Scheinert, *J. Appl. Phys.* **98**, 084505 (2005).
- [16] D.L. Smith, and P. P. Ruden, *J. Appl. Phys.* **101**, 084503 (2007).
- [17] D.S.H. Charrier, M. Kemerink, B.E. Smalbrugge, T. de Vries, and R.A.J. Janssen, *ACS Nano* **2**, 622 (2008).



## Chapter 4

# Bimolecular recombination in ambipolar organic field effect transistors

### 4.1 Introduction

At present, there is significant debate on the strength of bimolecular recombination in organic semiconducting materials.<sup>1</sup> Not only does this issue relate to our understanding of fundamental processes in a large class of disordered materials, but it also translates directly into device performance. A device type in which the bimolecular recombination strength is of great relevance is the recently developed organic light emitting field effect transistor (LEFET).<sup>2</sup> The high current densities in these devices<sup>3</sup> as compared to those in diode-type devices may help to reach population inversion, which is a prerequisite for an electrically driven organic laser,<sup>4-6</sup> and may offer significant advantages for lighting applications. However, the high carrier and exciton densities in LEFET may also enhance exciton quenching, reducing the internal quantum efficiency.<sup>3,7</sup> As such, knowledge of the actual exciton density is crucial. The latter is directly related to the width of the recombination zone  $W$ , which in turn, is governed by the bimolecular recombination strength  $\gamma$ . In the previous chapter we have shown that  $W$  is given by<sup>8</sup>

$$W = \sqrt{4.34d\delta/\beta} \quad (1)$$

with  $d$  and  $\delta$  the thickness of the gate dielectric and the accumulation layer, respectively. The parameter  $\beta$  is defined as  $\gamma = \beta\gamma_L$  with  $\gamma_L$  the Langevin recombination strength. Reported values for  $\beta$  vary from around unity to orders of magnitude below unity.<sup>1</sup>

In this chapter, we present a detailed analysis of surface potential profiles as measured by scanning Kelvin probe microscopy (SKPM) on a prototypical ambipolar oFET. We find  $W = 0.5 \mu\text{m}$ , which translates into  $\beta = 10^{-2}$ , in good agreement with recent theoretical predictions.<sup>1</sup>

Before turning to the results obtained on oFETs, we need to discuss the methodology that enabled us to directly compare experimental surface potentials to theoretical model predictions.

Scanning Kelvin probe microscopy (SKPM) offers the unique possibility to look inside operational electronic devices on truly nanoscopic length scales.<sup>9</sup> A drawback of SKPM is that the obtained potential traces do not reflect the real surface potential  $V(x)$  but rather a convolution of  $V(x)$  with a usually unknown instrument response function.<sup>10-14</sup> The physical reason for this is that not only the tip apex contributes to the signal but the entire metalized tip, consisting of apex, cone and lever, interacts with the sample due to the relatively long range of the electrostatic force.<sup>15</sup> As a result, the obtained surface potentials are distorted in both shape and magnitude; the error in the latter may exceed 60%. To surmount these intrinsic SKPM limitations, two fundamentally different approaches are possible, i.e. prediction and reconstruction.

Prediction methods aim to convolute a ‘real’ surface potential, which e.g. follows from theoretical considerations, with a theoretically or experimentally known tip response. So far, all reported prediction methods are based on a theoretical tip response.<sup>10,11,15</sup> Reconstruction methods aim to deconvolute the experimental surface potential with a theoretically or experimentally known response function in order to extract the real surface potential.<sup>12,13</sup>

For our present purposes, we developed a flexible and convenient method for both predicting and reconstructing SKPM surface potentials. In contrast to previous studies, the entire instrument response is contained in an *experimentally* determined transfer function. Hence, there is no need to explicitly evaluate the electrostatic interactions using either (approximate) analytical expressions<sup>10,11,12,16</sup> or brute force numerics.<sup>15</sup> The method is equally valid for SKPM based on electrostatic force detection, as employed here, as for SKPM based on force gradient detection.<sup>16</sup>

#### 4. Bimolecular recombination in ambipolar organic field effect transistors

The hypothesis underlying the (re)construction of SKPM measurements is that the measured surface potential  $y$  is a convolution of the real surface potential  $x$  with a transfer function  $h$ , i.e.  $y = h \otimes x$ . In general,  $h$  will depend on the tip geometry, its orientation with respect to the sample and the vertical distance from the sample. Since all electrostatic forces are implicitly contained in the transfer function  $h$  there is no need to quantify any electrostatic forces. From the convolution theorem we then have<sup>17</sup>

$$F(y) = F(h)F(x) \quad (2)$$

where  $F$  indicates the Fourier transform. The transfer function  $h$  is experimentally determined from a reference measurement. This is most conveniently done on a step edge, for which case the mathematical link between  $x_{step}$ ,  $y_{step}$  and  $h$  is simply

$$F(h) = F(y'_{step}) \quad (3).$$

where the prime denotes the spatial derivative along the axis of measurement. Eq. (3) follows by applying (2) to the step edge,  $F(y_{step}) = F(h)F(x_{step})$ . Using the property  $F(y') = i\omega F(y)$  and taking the spatial derivative of both  $x_{step}$  and  $y_{step}$ , one obtains  $F(y'_{step}) = F(h)F(x'_{step})$ . This reduces to (3) by using  $x'_{step} = \delta$  with  $\delta$  the Dirac delta function and  $F(\delta) = 1$ . Once the transfer function  $h$  of a particular configuration is determined, any experimental surface potential can be inverted to obtain the 'real' surface potential  $x$  using  $x = F^{-1}(F(y)/F(h))$  and similarly for prediction from a known  $x$ . Here,  $F^{-1}$  denotes the inverse Fourier transform. Numerical implementation of these equations is relatively straightforward.<sup>18</sup>

#### 4.2 Materials and methods

To be applicable to thin film oFETs, the transfer function  $h$  should formally be determined on a step buried under a dielectric layer. However, electrostatic finite element

calculations (not shown) indicate that the effect of a  $\sim 100$  nm thick polymer layer with  $\epsilon_r \approx 3$  on the surface potential is negligible as compared to the experimental uncertainty. The polymer layer acts as a spacer.

To experimentally determine the step edge response, we made a step edge of a few monolayers of Ti on Au, see top inset of Fig. 1. These reference samples were manufactured using standard UV photolithography. Starting from chemically cleaned silicon wafers with 200 nm of thermal  $\text{SiO}_2$  on top, 5 nm of Ti as adhesion layer and 25 nm of Au were subsequently deposited by electron beam evaporation under high vacuum conditions. A classical lift-off procedure was employed to pattern a second Ti layer on top of the Au. The SKPM-AFM was a Veeco / Dimension 3100/ extended Nanoscope IIIa working in lift mode under ambient conditions. We used Pt-coated Si tips (Olympus OMCL-AC240TM-B2,  $f_0 \approx 70$  kHz,  $k \approx 2$  N/m,  $R_{\text{apex}} < 25$  nm).

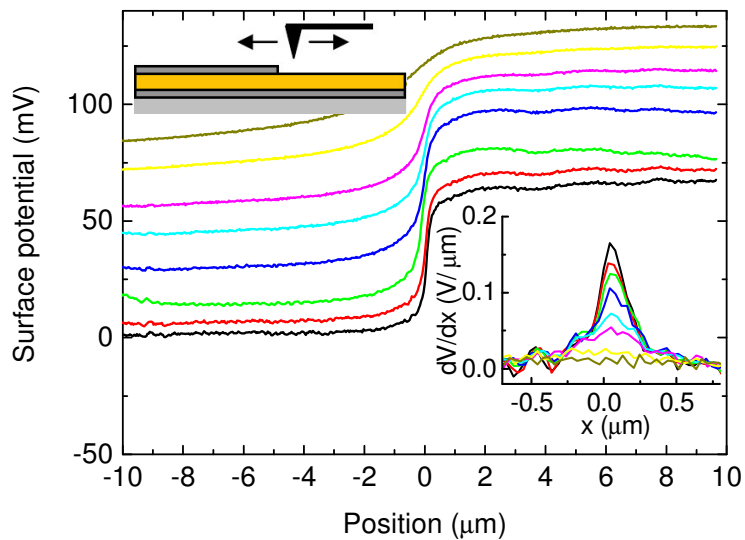


Fig. 1: Main panel: SKPM step edge response with the tip orthogonal to the channel for different lift heights, lines are the measured surface potential over the step edge at  $z_{\text{lift}} = 0, 25, 50, 100, 150, 200, 500, 1000$  nm. Top inset: layout of step edge sample. Right inset: transfer function  $h$  for different  $z_{\text{lift}}$ .

The main panel of Fig. 1 shows typical SKPM measurements on the Ti:Au step edge for different lift heights  $z_{\text{lift}}$ . The relatively small difference in work functions

#### 4. Bimolecular recombination in ambipolar organic field effect transistors

observed between Ti and Au is due to the ambient conditions during the experiments, but the actual step height does not affect the procedure. The right inset is the transfer function  $h$  for increasing lift height. The increasing width with increasing lift height reflects the obvious loss in spatial resolution. Moreover, the asymmetric shape of  $h$  is due to the asymmetric measurement configuration in which the cantilever is oriented perpendicular to the step edge. An orientation parallel to the edge yields a symmetric  $h$ .<sup>15</sup>

#### 4.3 Results and discussion

We now return to the problem of measuring the actual recombination profile in an ambipolar oFET. The methodology described above was applied to surface potentials measured by SKPM on ambipolar oFETs that have been extensively described before.<sup>8,19</sup> In short, these devices consist of a thin nickel dithiolene (NiDT) layer on a Si/SiO<sub>2</sub> (230 nm) substrate with Ti/Au bottom contacts in a ring transistor configuration with a channel width and length of 2500  $\mu\text{m}$  and 10  $\mu\text{m}$ , respectively, see inset to Fig. 2. By choosing proper bias conditions electron and hole accumulation regions, separated by a recombination zone, are simultaneously present. Electron and hole mobilities that are used in the numerical drift-diffusion calculations discussed below are obtained from transport characteristics and equal  $1 \times 10^{-11}$  and  $2 \times 10^{-12}$   $\text{m}^2/\text{V}$  for holes and electrons, respectively.

In Fig. 2 two different prediction methods are applied to a representative surface potential as measured by SKPM on the NiDT ambipolar transistor. The required input signal,  $x$  in (2), is calculated from the variable range hopping model discussed in Ref. 19 using  $V_g - V_{th} = 5.3$  V and  $V_{sd} = 9$  V and is shown as blue line. It is important to point out that this model assumes  $W = 0$ , i.e.  $\beta = \infty$ . From that, the black line is calculated using (2) with a transfer function  $h$  obtained from (3) as discussed above. Clearly, the predicted curve follows the experimental one closely. For comparison we also used a computationally much more demanding 3D finite element model to predict the SKPM response of  $x$ .<sup>15</sup> The result is shown as red line, and is in close agreement with the much easier obtained result of (2). From this we conclude that the transfer function method

provides a convenient way to transform a known surface potential into an actual SKPM response. However, a close inspection of both curves in the recombination zone reveals a maximum field that is significantly higher than observed experimentally. Below, this will be related to the nonzero value of  $W$ .

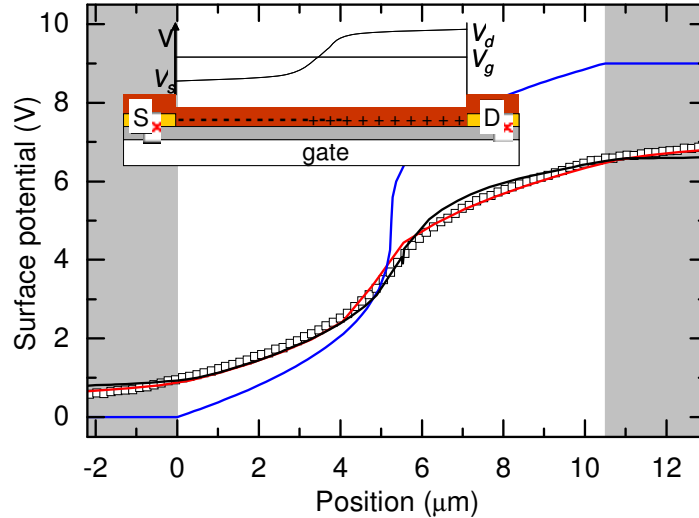


Fig. 2: Comparison of surface potential prediction methods applied to an ambipolar OFET. Symbols: experiment taken for  $V_{sd} = 9$  V and  $V_g - V_{th} = 5.3$  V at  $z_{lift} = 100$  nm; lines: transfer function method (black), 3D numerical (red) and theoretical potential used as input (blue). Inset: schematic layout of the ambipolar OFET. When  $0 < V_g - V_{th} < V_{sd}$  with  $V_g$ ,  $V_{th}$  and  $V_{sd}$  the gate, threshold and source-drain voltage respectively, electron and hole accumulation layers form on the left and right of a recombination zone, respectively. The source is grounded.

In Fig. 3, the experimental curve and its reconstructed surface potential are compared to the theoretical surface potential for again  $V_g - V_{th} = 5.3$  V and  $V_{sd} = 9$  V. Both the magnitude reduction of the experimental curve and most of its asymmetric distortion due to the asymmetric tip-channel orientation are correctly undone. However, the infinite field at the point where n- and p-type accumulation regions meet, as implicitly assumed in the model of Ref 19, is not observed. At this point, it is tempting to take the width of the derivative profile of the reconstructed surface potential, shown as thin black line in the insets of Fig. 3, as a measure of the actual recombination zone width  $W$ . However,

#### 4. Bimolecular recombination in ambipolar organic field effect transistors

despite the fact that the analytical model underlying (1) correctly predicts the recombination profile, it makes no predictions of the corresponding potential profile, and the widths of the two profiles are usually not equal.<sup>8</sup> Hence we performed a numerical drift-diffusion analysis as outlined in Ref. 8, and compared the (spatial derivative of the) resulting potential profiles to the reconstructed experimental profile, as shown in the lower inset of Fig. 3. We find optimal agreement between the two derivative profiles when parameters that give rise to a recombination zone width of 0.5  $\mu\text{m}$  are used. With  $d = 200$  nm and estimating  $\delta = 3$  nm, it follows from (1) that  $\beta \approx 10^{-2}$ , which is also used in the numerical calculations.

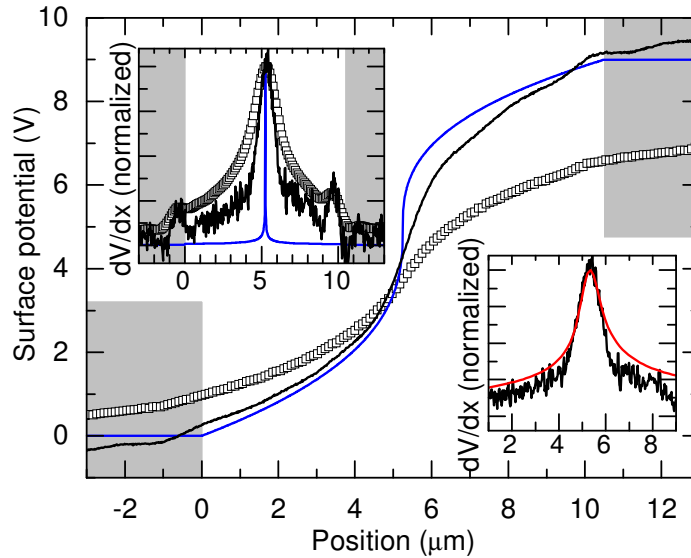


Fig. 3: Reconstruction of the surface potential of an ambipolar oFET. Symbols: experiment taken for  $V_{sd} = 9$  V and  $V_g - V_{th} = 5.3$  V at  $z_{lift} = 100$  nm; lines: transfer function method (black) and theoretical potential as calculated according to Ref. 19 (blue). Upper inset: normalized first derivative of the curves in the main panel. Lower inset: zoom-in on reconstructed first derivative profile (black) and calculated profile for a recombination zone width of 0.5  $\mu\text{m}$  (red).

This implies that the bimolecular recombination rate is two orders of magnitude below the value predicted by the Langevin expression. This finding is in good agreement

with the results from Monte Carlo simulations by Groves and Greenham,<sup>1</sup> who find values for  $\beta$  between  $10^{-1}$  and  $10^{-2}$  for similar parameters as in the present experiment. Indeed, they showed that by shrinking the dimensionality from 3D (bulk) to 2D (planar device as LEFET)  $\beta$  also decreases, and this is checked for different carrier densities.  $\beta$  decreases while the effective intercarrier spacing for a given charge density increases as transport in one dimension is increasingly constrained.

#### 4.4 Conclusion

Summarizing, we presented a practical method for prediction and reconstruction of surface potentials measured by SKPM. The method is based on (de)convolution with a transfer function containing the whole electrostatic tip-sample coupling. The transfer function is experimentally calibrated on an ‘ideal’ step edge. Using this method we determined a recombination zone width of 0.5  $\mu\text{m}$  for a NiDT ambipolar oFET, indicating a bimolecular recombination rate that is two orders of magnitude below the Langevin value.

#### 4.5 References and notes

- [1] See e.g. C. Groves, and N.C. Greenham, *Phys. Rev. B* **78**, 155205 (2008) and references therein.
- [2] For a recent review see e.g. J. Zaumseil, and H. Sirringhaus, *Chem. Rev.* **107**, 1296 (2007).
- [3] T. Takenobu, S.Z. Bisri, T. Takahashi, M. Yahiro, C. Adachi, and Y. Iwasa, *Phys. Rev. Lett.* **100**, 066601 (2008).
- [4] For a recent review see e.g. I. D. W. Samuel, and G. A. Turnbull, *Chem. Rev.* **107**, 1272 (2007).
- [5] R.C.G. Naber, M. Bird, and H. Sirringhaus, *Appl. Phys. Lett.* **93**, 023301 (2008).

#### 4. Bimolecular recombination in ambipolar organic field effect transistors

- [6] E.B. Namdas, M. Tong, P. Ledochowitsch, S.R. Mednick, J.D. Yuen, D. Moses, and A.J. Heeger, *Adv. Mater.* **21**, 799-802 (2009).
- [7] S. Verlaak, D. Cheyns, M. Debucquoy, V. Arkhipov, and P. Heremans, *Appl. Phys. Lett.* **85**, 2405 (2004).
- [8] M. Kemerink, D.S.H. Charrier, E.C.P. Smits, S.G.J. Mathijssen, D.M. de Leeuw, and R.A.J. Janssen, *Appl. Phys. Lett.* **93**, 033312 (2008).
- [9] M. Nonnenmacher, M. P. O'Boyle, and H.K. Wickramasinghe, *Appl. Phys. Lett.* **58**, 2921 (1991).
- [10] Y. Shen, D.M. Barnett, and P.M. Pinsky, *Rev. Sci. Instrum.* **79**, 023711 (2008).
- [11] A. Liscio, V. Palermo, and P. Samori, *Adv. Funct. Mater.* **18**, 907 (2008).
- [12] E. Strassburg, A. Boag, and Y. Rosenwaks, *Rev. Sci. Instrum.* **76**, 083705 (2005).
- [13] A. Schwartzman, E. Grunbaum, E. Strassburg, E. Lepkifker, A. Boag, Y. Rosenwaks, Th. Glatzel, Z. Barkay, M. Mazzer, and K. Barnham, *J. Appl. Phys.* **98**, 084310 (2005).
- [14] H.O. Jacobs, P. Leuchtmann, O.J. Homan, and A. Stemmer, *J. Appl. Phys.* **84**, 1168 (1998).
- [15] D.S.H. Charrier, M. Kemerink, B.E. Smalbrugge, T. de Vries, and R.A.J. Janssen, *ACS Nano* **2**, 622 (2008).
- [16] A. Gil, J. Colchero, J. Gómez-Herrero, and A.M. Baró, *Nanotechnology* **14**, 332 (2003).
- [17] E.O. Brigham, *The Fast Fourier Transform and its applications* (Prentice-Hall, Englewood Cliffs, 1988).
- [18] Numerical noise and spurious peaks in FFT signals could greatly be reduced by making all discrete signals  $X_N = (x_1, \dots, x_N)$  periodic by extending them to  $X_{2N} = (x_1, \dots, x_N, \dots, x_1)$ . To avoid extrapolation to low frequencies in Fourier space, the size of the reference scan was at least the size of the to-be-converted measurement of calculation. In the inversion procedure, a high frequency cutoff was used to avoid division-by-zero errors at frequencies where  $F(h)$  is close to zero.
- [19] E.C.P. Smits, S.G.J. Mathijssen, M. Cölle, A.J.G. Mank, P.A. Bobbert, P.W.M. Blom, B. de Boer, and D.M. de Leeuw, *Phys. Rev. B* **76**, 125202 (2007).



## Chapter 5

# Scanning tunneling microscopy via the accumulation layer of *p*-type organic field-effect transistors

### 5.1 Introduction

The ultimate method to do potentiometry on organic semiconductors is scanning tunneling potentiometry<sup>1</sup> (STP), a technique that is derived from scanning tunneling microscopy (STM). In principle, STP allows surface potentials to be measured with a sub-nanometer spatial resolution. For comparison, scanning Kelvin probe microscopy (SKPM) has a resolution at around 100 nm.<sup>2</sup> The nature of the underlying interactions explains the difference in resolution. SKPM extracts surface potentials from the electrostatic interaction between tip and sample, which is in principle long-range. In contrast, STP probes the electrochemical potential via a tunneling current, which depends exponentially on distance with a decay length in the order of Angstroms. Using the SKPM technique, surface potentials were obtained on both unipolar<sup>3</sup> and ambipolar<sup>4</sup> organic field-effect transistors (oFETs).

So far, the use of STM on conjugated materials was largely restricted to the measurement of topographic images of organic (mono)layers on metallic substrates. E.g. regioregular poly(3-alkylthiophene)s on graphite,<sup>5,6</sup> and a quaterthiophene (DFH-4T)<sup>7</sup> on Au(111) were successfully imaged. Besides topography, giving the molecular arrangement, information on the local density of states can be obtained in the scanning tunneling spectroscopy (STS) mode.<sup>8</sup> STS spectra of pentacene monolayers on Au were confronted with transport models.<sup>9</sup> STS was further used on disordered organic semiconductors to measure internal potentials and single particle gaps.<sup>10</sup> Prerequisites of

STS and STP are high signal-to-noise ratio of tunnel current. So far, STM on oFETs has not been reported. In this chapter, we will demonstrate the first step towards STP on oFETs by showing stable STM operation on the channel region of an operational pentacene transistor using the accumulation layer effectively as conducting substrate.

Due to the geometry of an oFET, the channel of bottom gate devices can be probed while gate and source-drain biases are applied. The STM bias ( $V_{bias}$ ) is applied between the source, which acts as reference for the device, and the STM tip, which is (virtually) grounded via the current amplifier (Fig. 1a). Two currents pathways can be involved in STM operation as illustrated in Fig. 1b: a pathway via the bulk of the organic semiconductor from the tip to the source (or drain) contact or a pathway via the accumulation layer at the interface with the gate dielectric. In both pathways tunneling through the vacuum gap is the first step. In order to reach maximum sensitivity to the local properties of the channel, the indirect pathway should dominate. Moreover, to enable imaging of the true topography by STM, which is not trivial for larger film thicknesses,<sup>10</sup> a tunneling gap should be present. Hence, the resistance associated with the vertical ( $R_{vert}$ ) and lateral ( $R_{lat}$ ) pathway must be significantly below the value associated with the STM setpoint, i.e.  $R_{vert} + R_{lat} \ll V_{bias}/I_{tunnel}$ .

## 5.2 Materials and methods

In this work, the device is a pentacene-based oFET. The substrate consists of highly-doped Si, acting as bottom gate, with a 200 nm thick thermal SiO<sub>2</sub> layer on top as gate dielectric. Bottom source and drain contacts are made from Au/Ti (25 nm/5 nm) by standard UV-lithography. Channel lengths  $L$  vary from 1  $\mu\text{m}$  to 20  $\mu\text{m}$ . Prior to pentacene deposition, the dielectric surface was treated with HMDS. The pentacene is evaporated at 150 °C in vacuum ( $10^{-7}$  mbar) at 0.4  $\text{\AA}/\text{s}$ . As expected, the 20 nm thick pentacene layer on SiO<sub>2</sub> shows large crystals and terraces in pyramidal shapes with 1.4 nm step edge height under AFM. Several layer thicknesses were checked in terms of image quality. For STM, the layer must be fully covered to avoid tip crashes on the non-conducting SiO<sub>2</sub>. On the other hand, thicker layers lead to a higher  $R_{vert}$ , which can cause

## 5. Scanning tunneling microscopy via the accumulation layer of *p*-type organic field effect transistors

unstable imaging as explained above. The best compromise was found for a thickness of 20 nm. For this thickness we measure a mobility of about  $0.18 \text{ cm}^2/\text{Vs}$  in ambient conditions. Because of the ambient conditions used in the experiments, the threshold voltage was around  $V_{th} \approx 6 \text{ V}$  for a fresh device. Since oxygen ( $\text{O}_2$ ) doping of pentacene increases its conductivity,<sup>11</sup> the ambient conditions used in the STM might enhance current path 1 through the bulk, while part 2 runs through the bulk only for a short distance. Below, we show that the contribution of path 1 is still negligible.

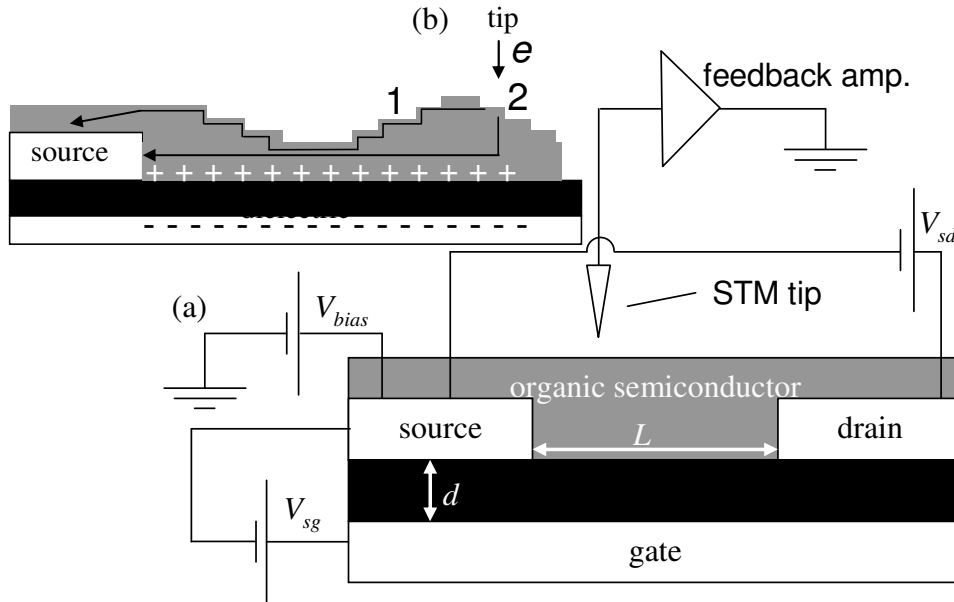


Fig. 1 (a): Schematic drawing of STM and external power supplies wiring. (b): two possible paths for the tip-source current. See text for further discussion.

STM experiments were performed using a Veeco Multimode AFM with Nanoscope IIIa controller used in STM mode. The tips were cut from Pt/Ir wire. Source-drain ( $V_{sd}$ ) and source-gate ( $V_{sg}$ ) biases were applied with two (floating) Keithley 2400 source-measure units. The STM bias was applied by the microscope controller. During STM scanning  $V_{sd}$  and  $V_{sg}$  were continuously applied; this continuous stressing of the device caused a decrease in source-drain current  $I_{sd}$  by 30% after 2 h. The AFM was performed with a Veeco Dimension 3100 AFM with Nanoscope IIIa controller. We used Nanosensors tips (PPP-NCHR-50, 330 kHz resonance frequency, and  $\sim 42 \text{ N/m}$  spring constant).

### 5.3 Results and discussion

The STM images taken on a pentacene oFET in the accumulation regime ( $V_{sg} - V_{th} = -12$  V and  $V_{sd} = 0$  V) are shown in Figs. 2 a) and b). The STM settings were  $V_{bias} = 200$  mV and  $I_{tunnel} = 1.2$  pA. In Fig. 2a, the source and drain electrodes are indicated; their nominal height of 30 nm is found back both in AFM and STM. In Fig. 2b, an STM image is taken in the channel region, i.e. on SiO<sub>2</sub>. The observed pentacene grain sizes of around 200 nm are consistent with those observed by AFM in Fig. 2d.

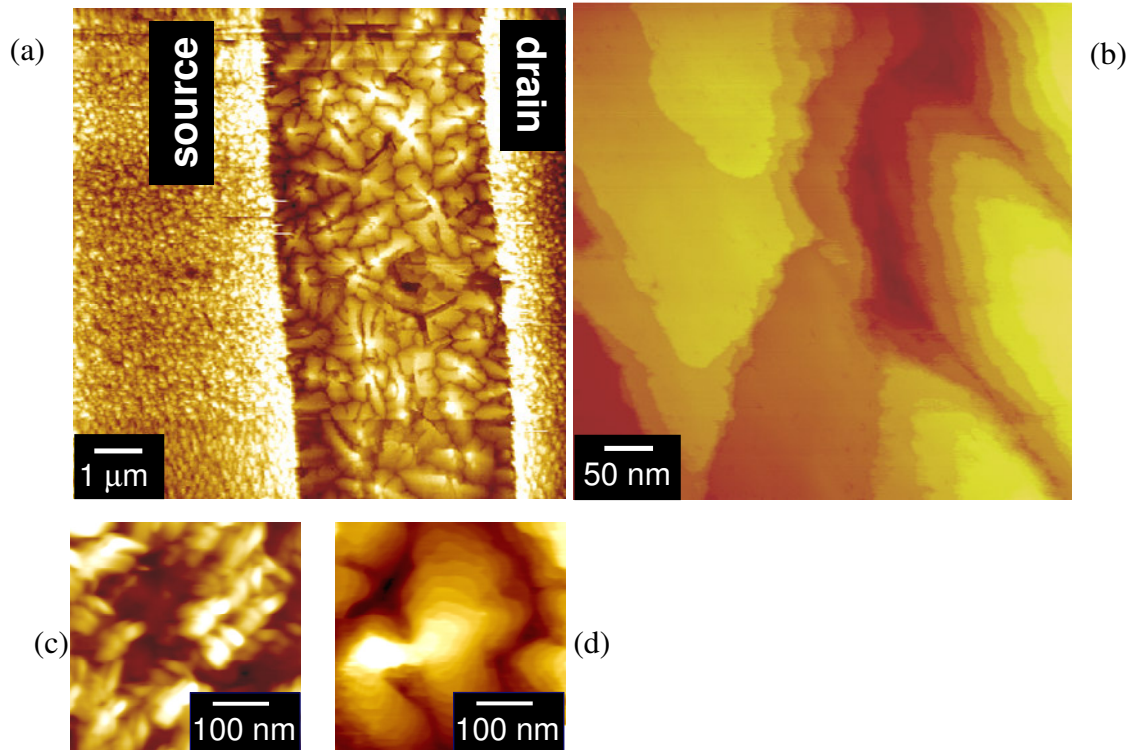


Fig. 2: STM pictures at  $V_{bias} = 200$  mV,  $I_{tunnel} = 1.2$  pA,  $V_{sg} - V_{th} = -12$  V and  $V_{sd} = 0$  V of (a) a bottom contact pentacene field effect transistor and (b) a zoom in the channel region. AFM pictures of (c) pentacene on Au and (d) pentacene on SiO<sub>2</sub>. In all images, the pentacene layer is 20 nm thick. The vertical scales are (a) 50 nm and (b-d) 25 nm.

The same holds for the smaller pentacene grain sizes ( $\sim 40 - 200$  nm) as observed on the Au contacts in Fig. 2c. Finally, the measured terrace height in both AFM and STM

## 5. Scanning tunneling microscopy via the accumulation layer of *p*-type organic field effect transistors

is exactly 1.4 nm which is the length of the pentacene molecule in upright stacking. We therefore conclude that stable STM images can be taken at both large and small scan sizes.

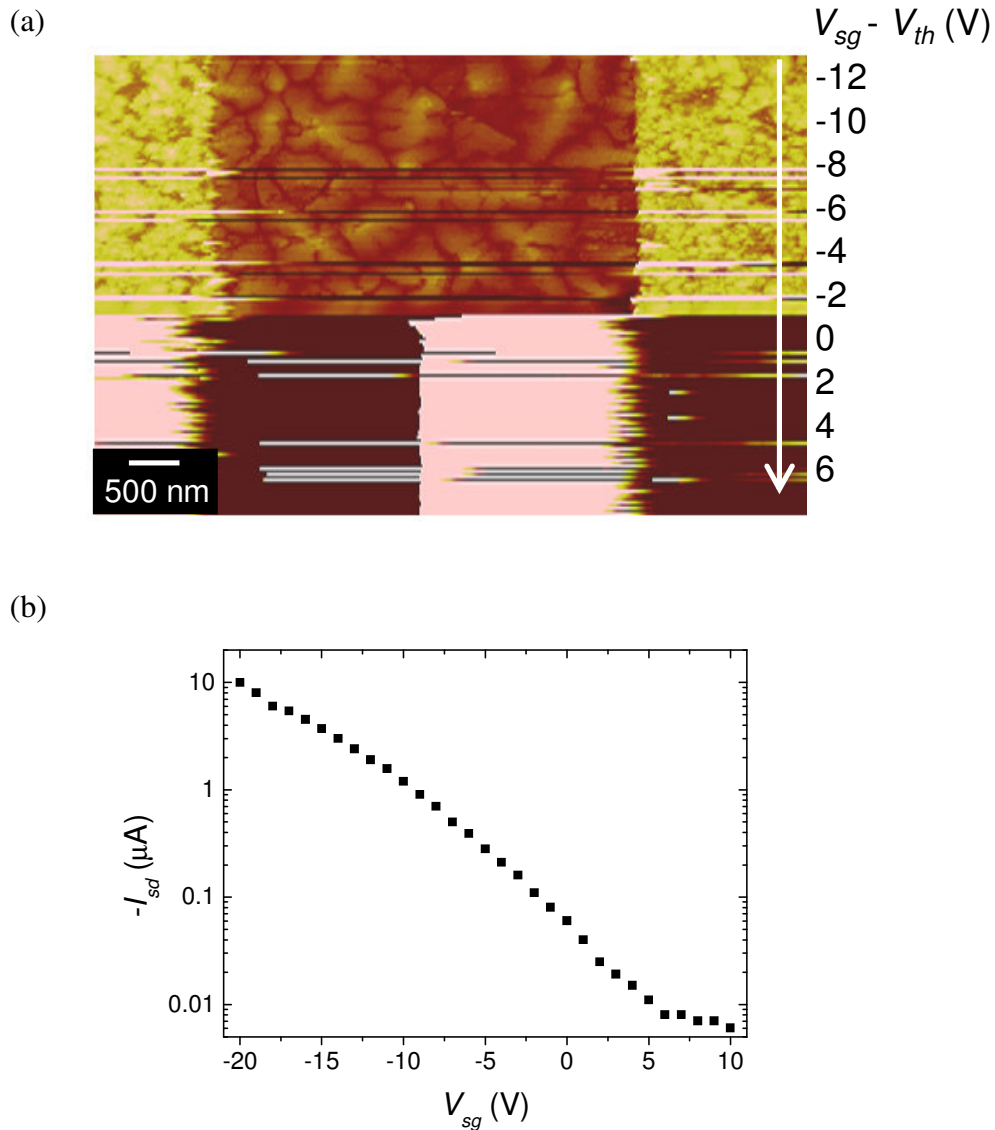


Fig. 3: Tip crash and proof of concept. (a) STM picture at  $V_{bias} = 200$  mV and  $I_{tunnel} = 1$  pA, while sweeping the gate bias from  $V_{sg} - V_{th} = -12$  V (accumulation) to  $V_{sg} - V_{th} = +6$  V (depletion). Downward arrow: scan direction and used gate bias.  $V_{sd} = 0$  V (b) In situ transfer curve, taken immediately after the tip crash,  $V_{sd} = -15$  V.

In order to distinguish the two possible current paths discussed above (Fig. 1b), a continuous STM measurement was performed while slowly increasing  $V_{sg}$ , i.e. while going from the accumulation to the depletion regime. In case the accumulation layer (path 2) is involved in the charge transport, a tip crash is expected around the threshold voltage where in Fig. 3a the result of such an experiment is shown. Well in accumulation ( $V_{sg} \ll V_{th} = 6$  V), stable imaging is possible. In the vicinity of the threshold voltage ( $V_{sg} \approx V_{th} = 6$  V), white lines appear in the image, suggesting a collapse of the tunneling gap, causing occasional tip-surface contact. Clearly the tip completely crashes at  $V_{sg} > V_{th} = 6$  V, i.e. in the off regime. Both regimes are clearly identifiable in the in-situ transfer curve shown in Fig. 3b. From this experiment we conclude that the large majority of the tunneling current is transported to the electrodes via the accumulation layer. As discussed above, this is a prerequisite for high-resolution potentiometry.

In view of the above, it may appear surprising that also in the saturation regime ( $V_{bias} = 200$  mV,  $V_{sg} - V_{th} = -9$  V, and  $V_{sd} = -15$  V) relatively stable STM images of the entire channel, including the pinch-off region, could be taken (Fig. 4).

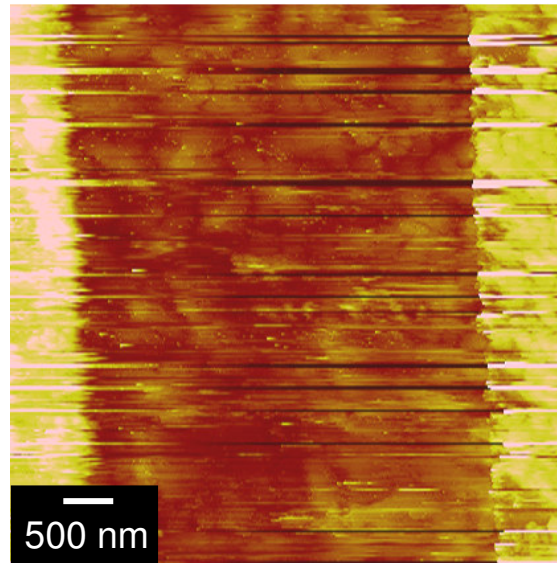


Fig. 4: STM picture at  $V_{bias} = 200$  mV,  $I_{tunnel} = 1$  pA,  $V_{sg} - V_{th} = -9$  V and  $V_{sd} = -15$  V (saturation regime) of a bottom contact pentacene field effect transistor. The vertical scale is 100 nm.

## 5. Scanning tunneling microscopy via the accumulation layer of *p*-type organic field effect transistors

However, an occasional tip-surface contact seemed to occur. This can qualitatively be understood from the fact that stable imaging in the saturation regime should be possible when the current density injected from the tip is small as compared to that in the channel. Under the conditions used, i.e. a 0.2  $\mu\text{A}$  current and a 7 mm wide channel, the surface current density in the channel is around  $3 \times 10^{-5}$  A/m, so the above criterion translates into a minimal width of the  $I_{\text{tunnel}} = 1$  pA tip current at the accumulation layer of about 35 nm. For an average layer thickness of 20 nm, a spread of a few tens of nm seems to be at the edge of what can be considered to be realistic. Hence, an occasional tip-surface contact is to be expected, in line with experimental observations. This spreading width is also the maximum attainable spatial resolution in STP. A value of 35 nm is about a factor three better than what can be reached with SKPM. Hence, for optimal resolution current spreading should be suppressed and the organic layer thickness should be as thin as possible. Although the latter also holds for SKPM, there is an important difference between SKPM and STM. In the former technique, resolution is limited by long range electrostatic interactions, which hardly change for very thin films, see Chapter 4. Hence, reducing the film thickness to the nm level is expected to have a much bigger effect on the STP resolution than on the SKPM resolution.

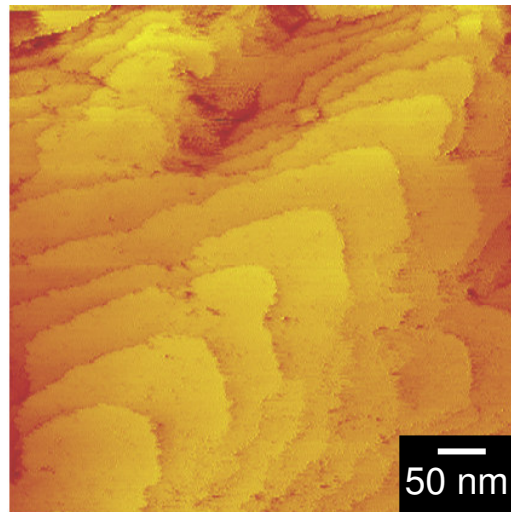


Fig. 5: STM picture at  $V_{\text{bias}} = -200$  mV,  $I_{\text{tunnel}} = 1$  pA,  $V_{\text{sg}} - V_{\text{th}} = -12$  V and  $V_{\text{sd}} = 0$  V in the channel region. The vertical scale is 30 nm.

At negative tip bias ( $V_{bias} = -200$  mV), identical STM topographies were obtained (Fig. 5) as for positive bias, i.e.  $V_{bias} = +200$  mV. This implies the tunneling current can run in both directions, which in turn can be explained by the band diagrams in Fig. 6.

In Fig. 6a, the band diagram is shown at zero sample bias  $V_{bias} = 0$  V, with the p-type oFET in accumulation, i.e.  $V_{sg} < 0$  V. From left to right tip, vacuum, pentacene (PC), gate dielectric and gate are shown. For the metallic tip and gate, the vacuum energy  $E_{vac}$  and the work functions  $\chi_{tip}$  and  $\chi_{gate}$  define the Fermi level of tip and gate as  $\epsilon_{tip} = E_{vac} - \chi_{tip}$  and  $\epsilon_{gate} = E_{vac} - \chi_{gate}$ , respectively. The tunnel gap (vacuum) of distance  $d$  separates the tip from the pentacene semiconductor. The gate dielectric is insulating and has a dielectric constant that for simplicity is taken equal to that of pentacene. The Fermi level in the pentacene channel,  $\epsilon_{channel}$  is determined by the source and drain Fermi levels. For simplicity, we assume  $V_{sd} = 0$  V in this discussion. For  $V_{bias} = 0$  V, the tip, pentacene and gate Fermi levels are energetically aligned. The effect of a negative gate voltage  $V_{sg}$  is shown in Fig. 6a. Close to the dielectric, the accumulated holes screen  $V_{sg}$ .

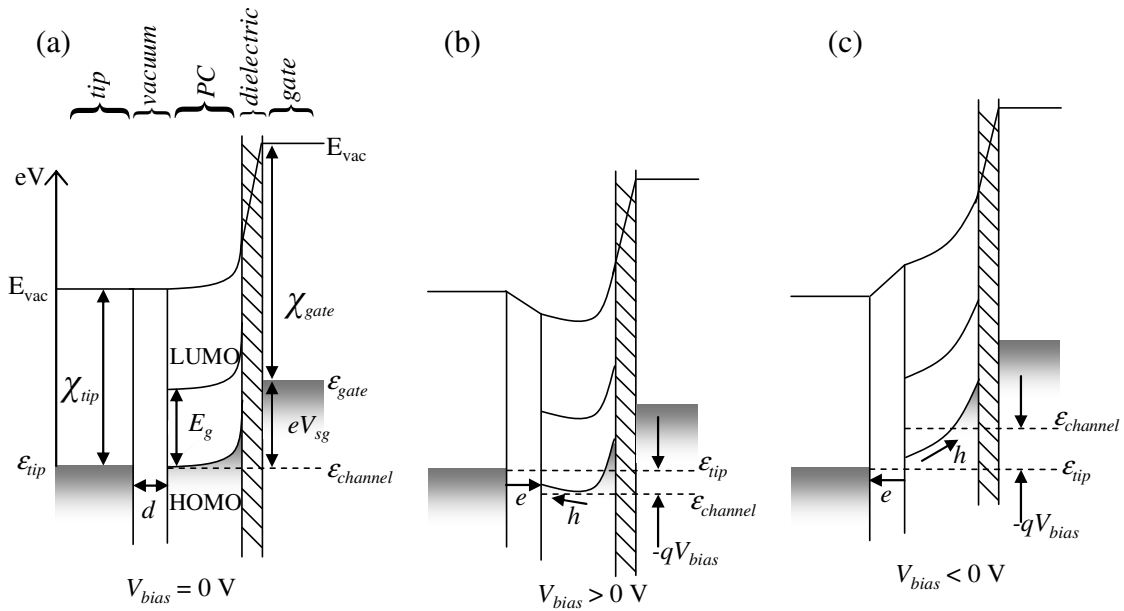


Fig. 6: Band diagrams in accumulation regime for a  $p$ -type oFET, i.e.  $V_{sg} < 0$  V and  $V_{sd} = 0$  V, at STM tip bias (a)  $V_{bias} = 0$  V, (b)  $V_{bias} > 0$  V and (c)  $V_{bias} < 0$  V. Since the tip is (virtually) grounded in the experiment, the tip Fermi level is taken as reference.

## 5. Scanning tunneling microscopy via the accumulation layer of *p*-type organic field effect transistors

For positive sample bias  $V_{bias} > 0$  V, the most probable current pathway is illustrated in Fig. 6b. As shown, electrons tunnel from the tip to the HOMO of pentacene where they recombine with holes coming from the accumulation layer. At negative sample bias  $V_{bias} < 0$  V, see Fig. 6c, electrons tunnel from the HOMO of pentacene to the tip, creating vacant holes in pentacene, which are subsequently transported to the accumulation layer.

To get an idea of the maximum current density that can be used in this type of experiment, we followed the imaging stability versus tunnel current. By increasing the STM current to  $I_{tunnel} = 10$  pA, the ‘topography’ started showing a flat surface, suggesting that the STM tip penetrates the layer. At  $I_{tunnel} = 20$  pA the tip crashed on the SiO<sub>2</sub> dielectric.

### 5.4 Conclusion

Summarizing, we demonstrate the possibility to do STM on operational oFETs in both the linear and the saturation regime. The tunnel current is transported to the source and drain contacts via the accumulation layer. With the condition of high signal-to-noise ratio in the tunnel current, the demonstration of stable STM is an important step towards high resolution scanning tunneling potentiometry.

### 5.5 References and notes

- [1] P. Muralt, and D.W. Pohl, Appl. Phys. Lett. **48**, 514 (1986).
- [2] D.S.H. Charrier, T. de Vries, S.G.J. Mathijssen, E.-J. Geluk, E.C.P. Smits, M. Kemerink, R.A.J. Janssen, Org. Electron. **10**, 994 (2009).
- [3] L. Bürgi, H. Sirringhaus, and R.H. Friend, Appl. Phys. Lett. **80**, 2913 (2002).
- [4] E.C.P. Smits, S.G.J. Mathijssen, M. Cölle, A.J.G. Mank, P.A. Bobbert, P.W.M. Blom, B. de Boer, and D.M. de Leeuw, Phys. Rev. B **76**, 125202 (2007).

- [5] E. Mena-Osteritz, A. Meyer, B.M.W. Langeveld-Voss, R.A.J. Janssen, E.W. Meijer, and P. Bäuerle, *Angew. Chem. Int. Ed.* **39**, 2680 (2000).
- [6] B. Grévin, P. Rannou, R. Payerne, A. Pron, and J.-P. Travers, *Adv. Mater.* **15**, 881 (2003).
- [7] G.R. Dholakia, M. Meyyappan, A. Facchetti, and T.J. Marks, *Nano Lett.* **6**, 2447 (2006).
- [8] A.I. Onipko, K.-F. Berggren, Yu.O. Klymenko, L.I. Malysheva, J.J.W. M. Rosink, L.J. Geerligs, E. van der Drift, and S. Radelaar, *Phys. Rev. B* **61**, 11118 (2000).
- [9] L. Ruppel, A. Birkner, G. Witte, C. Busse, T. Lindner, G. Paasch, and C. Wöll, *J. Appl. Phys.* **102**, 033708 (2007).
- [10] M. Kemerink, S.F. Alvarado, P. Muller, P.M. Koenraad, H.W.M. Salemink, J.H. Wolter, and R.A.J. Janssen, *Phys. Rev. B* **70**, 045202 (2004).
- [11] O.D. Jurchescu, J. Baas, and T.T.M. Palstra, *Appl. Phys. Lett.* **87**, 052102 (2005).

## Chapter 6

# Giant out-of-plane ambient actuation of poly(3,4-ethylenedioxythiophene) : poly(styrenesulfonate) thin films

### 6.1 Introduction

Conjugated polymers offer distinct and advantageous properties as compared to inorganic materials in terms of plasticity, biocompatibility, and low processing cost. Hence, their use in electroactive actuators attracts considerable interest,<sup>1-6</sup> and finds application in artificial muscles,<sup>7,8</sup> microsystems,<sup>9</sup> extendable textiles,<sup>10</sup> and more recently in lab-on-a-chip.<sup>11</sup>

Nowadays, the most widely used  $\pi$ -conjugated polymer in organic actuators is polypyrrole (PPy), combined with dodecylbenzenesulfonate (DBS). This system manifests an in-plane elongation that can be converted into a bending motion on micro or millimetric scales with long lifetimes.<sup>12</sup> The PPy:DBS system uses an additive electrolyte as ionic reservoir, called 'wet' or 'dry' actuator if the reservoir is a liquid<sup>13</sup> or a solid<sup>14</sup> ion source. Under an externally applied voltage, the mobile anions or cations present in the electrolyte can move and create a volume expansion (or contraction) in the polymer by insertion (or de-insertion) of ions. Due to similarities, this expansion is also called osmotic expansion.<sup>15</sup> Additively, changes in bond lengths and conformation in the polymer backbone may also contribute to expansion. In standard organic actuators, the insertion and de-insertion of ions is achieved while maintaining global electroneutrality, therefore the polymer is either oxidized or reduced. Although in-plane actuation is

commonly reported, remarkably few publications reported out-of-plane actuation. Smela *et al.*<sup>16</sup> measured a 1.5  $\mu\text{m}$  thick film of PPy with atomic force microscopy (AFM), showing an out-of-plane actuation of 125% at first cycle and 35% in normal cycle. The experiment was done in a  $\text{Na}^+\text{DBS}^-$ -rich solution.

In the field of organic electronics, the oxidatively doped conjugated polycation poly(3,4-ethylenedioxythiophene) blended with poly(styrenesulfonate) as polyanion (PEDOT:PSS) is ubiquitous and a viable candidate for replacing metallic electrodes in organic field effect transistors,<sup>17,18</sup> organic solar cells,<sup>19</sup> and organic light emitting diodes.<sup>20</sup> Recently, Kiefer *et al.*<sup>21</sup> made a PEDOT bilayer in-plane actuator by electrochemical synthesis and obtained good lifetime performances. They showed a high deflection (1.5 mm) at a polymerization potential of 1.0 V and reasonable stability after 100 cycles. Out-of-plane actuation at ambient conditions of PEDOT:PSS thin films has not been reported to our knowledge.

In this chapter, we present the surprising giant out-of-plane actuation (up to 950% at first cycle and more than 100% for normal cycle) of PEDOT:PSS thin films in air, without using additional ionic electrolytes. The PEDOT:PSS thin films deposited on micropatterned electrodes actuate on the positive electrode upon application of a DC bias with an onset bias around 4 V. Below we outline the experimental observations and a possible mechanism for this remarkable actuation.

## 6.2 Results

### 6.2.1 Out-of-plane actuation at the anode

Thin (65 nm) PEDOT:PSS (1:6 weight ratio) films have been applied onto glass substrates covered with interdigitating gold electrodes (30 nm high, 10  $\mu\text{m}$  wide) at variable spacing  $L$  (1, 4, 10, or 20  $\mu\text{m}$ ). Fig. 1a shows a typical example of the current measured between anode and cathode (for  $L = 10 \mu\text{m}$ ) while 4 V was applied. The current decreases irregularly with time, suggesting that several processes are involved, to reach a

## 6. Giant out-of-plane ambient actuation of poly(3,4-ethylenedioxythiophene) : poly(styrenesulfonate) thin films

steady, but low current after about 450 s. The dotted horizontal line shown in Fig. 1a at 2.4  $\mu\text{A}$  is the Ohmic current at 4 V according to the reported low field lateral conductivity of PEDOT:PSS.<sup>22</sup> The arrows in Fig. 1a indicate characteristic points at different times.

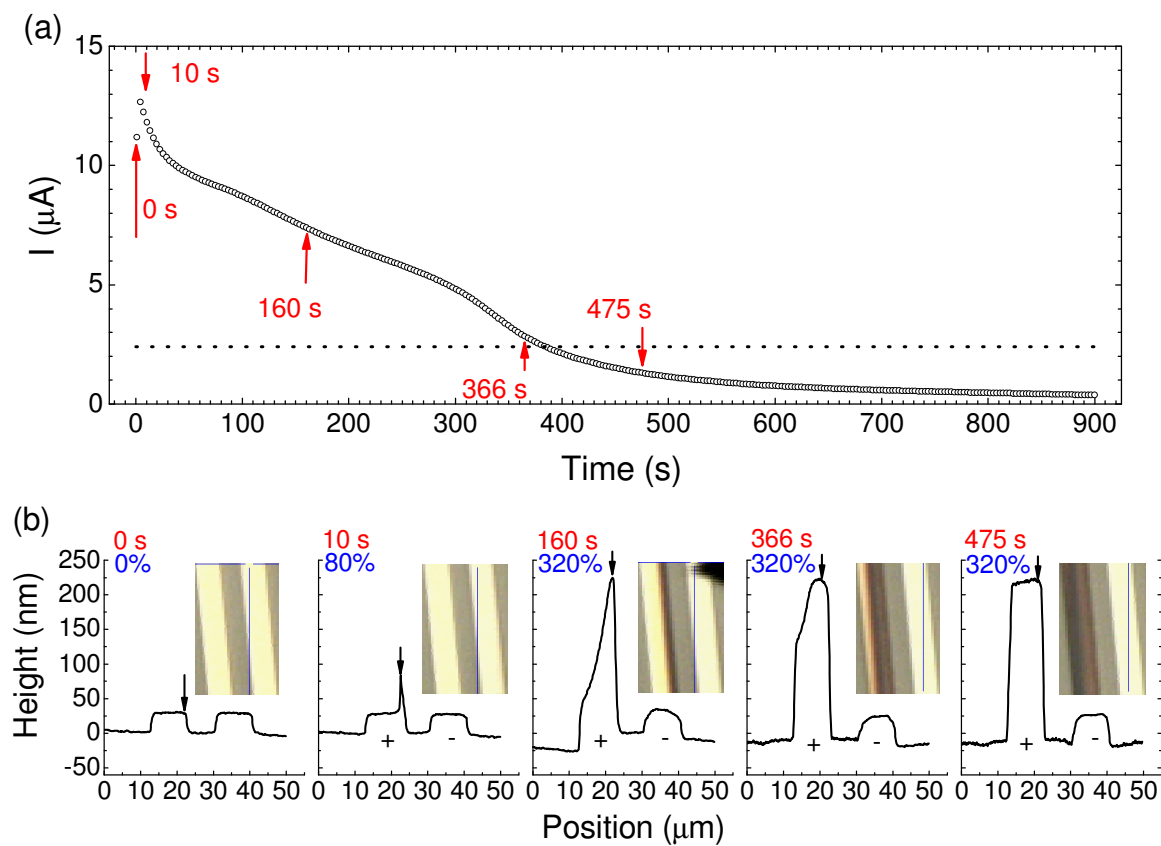


Fig. 1. (a) Current versus time while 4 V was applied between the anode and cathode at 35% relative humidity and with  $W = 1$  mm and  $L = 10$   $\mu\text{m}$ . (b) Topography AFM measurements and optical pictures (insets) at characteristic times in panel (a). Actuation rates are calculated at arrowed locations.

Topography measurements by AFM and optical pictures at these characteristic points are shown in Fig. 1b. At 0 s, the PEDOT:PSS thin film covered the substrate where 30 nm thick gold electrodes were visible in both topography and the optical picture, since the PEDOT:PSS layer is transparent. At 10 s, the anode showed a 80 nm (or 80%<sup>23</sup>)

positive and out-of-plane actuation appearing from the channel side, while the PEDOT:PSS film remained transparent. The total dissipated energy  $E = 480 \mu\text{J}$  after 10 s was estimated from the product of current ( $12 \mu\text{A}$ ), bias (4 V), and time. At 160 s, the actuation extended over the whole anode, the highest point was at 225 nm (or 320%). The optical picture showed a dark front on the anode coinciding with the maximum height. At 366 s, the actuation continued and saturated from the channel side whereas the optical image showed a dark front coinciding with the saturated region. From 475 s onwards, the actuation was saturated and a 230 nm (or 320%) high plateau was formed on the anode and a brownish color appeared. A test sample was made to confirm that a fresh 250 nm thick film of PEDOT:PSS is not brownish but rather transparent light blue. At 0 V bias, the whole anode remained unchanged in color and topography for at least several hours. The stability over time will be discussed in more detail below. The actuation was working in a bias range from 4 V to 10 V. Below 4 V, no out-of-plane actuation on the anode was observed, above 10 V the thin film deteriorated quickly.

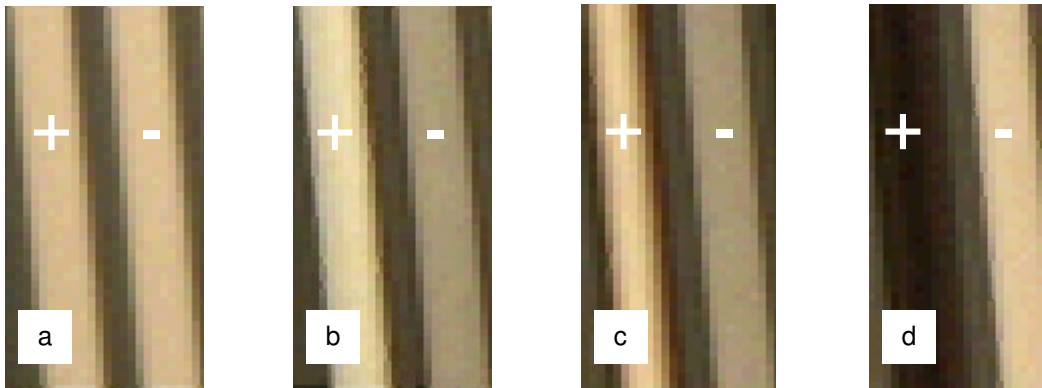


Fig. 2. At low sample illumination, the cathode showed a bluish color for  $t < 100$  s, the anode was actuated at 4 V with  $L = 4 \mu\text{m}$  and  $W = 7 \text{ mm}$ . a), b), c) and d) refer to the times of an applied 4 V bias at  $t = 0, 59, 78,$  and  $197$  s, respectively.

Under low sample illumination, a bluish color could be observed on the cathode for  $t < 100$  s while the anode was actuated at 4 V, as shown in Fig. 2. The bluish color appearing on the cathode indicates that PEDOT is reduced at the cathode.<sup>24,25</sup> In the neutral state PEDOT exhibits a strong absorption in the red part of the spectrum at  $\sim 600$

## 6. Giant out-of-plane ambient actuation of poly(3,4-ethylenedioxythiophene) : poly(styrenesulfonate) thin films

nm and less at lower wavelengths, causing a bluish color. The disappearance of the bluish color at later times suggests that the reduced PEDOT is reacted away for  $t > 100$  s.

### 6.2.2 Depletion and morphology changes in the channel

In section 2.1, the height of accumulated material on the anode was measured taking the channel as a baseline.<sup>23</sup> To access the absolute actuation height, a measurement of material depletion in the channel is necessary. The microstructure design allowed us to measure, in a single AFM measurement, the topography over areas with and without electric field. The left picture of Fig. 3 is a  $50\ \mu\text{m} \times 50\ \mu\text{m}$  AFM image scanning two (left and right) actuated anodes and one (middle) cathode. Upon applying a bias over anode and cathode an electric field will only be present where the two electrodes are interdigitating, i.e. the lower part of the image, while in the upper part the field is absent. The top left inset represents an optical picture at the same scanning area, showing the electrodes and the (brown) material that has accumulated on the anodes next to the anode. Measurement positions  $z_1$  and  $z_2$  were placed in areas without electric field and with electric field, respectively.  $z_1$  was assumed to have an unchanged height and thickness. The line-section through  $z_1$  and  $z_2$  is plotted in the inset and is a proof of height diminution in the channel. The height difference between  $z_1$  and  $z_2$  is a direct reading of the depletion of material and is around 65 nm in the case of Fig. 3. For very thin films, i.e. for 21 and 26 nm, the depletion measurements were not very accurate.

Besides AFM, also STM measurements were performed to look at the PEDOT:PSS morphology. The tunneling current was flowing from the Pt/Ir tip to one electrode via the PEDOT:PSS layer. PEDOT:PSS thin films have a sufficiently high lateral conductivity<sup>22</sup> to allow for STM in the channel, despite the absence of a conductive substrate. On the top right of Fig. 3, the  $400\ \text{nm} \times 400\ \text{nm}$  STM picture of a pristine device (taken around point  $z_1$ , see above) shows pancake-shaped domains, as reported previously.<sup>22</sup> These domains are the PEDOT:PSS clusters having a PEDOT-rich and quasi-metallic core and a PSS-rich insulating or weakly conductive shell.<sup>22</sup> The STM picture on the bottom right of Fig. 3 was measured between the electrodes at  $z_2$ , after having applied the 4 V bias. The electric field orientation is indicated with the white

arrow. The STM pictures show that the surface morphology in the channel changed from pancake shaped clusters to fibrous shapes in going from a pristine to a fully actuated device. The fibrous orientation coincides with the electric field direction. Moreover, the STM pictures show a major field induced surface change, indicating mass transport supported by the height reduction seen by AFM. Moreover, the bias needed for STM measurements on actuated material was 3 times higher than for pristine material. By measuring the  $I$ - $V$  curves before and after actuation, we observed a decrease in film conductance by one order of magnitude. This observation is consistent with the depletion measurements, i.e. less material present in the channel will lead to a layer with a lower conductance. The conductivity of the remaining material could not be accurately determined because of a large (relative) uncertainty in the final layer thickness.

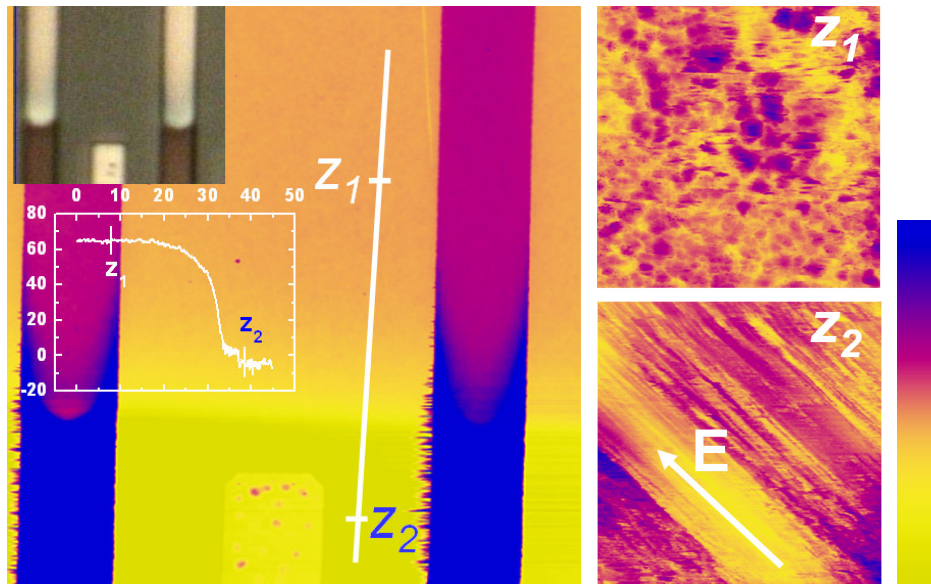


Fig. 3: Left picture:  $50 \mu\text{m} \times 50 \mu\text{m}$  AFM picture ( $z_{\text{scale}} = 150 \text{ nm}$ ) scanning two (left and right) actuated anodes and one (middle) cathode. A 4 V bias was applied during 30 min. Top left inset: optical picture of the same area.  $z_1$  and  $z_2$  are placed in areas without and with electric field, respectively. A cross-section on the line through  $z_1$  and  $z_2$  is plotted in the inset with vertical axis in nm and horizontal axis in  $\mu\text{m}$ . On the right:  $400 \text{ nm} \times 400 \text{ nm}$  STM pictures ( $z_{\text{scale}} = 30 \text{ nm}$ ) were measured at  $z_1$  and  $z_2$ .  $z_1$  ( $z_2$ ) was taken with the following parameters: sample bias 0.5 V (1.5 V), setpoint current 500 fA (100 fA).

## 6. Giant out-of-plane ambient actuation of poly(3,4-ethylenedioxythiophene) : poly(styrenesulfonate) thin films

### 6.2.3 Lack of volume conservation

The AFM measurements in Fig. 1b show that the final height of the anode after actuation equals 230 nm. On first sight, this might be a summation of depleted material from channel (65 nm) and cathode (65 nm) plus material already present on the anode (65 nm) plus the electrode thickness (30 nm), i.e.  $230 \approx 225 = 65 + 65 + 65 + 30$ . Recall that height is measured with respect to the surrounding channel, so the calculated 225 nm is an upper limit under the assumption that both channel and cathode are fully depleted. For  $L = 10 \mu\text{m}$  no further geometrical corrections are needed since channel and electrode have the same width. The difference  $230 - 225 = 5 \text{ nm}$  is small in this case.

Surprisingly, however, the maximum attainable height on the anode proved to be virtually independent of both channel length  $L$  and initial film thickness  $d$ , as shown in Fig. 4. We attribute the non-systematic, minor variation between layers of different thickness to differences in ambient humidity while measuring different samples. On a very wide anode (not shown) the actuation stopped after certain length because the channel was depleted and the reaction that started at the anode edge stopped. A very wide cathode (not shown) did not change the maximum actuation height on the anode, suggesting that the amount of material per unit length determines the final height.

This independence of  $d$  translates into giant actuation rates for very thin films, e.g. 950% for a 21 nm film. For these thinner films, the difference between anodic height increase and available material (in channel and cathode regions) can be as high as 150 nm. From this result we conclude that a significant part of the height increase on the anode is not due to a rearrangement of material but due to a volume increase of the available material.

PEDOT:PSS films with a weight ratio 1:20 (instead of the 1:6 used above) and with thicknesses of 42, 94, and 160 nm, respectively gave maximum actuation heights at 245 nm, 238 nm and 220 nm. Error bars were 5 nm for each value. Like for the 1:6 PEDOT:PSS, the maximally attainable actuation height seems mostly independent of film

thickness. Also the absolute numbers are within experimental accuracy the same for 1:6 and 1:20. Hence, the results suggest that the actuation rate is also independent of the PEDOT:PSS composition. Films with a weight ratio of 1:1 did not show any actuation which we attribute to the much higher viscosity of this material.

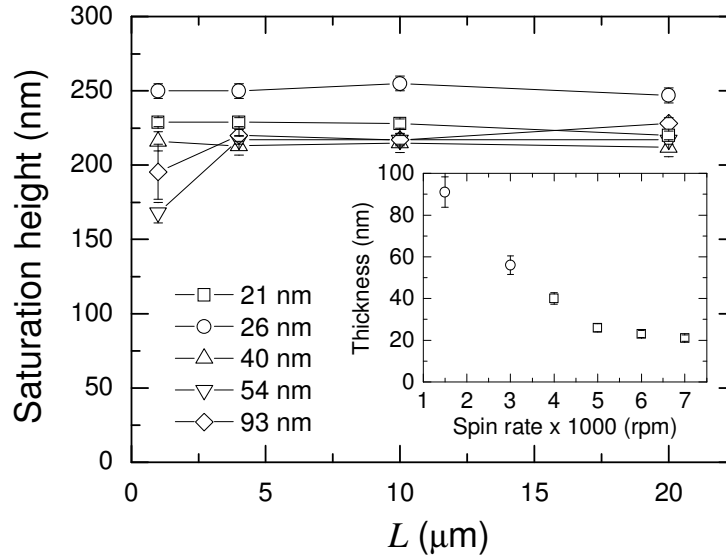


Fig. 4: Maximum attainable actuation (saturation) on the anode is measured versus  $L$  for different film thicknesses  $d$ , see legend. The inset shows the film thicknesses versus the spin rate of deposition. Open squares are obtained from a diluted solution.

#### 6.2.4 Reversibility of the actuation

Because the observed actuation is in part due to transport of material from the channel and the cathode to the anode and in part due to a volume increase of the material at the anode, the reversibility of the processes is an interesting question.

Reversibility experiments were performed in a quantitative way; we used new devices under identical conditions (i.e. same batch,  $L$ ,  $W$ , and relative humidity) as those shown in Fig. 1. The 10 s actuation showed a reasonably reversible actuator with at least 10 full cycles, as shown in Fig. 5a. The average forward actuation speed was 3 nm/s whereas the reversed process was faster at  $-57$  nm/s. Under 0 V bias, the actuation remained stable in time ranges of tenths of seconds. The noisy AFM signal was mainly

## 6. Giant out-of-plane ambient actuation of poly(3,4-ethylenedioxythiophene) : poly(styrenesulfonate) thin films

due to the fast changing of topography although also some topographical spots appeared on the electrodes for higher cycle numbers.

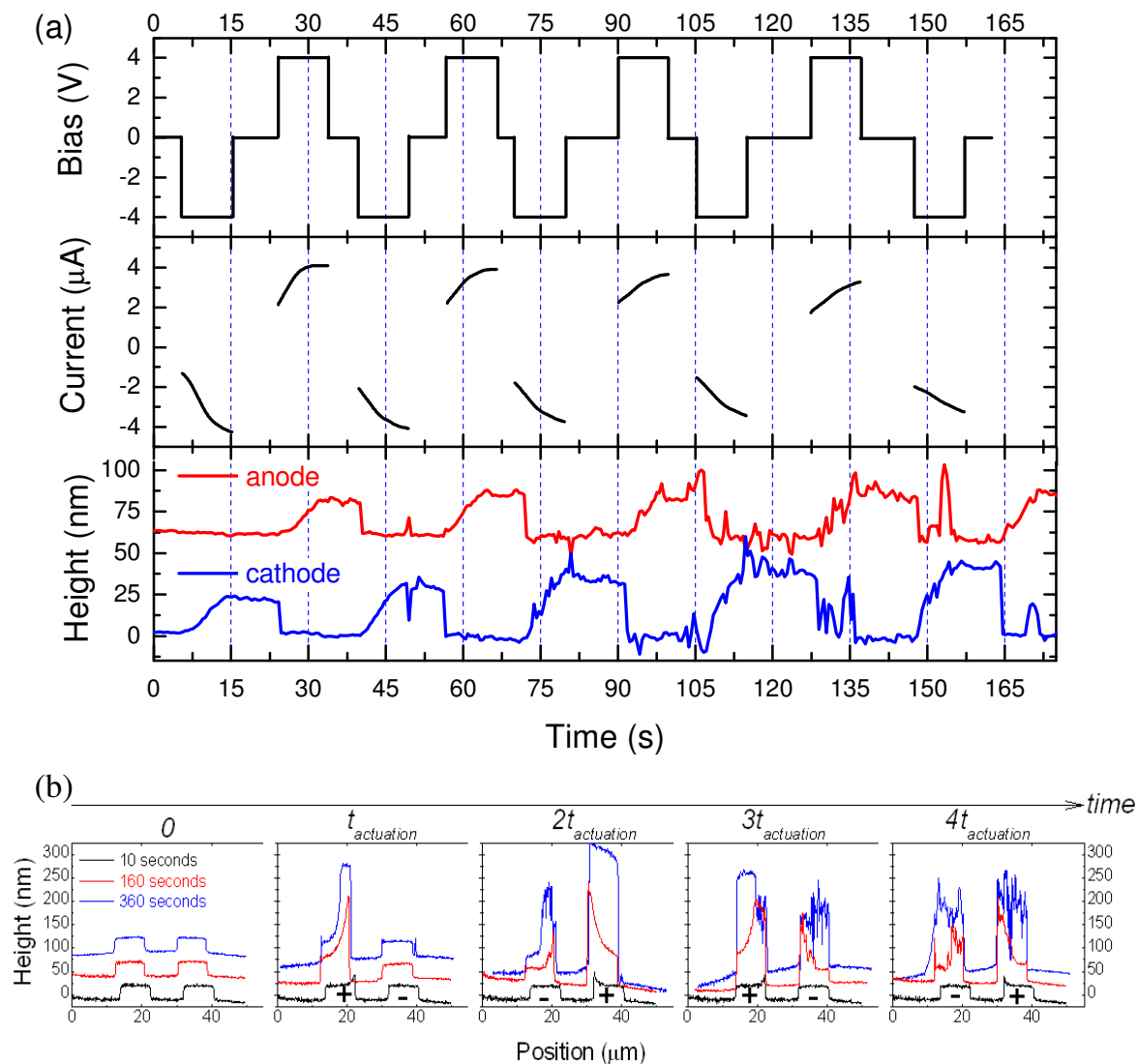


Fig. 5: (a). A cyclic bias between +4 and -4 V was applied while the current and height above the electrodes were simultaneously measured versus time. At 10 s applied bias, the actuation is fully reversible after 5 cycles. (b) Topographic sections for three actuation times 10, 160, and 366 s. For clarity, the topographies are vertically shifted 25 nm from each other. The top horizontal axis shows the actuation times according to the legend. Sign of bias is indicated.

The graphs in Fig. 5b show the effects of reversing the actuating bias for three actuation times, 10 (black), 160 (red) and 366 s (blue). Clearly, reversibility is reduced with increasing actuation time, the 10 s being fully reversible, the 160 s partially, and the 366 s only marginally. We remark that the hardly reversible part is accompanied by a brownish color on the anode, as visible in Fig. 1b. This suggests that the reversible and irreversible processes are related to different processes, giving rise to different changes in the optical absorption. Recall also the bluish color on the cathode during the reversible actuation as discussed above.

### 6.2.5 Role of humidity in actuation and stability

To investigate the possibility that the volume increase of material is associated with the uptake of water from the ambient, actuation was tested under different environmental conditions. We established that actuation was not observed in a dry N<sub>2</sub> atmosphere and hardly observed in an ambient of reduced (13%) relative humidity.

To further assess the role of water, annealing experiments using a hot plate on *already* actuated (in air) devices were performed in air and in dry N<sub>2</sub> atmosphere. In a first experiment an actuated device was heated in air at 130 °C for 2 min. Representative height profiles before (label A) and after (label B) are shown in Fig. 6a. The height significantly dropped by 132 nm, i.e. from 201 nm to 69 nm, and a turquoise color appeared on the anode instead of the original brown. Note that the original height of the anode prior to actuation was 30 nm, whereas the height after actuation and subsequent annealing was ca. 69 nm. Hence height gain of actuation is only partly undone by the annealing.

A second experiment was to measure an air-actuated device that was transported to and then left in a glove box filled with dry N<sub>2</sub> for 5 days (Fig. 6b A (before) to B (after)). The height dropped by 115 nm, from 205 nm to 90 nm. A last heating step at 130 °C for 2 min. (label C) did not further change the height.

**6. Giant out-of-plane ambient actuation of poly(3,4-ethylenedioxythiophene) : poly(styrenesulfonate) thin films**

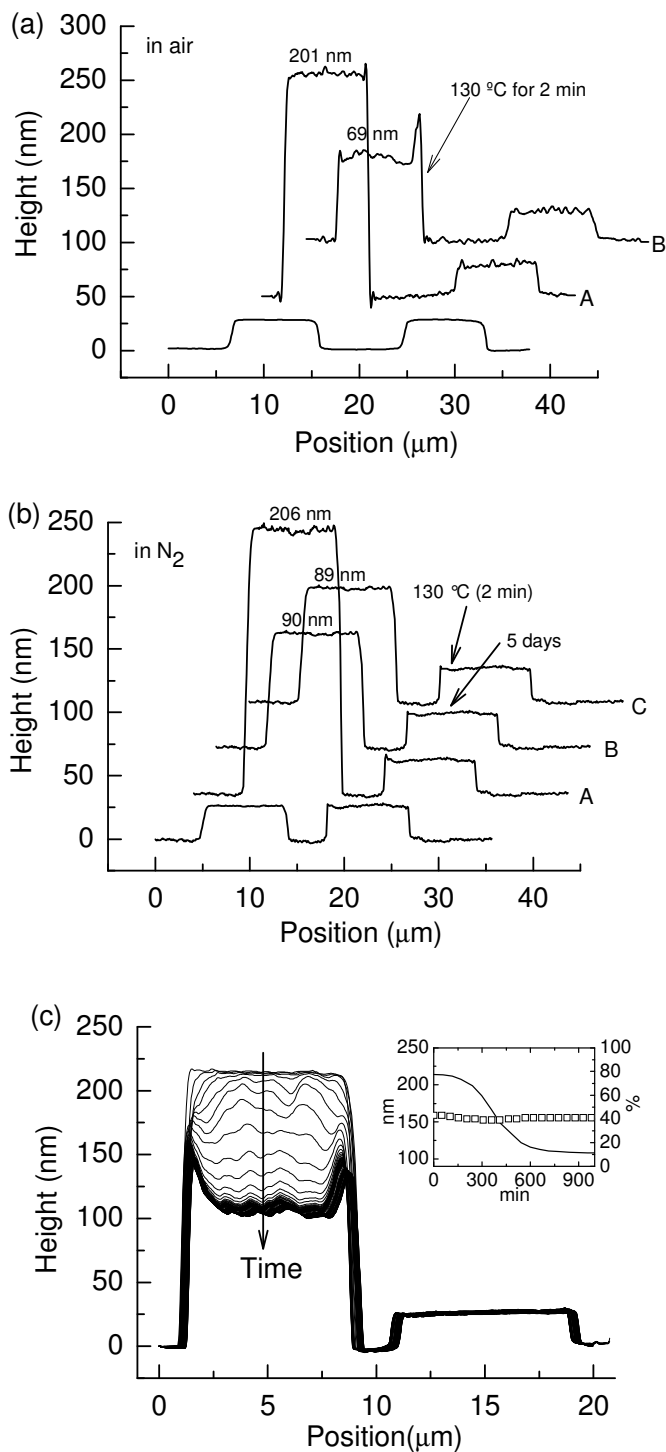


Fig. 6: Annealing experiments in air (a) and in  $\text{N}_2$  (b) of devices previously actuated in air. The relaxation of the actuation or is shown in panel (c). Curves were recorded every 60 min during 4 days. The inset shows the height in nm (continuous curve) in the middle of the anode and the relative humidity in % (open squares) versus time.

The absence of actuation in dry environments already indicates that ambient water is involved in the actuation, either directly by enabling electrochemical reactions, or indirectly by acting as a plasticizer for PEDOT:PSS. The very similar effects of slow and forced drying, i.e. a height reduction on the actuated anode while the cathode remains unchanged, suggest that a significant fraction (~60%) of the gained height is due to hygroscopic effects, i.e. absorbed water. The material remaining on the anode after evaporation of excess water has likely been transported from the channel and cathode, as discussed under in section 2.2 above.

Another experiment was the continuous height measurement under ambient conditions during 4 days (Fig. 6c). The inset shows the height (continuous curve) in the middle of the anode versus time, empty squares are the ambient relative humidity recorded simultaneously. In addition to a drop by 100 nm of the actuated height over 4 days, a color change from brownish to turquoise was observed.

### 6.2.6 Surface potential measurements

Scanning Kelvin probe microscopy measurements (SKPM) were performed on different samples. Typical results for a device with film thickness of 21 nm are shown in Fig. 7 (black). Fig. 7a shows the simultaneously measured topography and surface potential averaged over the anode (continuous line) and cathode (dotted line) versus time.

In regions 1 and 2, a 4 V bias is applied, while in regions 0 and 3 both electrodes are grounded. Surprisingly, the surface potential of both electrodes is roughly equal ( $V_{\text{anode}} - V_{\text{cathode}} \approx 0.4$  V) despite a bias voltage of 4 V between them (region 1 in Fig. 7a). Once saturation is reached (at  $t = 413$  s, region 2) a relatively sudden drop of both surface potentials is observed. 65 nm and 91 nm (red) thick films exhibited similar surface potential behavior, though with a significantly smaller difference of surface potentials between the electrodes ( $V_{\text{anode}} - V_{\text{cathode}} \approx 0.2$  V) in region 1, i.e. during actuation.

## 6. Giant out-of-plane ambient actuation of poly(3,4-ethylenedioxythiophene) : poly(styrenesulfonate) thin films

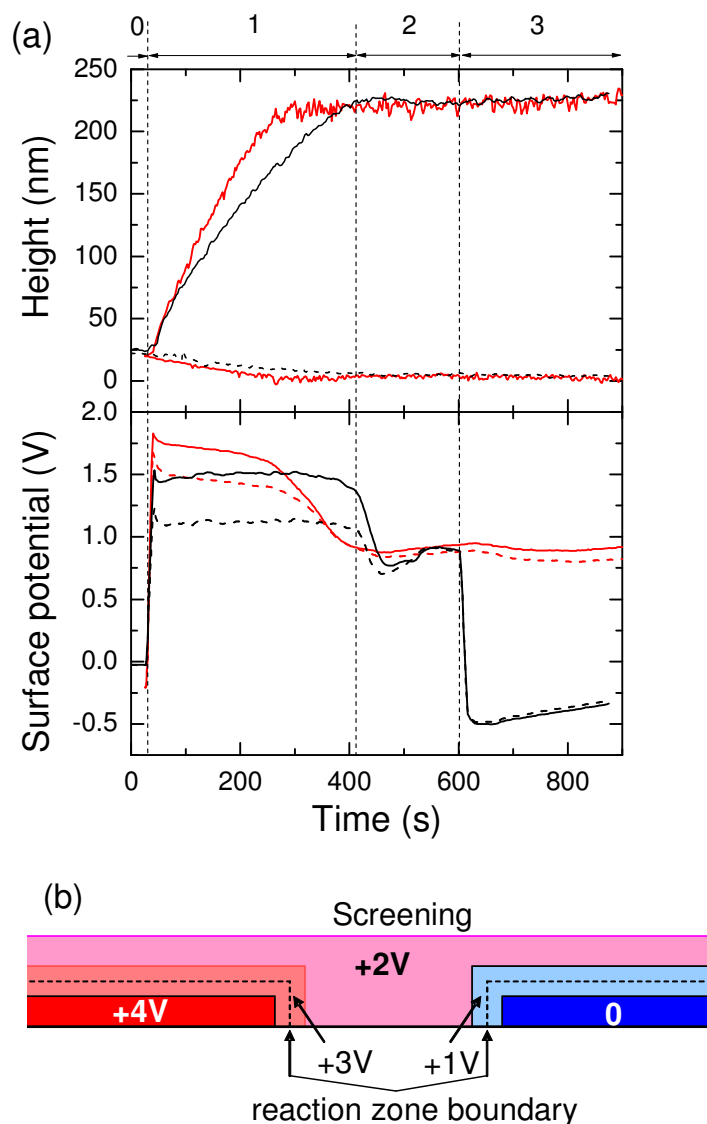
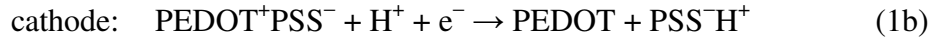
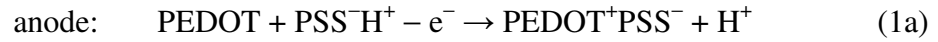


Fig. 7: (a) A 21 nm PEDOT:PSS film was measured at 59% relative humidity with SKPM at 0 nm lift height (black lines). In regions 1 and 2, a 4 V bias was applied, while in regions 0 and 3 both electrodes were grounded. SKPM and topography measurements are shown versus time simultaneously on anode (solid line) and cathode (dashed line). For comparison a 90 nm PEDOT:PSS film (red lines) was measured under the same conditions. (b) Schematic drawing of the potential inside the PEDOT:PSS film with anode and cathode at 4 V and 0 V, respectively. The potential drops in the light colored regions.

The fact that only a fraction of the applied bias is visible in the surface potential is attributed to (partial) electrostatic screening by mobile ions present in the PEDOT:PSS, as illustrated in the cartoon in Fig. 7b. The smaller difference between anodic and cathodic surface potentials for thicker (65 nm and 91 nm) films strongly suggests that the screening length is of the order of a few tens of nm. We note that Taylor *et al.*<sup>26</sup> reported similar electrostatic screening in PEDOT:PSS, though on longer channels.

### 6.3 Discussion

From the observations above, it is clear that at least two different mechanisms are relevant; one reversible reaction causing a blue color on the cathode preceding one or more irreversible reactions causing the occurrence of dark colors on the anode. For the reversible reactions we propose the following electrochemical redox reactions:



where PEDOT<sup>(+)</sup>, PSS<sup>(-)</sup> and H<sup>+</sup> are respectively a neutral (oxidized) PEDOT repeat unit, the neutral (reduced) PSS repeat unit, and the proton. Starting from a neutral film as drawn in Fig. 8a and under high enough bias, PEDOT:PSS will further oxidize at the anode, causing remaining neutral PEDOT repeat units to form PEDOT<sup>+</sup>PSS<sup>-</sup> in a higher oxidation state and an excess of H<sup>+</sup>. In the electric field between anode and cathode, the excess charge formed on the anode can be most easily transferred to the cathode via transport of the excess proton through the PEDOT:PSS layer. The excess of PSSH in the 1:6 wt. ratio PEDOT:PSS mediates the transport of the small H<sup>+</sup> ion. Due to their much larger size, the ion mobilities of PEDOT<sup>+</sup> to the cathode or PSS<sup>-</sup> to the anode will be less. Under ambient conditions, the hygroscopic PEDOT:PSS film contains a significant amount (~25%) of water, which facilitates H<sup>+</sup> transport.<sup>27</sup> In section 6.2.5 we showed that dry conditions indeed prevent the actuation effect.

## 6. Giant out-of-plane ambient actuation of poly(3,4-ethylenedioxythiophene) : poly(styrenesulfonate) thin films

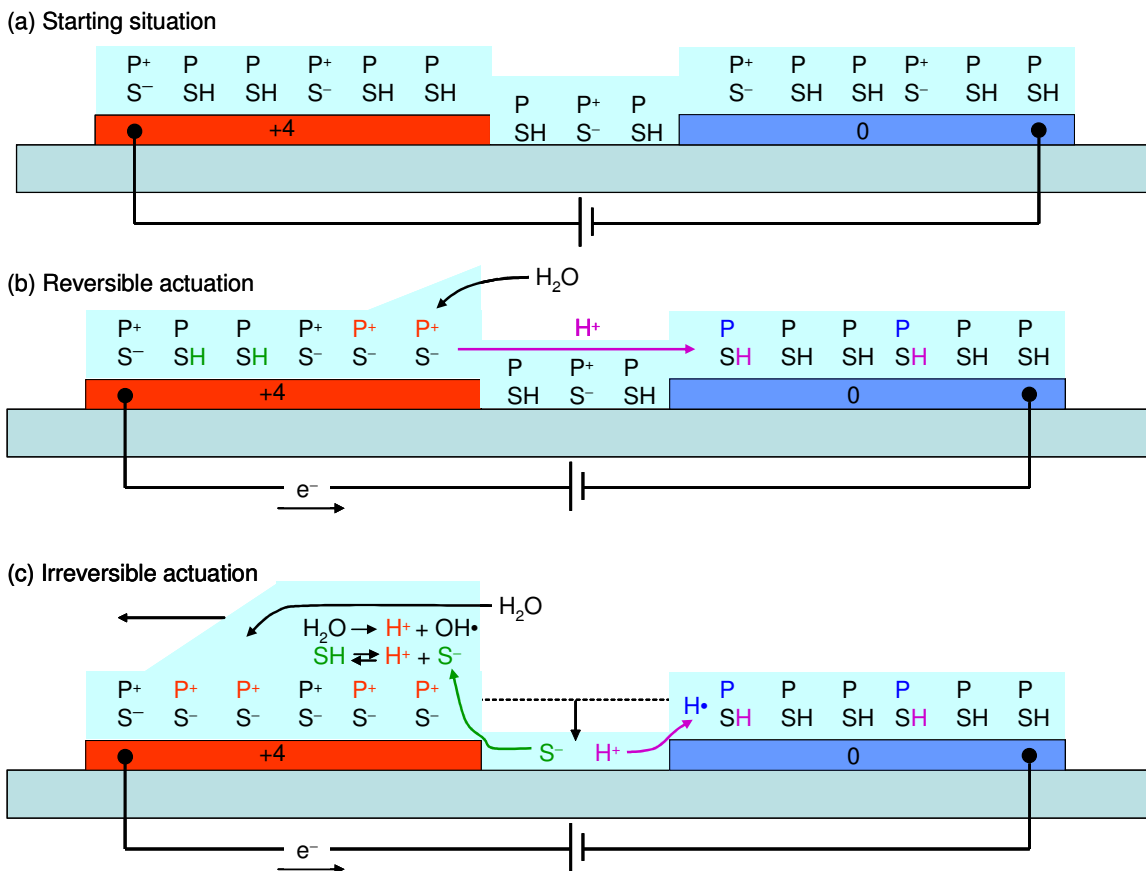
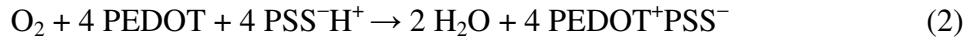


Fig. 8: Schematic drawings of starting situation (a), reversible (b), and irreversible (c) actuations. Repeating units of PEDOT<sup>(+)</sup> and PSS<sup>(-)</sup> are represented by P<sup>(+)</sup> and S<sup>(-)</sup>. (a) The starting situation reflects that in pristine PEDOT:PSS about 1 in 3 PEDOT monomer units is oxidized and electrostatically bound to PSS<sup>-</sup>. (b) During reversible actuation P units are oxidized at the anode (red) and P<sup>+</sup> units reduced at the cathode (blue), accompanied by H<sup>+</sup> transport (form left to right). This reaction will become limited by the availability of P (or P<sup>+</sup>) at the electrodes and the imbalance in H<sup>+</sup> concentration. (c) Irreversible actuation will occur and new oxidation and reduction reactions, likely involving water and protons, will take place, while remaining ions in the channel will PSS<sup>-</sup> will move. During the entire actuation (b and c), water is absorbed from the ambient, causing the actuation not to be limited by the amount of starting material in the channel.

Reaction (1b) is the electrochemical reduction of PEDOT<sup>+</sup>, the reverse of (1a), and proposed to occur at the cathode. The proton is supplied by the anodic reaction and forms PSSH with PSS<sup>-</sup>, while PEDOT<sup>+</sup> is (partially) reduced to PEDOT. The observation of a bluish color on the cathode confirms this reduction step for times  $t < 100$  s. For longer times, the working conditions enable the oxidation of PEDOT by oxygen from the air:



which suppresses the bluish color on the cathode for times  $t > 100$  s.

Having established possible redox reactions, we will now discuss the actuation mechanism. The actuation on the anode may be caused by (a) a mass transport of anions coming from the cathode, (b) conformational changes, or (c) osmosis, i.e. uptake of H<sub>2</sub>O from ambient air or other parts of the film. An alternative to the three mentioned reasons for explaining the apparent volume expansion is gas formation due to electrolysis of water. As demonstrated by de Brito *et al.*<sup>28</sup> a PEDOT:PSS layer sandwiched by crossed Au electrodes can be used as (irreversible) fuse due to the trapping of gas between the electrodes. However, in the present case, gas formation is not consistent with the observed reversibility of actuation, gas formation being irreversible.

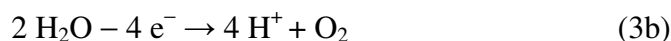
The proposed redox reactions (1a) and (1b) do not involve anionic species to transport from the cathode toward the anode. Apart from PEDOT<sup>+</sup>, PSS<sup>-</sup>, and H<sup>+</sup>, the most abundant ionic species in PEDOT:PSS is Na<sup>+</sup> (300 ppm). Lowering the Na<sup>+</sup> concentration by a factor 10 to 30 ppm did not lead to appreciable changes in actuation. Doping of polymer chains is known to induce conformational changes. X-ray measurements on highly oriented polyacetylene showed a chain length elongation (or contraction) upon Li<sup>+</sup>, K<sup>+</sup> donor (or Γ<sup>-</sup> acceptor) doping.<sup>29</sup> However, the reported effects are typically small as compared to the height changes observed here. Hence, in our view neither mass transport (small protons) nor conformational changes can explain the actuation on the anode. Therefore, we suggest the osmotic mechanism to explain the actuation and, simultaneously, the apparent lack of volume conservation. Reaction (1a) leads to an increased positive doping of PEDOT<sup>+</sup> chains at the anode, causing the further

## 6. Giant out-of-plane ambient actuation of poly(3,4-ethylenedioxythiophene) : poly(styrenesulfonate) thin films

uptake of ambient H<sub>2</sub>O. Alternatively, other parts of the thin film may act as source for H<sub>2</sub>O. The assignment of H<sub>2</sub>O uptake on the anode as the main cause of volume increase is in full agreement with the observations in described in section 6.2.5.

By changing the bias polarity, reactions (1) swap electrode, and the PEDOT<sup>+</sup> concentration on the ‘new’ anode increases at the cost of the concentration on the ‘old’ anode. Hence, an osmotic driving force for H<sub>2</sub>O transport from the old to the new anode develops, making the actuation reversible. A schematic drawing of the reversible process is shown in Fig. 8b.

Several mechanisms can be proposed as for why reactions (1a) and (1b) stop and irreversible reactions start. E.g. when all PEDOT becomes fully neutralized at the cathode or fully oxidized at the anode, reactions (1b) and (1a) will terminate. The former option seems less likely because air oxidation (2) enables a ‘recycling’ of neutralized PEDOT under ambient conditions at the cathode. Both options, however, also seem unlikely considering that the integrated current during the reversible regime is insufficient to convert all available PEDOT on the anode or PEDOT<sup>+</sup> on the cathode. More likely, reactions (1a) and (1b) stop because of a pH imbalance developing between the two electrodes. At that point other redox reactions can take over that can restore the pH balance and are within the electrochemical window, e.g.



where reactions (3a) and (3c) are equivalent to (3b) and (3d) but do not require the overpotentials usually associated with the formation of gaseous oxygen or hydrogen. To maintain charge neutrality above the electrodes, we propose the migration of PSS<sup>-</sup> to the anode and migration of protons to the cathode. The observations described in section 6.2.2 are consistent with transport of PSS<sup>-</sup>. Once PSS<sup>-</sup> has left the cathode it leaves behind a vacant H<sup>+</sup>, which will likely be reduced to form H<sup>·</sup> radicals that will react further, making the process described by (3a) and (3c) irreversible. A schematic drawing

is shown in Fig. 8c. In this regime, the actuation is a combination of the reactions (1a) and (3a) implying mass (PSS) transport and osmosis (uptake from water). The observations in section 6.2.2 clearly showed a depleted channel after reaching the maximum attainable actuation, showing that also the channel may act as  $\text{PSS}^-$  source. They also showed a morphology change in the channel attributed to transport of PSS to the anode. The thermal and temporal experiments in section 6.2.5 showed a partial height reduction reflecting the  $\text{H}_2\text{O}$  component; the remaining material on the anode is therefore attributed to PSS. The dark and turquoise colors are tentatively explained by the irreversible chemical reactions of water or formed hydroxyl radicals at the anode to highly oxidized PEDOT segments.

The picture sketched above rationalizes most observations. However, the independence of the maximally attainable actuation height on channel width and film thickness and on PEDOT:PSS ratio (section 6.2.3) remain to be explained. The answer to these, at first sight surprising independencies comes from the SKPM experiments discussed in section 6.2.6. From the thickness dependence of the potential screening we concluded that the screening length is of the order of tens of nm. Consequently, only a very thin (tens of nm) region is at sufficiently large voltage with respect to the rest of the sample to enable electrochemical reactions, see Fig. 7b. Hence, only the reactive material on the anode within the screening length can react. In other words, the screening length rather than the film thickness determines the actuation height. A similar reasoning explains the channel length independence: as long as the amount of material within the screening length is the limiting factor, the final actuation height is independent of  $L$ . Only for short channels the combined amount of material in the channel and on the cathode may become limiting, as seems to happen in a few instances in Fig. 4. The PEDOT:PSS ratio independence might be explained by a consideration about the most likely screening species being protons. Since PSS is present in similar absolute concentrations in 1:20 and 1:6 PEDOT:PSS material, and is the main proton source, both compositions will have similar screening lengths. Since the amount of PEDOT within the screening length is lower for 1:20, one might expect less actuation for 1:20. However, other effects like viscosity, as is the case for 1:1, will play a role as well.

## 6. Giant out-of-plane ambient actuation of poly(3,4-ethylenedioxythiophene) : poly(styrenesulfonate) thin films

### 6.4 Conclusion

In conclusion, we have found an unexpected out-of-plane actuation of PEDOT:PSS thin films under ambient conditions. The maximum attainable actuation was found to be independent of film thickness and composition and leads to a maximum actuation at first cycle of 950% for a 21 nm thick film. On basis of a wide range of experimental observations, we propose a qualitative electrochemical model. The latter assumes a reversible regime in which proton transport is dominant, and an irreversible regime in which  $\text{PSS}^-$  transport dominates. In both regimes osmotic water adsorption is responsible for a large fraction of the volume expansion.

### 6.5 Experimental

In total, 20 substrates, each containing 62 microstructured pairs of interdigitated electrodes were made. Both anode (positive) and cathode (negative) were 10  $\mu\text{m}$  wide, the distance  $L$  separating the electrodes was 1, 4, 10 or 20  $\mu\text{m}$ , whereas the channel width  $W$  was 1, 7 or 19  $\mu\text{m}$ . Glass substrates and Si/SiO<sub>2</sub> wafers did not show different results. The samples were manufactured using standard UV photolithography. Starting from chemically cleaned substrates, 5 nm of Ti as adhesion layer and 25 nm of Au were subsequently deposited on the developed photoresist by electron beam evaporation under high vacuum conditions. A classical lift-off with acetone was done to remove the resist and to reveal the microstructures.

In our experiments, PEDOT:PSS with a weight ratio 1:6 was purchased from H. C. Starck (Baytron P VP Al 4083, recently renamed Clevios® P Jet (OLED)). The Na<sup>+</sup> concentration was 300 ppm. Alternatively, a 1:6 PEDOT:PSS suspension with a 30 ppm Na<sup>+</sup> concentration was tried and did not exhibit differences in terms of actuation behavior. Prior to spin coating, 2 mL of PEDOT:PSS was taken in a syringe and filtered through a 5  $\mu\text{m}$  porous material (Schleicher & Schue, FP 30/5,0 CN-S). Film thickness

was varied by adjusting the spin rate and dilution as shown in the inset of Fig. 4. The samples were annealed at 200 °C for 2 minutes in order to reduce water content and create a compact layer. Film thicknesses were measured with a profilometer or an AFM. The measured thicknesses varied 5 nm depending on the sample location. Other PEDOT:PSS compositions 1:x were used with  $x = 1$  and  $x = 20$ . The high viscosity of  $x = 1$  did not allow filtering through porous material. For  $x = 1$  no actuation was observed. Between fabrication and measurement the samples were stored in a vacuum glass container ( $10^{-2}$  mbar) or in a N<sub>2</sub>-filled glove box.

The AFM (and scanning Kelvin probe microscope - SKPM) was performed with a Veeco Dimension 3100. Free software (Super Screen Recorder, version 2.0) was used to capture optical images from the built-in camera as video file. We used Nanosensors tips (PPP-NCHR-50, 330 kHz resonance frequency and  $\sim 42$  N m<sup>-1</sup> spring constant) for AFM and Pt-coated Olympus tips (OMCL-AC240TM-B2, 70 kHz resonance frequency and  $\sim 2$  N/m spring constant) for SKPM. The Scanning Tunneling Microscope (STM) was a Veeco Multimode equipped with a low current pre-amp. The STM tips were cut from Pt/Ir wire.

Current-voltage characteristics were measured using a Keithley 4200 parameter analyzer, which was also used to provide biases and measure currents during scanning probe experiments.

## 6.6 References and notes

- [1] T. F. Otero, J. Mater. Chem. **19**, 681 (2009).
- [2] E. Smela, MRS Bulletin **33**,197 (2008).
- [3] G. M. Spinks, E. Smela, in *Handbook of Conducting Polymers*, 3rd Edition, Vol 2 (Eds: T.A. Skotheim, J.R. Reynolds), (CRC Press LLC, Boca Raton, Florida, **2007**, Ch. 14).
- [4] E. Smela, Adv. Mater. **15**, 481 (2003).

## 6. Giant out-of-plane ambient actuation of poly(3,4-ethylenedioxythiophene) : poly(styrenesulfonate) thin films

- [5] C. Immerstrand, K. Holmgren-Peterson, K.-E. Magnusson, E. Jager, M. Krogh, M. Skoglund, A. Selbing, and O. Inganäs, *MRS Bulletin* **27**, 461 (2002).
- [6] R.H. Baughman, *Synth. Met.* **78**, 339 (1996).
- [7] T.F. Otero, and J.M. Sansiñena, *Adv. Mater.* **10**, 491 (1998).
- [8] L. Bay, K. West, P. Sommer-Larsen, S. Skaarup, and M. Benslimane, *Adv. Mater.* **15**, 310 (2003).
- [9] E.W.H. Jager, O. Inganäs, and I. Lundström, *Science* **288**, 2335 (2000).
- [10] F. Carpi, and D. De Rossi, *IEEE Transactions on Information Technology in Biomedicine* **9**, 295 (2005).
- [11] S.B. Prakash, M. Urdaneta, M. Christophersen, E. Smela, and P. Abshire, *Sens. Actuators B Chem.* **129**, 699 (2008).
- [12] J. Ding, D. Zhou, G. Spinks, G. Wallace, S. Forsyth, M. Forsyth, and D. MacFarlane, *Chem. Mater.* **15**, 2392 (2003).
- [13] W. Lu, A.G. Fadeev, B.H. Qi, E. Smela, B.R. Mattes, J. Ding, G.M. Spinks, J. Mazurkiewicz, D.Z. Zhou, G.G. Wallace, D.R. MacFarlane, S.A. Forsyth, and M. Forsyth, *Science* **297**, 983 (2002).
- [14] K. Kaneto, M. Kaneko, Y. Min, and A.G. MacDiarmid, *Synth. Met.* **71**, 2211 (1995).
- [15] L. Bay, T. Jacobsen, S. Skaarup, and K. West, *J. Phys. Chem. B* **105**, 8492 (2001).
- [16] E. Smela, and N. Gadegaard, *Adv. Mater.* **11**, 953 (1999).
- [17] H. Rost, J. Ficker, J.S. Alonso, L. Leenders, and I. McCulloch, *Synth. Met.* **145**, 83 (2004).
- [18] H.J. Snaith, H. Kenrick, M. Chiesa, and R.H. Friend, *Polymer* **46**, 2573 (2005).
- [19] S.-I. Na, S.-S. Kim, J. Jo, and D.-Y. Kim, *Adv. Mater.* **20**, 4061 (2008).
- [20] P.A. Levermore, R. Jin, X. Wang, L. Chen, D.D.C. Bradley, and J.C. de Mello, *J. Mater. Chem.* **18**, 4414 (2008).
- [21] R. Kiefer, D.G. Weis, J. Travas-Sejdic, G. Urban, and J. Heinze, *Sens. Actuators B Chem.* **123**, 379 (2007).
- [22] A.M. Nardes, M. Kemerink, R.A.J. Janssen, J.A.M. Bastiaansen, N.M.M. Kiggen, B. M.W. Langeveld, A.J.J.M. van Breemen, and M.M. de Kok, *Adv. Mater.* **19**, 1196 (2007).

[23] Due to the absence of absolute baseline, the baseline was defined on the PEDOT:PSS surface around the positive electrode where the material was assumed not to completely deplete. This assumption enabled us to estimate the actuation rates  $RA$  (%). They were calculated as  $RA=(A-T)/I$  where  $A$  is the apparent actuation height between the highest point above the anode and the lowest point on substrate,  $T$  the electrode thickness, and  $I$  the initial PEDOT:PSS film thickness.

[24] J.C. Gustafsson, B. Liedberg, and O. Inganäs, *Solid State Ionics* **69**, 145 (1994).

[25] H.W. Heuer, R. Wehrmann, and S. Kirchmeyer, *Adv. Funct. Mater.* **12**, 89 (2002).

[26] D.M. Taylor, D. Morris, and J.A. Cambridge, *Appl. Phys. Lett.* **85**, 5266 (2004).

[27] A.M. Nardes, M. Kemerink, M.M. de Kok, E. Vinken, K. Maturova, and R.A.J. Janssen, *Org. Electron.* **9**, 727 (2008).

[28] B.C. de Brito, E.C.P. Smits, P.A. van Hal, T.C.T. Geuns, B. de Boer, C.J.M. Lasance, H.L. Gomes, and D.M. de Leeuw, *Adv. Mater.* **20**, 3750 (2008).

[29] N.S. Murthy, L.W. Shacklette, and R.H. Baughman, *J. Chem. Phys.* **87**, 2346 (1987).

# Potentiometry on organic semiconductor devices

## Summary

In this thesis, we are interested in the local electrical potential of operational devices based on organic semiconductors. Potential profiles are measured using advanced scanning probe techniques with the final aim to confront experimental data with charge transport and device models. The motivation to do so is that spatially resolved potentials give a true window on the actual *internal* operation of the device, rather than on its mere *external* output.

In order to do so in a quantitative manner, the spatial resolution of the used potential probe needs to be understood in detail. Ideally, one should not only be able to predict the experimental response from a known theoretical prediction, but also to recover the underlying ‘true’ potential profile from an experimental (broadened) profile. The most commonly used probe in this respect is scanning Kelvin probe microscopy, or SKPM, which combines the classical Kelvin probe with atomic force microscopy (AFM). Hence, in the first part of this thesis, we have focused on this technique. In a later chapter, the first steps towards an alternative, scanning tunneling microscope (STM) based potential probing technique are set. The last chapter uses AFM, STM and SKPM to investigate a surprising actuation effect of PEDOT:PSS thin films.

Non-contact potentiometry or scanning Kelvin probe microscopy is a widely used technique to study charge injection and transport in (in)organic devices by measuring a laterally resolved local potential. This technique suffers from the significant drawback that experimentally obtained curves do generally not reflect the true potential profile in the device due to non-local coupling between the probing tip and the device. In Chapter 2 we quantitatively explain the experimental SKPM response, and by doing so directly link theoretical device models to real observables. In particular, the model quantitatively explains the effects of the tip-sample distance and the dependence on the orientation of

the probing tip with respect to the device. This coarse approach requires a very long calculation time.

The performance of organic light emitting field effect transistors (LEFET) is strongly influenced by the width of the recombination zone. In Chapter 3, we present an analytical model for the recombination profile. Assuming Langevin recombination, the recombination zone width  $W$  is found to be given by  $W = \sqrt{4.34d\delta}$  with  $d$  and  $\delta$  the gate dielectric and accumulation layer thicknesses respectively. The model compares favorably to both numerical calculations and measured surface potential profiles of an actual LEFET.

As explained in Chapter 3, in ambipolar organic field effect transistors (oFET) the shape of the channel potential is intimately related to the recombination zone width  $W$ , and hence to the electron-hole recombination strength. However, surface potentials as measured by scanning Kelvin probe microscopy (SKPM) are distorted due to spurious capacitive couplings. In Chapter 4, we develop a (de)convolution method with an experimentally calibrated transfer function to reconstruct the actual surface potential from a measured SKPM response and vice versa. This approach is much faster than the one presented in Chapter 2. Using this scheme, we find  $W = 0.5 \mu\text{m}$  for a nickel dithiolene oFET, which translates into a recombination rate that is two orders of magnitude below the Langevin value.

In Chapter 5, we report a new method for investigating the local electrical properties of organic field effect transistors with potentially unprecedented spatial resolution. In particular, we show that it is possible to perform scanning tunneling microscopy on the channel of an operational pentacene oFET, despite the absence of a conducting substrate. Charge transport from the STM tip to the contacts occurs via a three-step process of vacuum tunneling, followed by vertical transport to the accumulation layer and lateral transport in the accumulation layer.

In Chapter 6, we demonstrate giant out-of-plane actuation of thin films of poly(3,4-ethylenedioxythiophene):poly(styrenesulfonate) (PEDOT:PSS) under ambient conditions. The actuation is driven by an electrical bias and resulting current between interdigitated gold electrodes on glass which are placed below the PEDOT:PSS thin film. We combine current measurements with optical, AFM, SKPM and STM measurements

on spin cast films. The actuation is found to be independent of film thickness and composition and leads to a maximum actuation in the first cycle of 950% for a 21 nm thick film in ambient. Two actuation regimes are identified. In the first regime, reversible redox reactions occur and actuation is mainly due to osmotic effects brought about by an increasing ion concentration on the anode. In the irreversible regime, secondary oxidation reactions occur and mass transport to the anode becomes also important. The independence of the maximally attainable actuation height on channel width and film thickness and on PEDOT:PSS ratio is explained by screening inside the thin film. From the thickness dependence of the potential screening we concluded that the screening length is of the order of tens of nm. Hence, the screening length rather than the film thickness determines the actuation height.

To summarize, we succeeded to resolve the resolution issues associated with scanning Kelvin probe microscopy, thereby enabling a quantitative comparison of measured and modeled surface potentials. The developed tools and insight is applied to the potential in an ambipolar oFET where we used the experimental SKPM response to investigate the recombination zone width  $W$ . As a next step, potentially unprecedented spatial resolution on organic semiconductors might be achieved using scanning tunneling potentiometry. The first step in this direction, stable STM operation on the channel of a working oFET, has been established.



# Potentiometrie op organische halfgeleider devices

## Samenvatting

In dit proefschrift zijn we geïnteresseerd in de lokale elektrische potentiaal van operationele devices op basis van organische halfgeleiders. Potentiaalprofielen zijn gemeten met behulp van geavanceerde scanning probe technieken met het uiteindelijke doel om de experimentele gegevens te vergelijken met ladingstransport- en devicemodellen. De motivatie om dit te doen is dat ruimtelijk opgeloste potentialen een kijk geven op de werkelijke *interne* werking van het device, en niet alleen op zijn *externe* werking.

Om dit op een kwantitatieve wijze te doen moet de ruimtelijke resolutie van de gebruikte potentiaalsensor in detail worden begrepen. Idealiter is men niet alleen in staat om de experimentele respons op een bekende theoretische voorspelling te berekenen, maar ook om het onderliggende 'echte' potentiaalprofiel te reconstrueren uit een experimenteel (verbreed) profiel. De voor dit doel meest gebruikte sensor is scanning Kelvin probe microscopie, of SKPM. Het combineert de klassieke Kelvin probe met atomaire kracht microscopie (AFM). Vandaar dat we in het eerste deel van dit proefschrift deze techniek bestuderen. In een later hoofdstuk worden de eerste stappen gezet op weg naar een alternatieve techniek om potentialen te meten, gebaseerd op scanning tunneling microscopie (STM). Het laatste hoofdstuk maakt gebruik van AFM, STM en SKPM om een verrassend volumeveranderingseffect in dunne PEDOT:PSS films te onderzoeken.

Contactloze potentiometrie of Kelvin scanning probe microscopie is een veel gebruikte techniek om te ladingsinjectie en -transport in (in)organische devices te bestuderen door het meten van lateraal opgeloste lokale potentialen. Deze techniek kampt met het grote nadeel dat experimenteel verkregen curves meestal niet overeenkomen met de echte potentiaalprofielen in het device. Dit is te wijten aan de niet-lokale elektrostatistische koppeling tussen de meetsonde en het device. In hoofdstuk 2 verklaren we kwantitatief de experimentele SKPM respons, en leggen daarmee rechtstreeks

verband tussen theoretische devicemodellen en waarnemingen. In het bijzonder verklaart het model kwantitatief de invloed van de tip-sample afstand en de afhankelijkheid van de oriëntatie van de AFM tip ten opzichte van het device. Deze brute-kracht benadering vereist zeer lange rekentijden.

Het gedrag van organische licht-emitterende veld effect transistoren (LEFET) wordt sterk beïnvloed door de breedte van de recombinatiezone. In hoofdstuk 3 presenteren we een analytisch model voor het recombinatieprofiel. Uitgaande van Langevin recombinatie, blijkt de breedte  $W$  van de recombinatiezone te worden gegeven door  $W = \sqrt{4.34d\delta}$  met  $d$  en  $\delta$  de dikte van het gate-diëlektricum en van de accumulatielaag, respectievelijk. Het model laat zich gunstig vergelijken met zowel numerieke berekeningen als met de gemeten oppervlakte-potentiaalprofielen van een daadwerkelijke LEFET.

Zoals uiteengezet in hoofdstuk 3 is in ambipolaire organisch veld effect transistoren (oFET) de vorm van de kanaalpotentiaal nauw gerelateerd aan de breedte van de recombinatiezone  $W$ , en dus aan de elektron-gat recombinatiesterkte. Echter, de oppervlaktepotentialen zoals gemeten met behulp van scanning Kelvin probe microscopie worden verstoord door ongewenste capacitieve koppelingen. In hoofdstuk 4 ontwikkelen we een (de)convolutiemethode waarin we met een experimenteel gekalibreerde overdrachtsfunctie de werkelijke oppervlaktepotentiaal uit een gemeten SKPM respons kunnen reconstrueren en *vice versa*. Deze aanpak is veel sneller dan die in hoofdstuk 2. Met deze methode vinden we voor een nikkel-dithioleer oFET  $W = 0,5 \mu\text{m}$ , wat zich laat vertalen in een recombinatie-snelheidsconstante die twee ordes van grootte lager is dan de Langevin-waarde.

In hoofdstuk 5 rapporteren we een nieuwe methode voor het onderzoeken van de lokale elektrische eigenschappen van organische veld effect transistoren met potentieel ongekeerde ruimtelijke resolutie. In het bijzonder hebben we laten zien dat het mogelijk is om scanning tunneling microscopie te doen op het kanaal van een werkende pentaceen oFET, ondanks het ontbreken van een geleidende ondergrond. Ladingstransport van de STM-tip naar de contacten gebeurt via een driestaps proces van vacuümtunneling, gevolgd door verticaal transport naar de accumulatielaag en lateraal transport in de accumulatielaag.

In hoofdstuk 6 tonen wij een reusachtig dikteveranderingseffect aan in dunne lagen van poly(3,4-ethyleendioxythiofeen):poly(styreensulfonaat) (PEDOT:PSS) onder atmosferische omstandigheden. De dikteverandering wordt aangedreven door een elektrisch potentiaalverschil en de daaruit voortvloeiende stroom tussen goud elektroden die op het glassubstraat onder de PEDOT:PSS laag zijn geplaatst. We combineren stroommetingen met optische, AFM, SKPM en STM metingen op gespincoate films. De dikteverandering blijkt onafhankelijk te zijn van laagdikte en -samenstelling en leidt in lucht tot een maximum dikteverandering in de eerste cyclus van 950% voor een 21 nm dikke film. Twee dikteveranderingsregimes zijn geïdentificeerd. In het eerste regime treden omkeerbare redoxreacties op en is de dikteverandering voornamelijk het gevolg van osmotische effecten door een toenemende ionenconcentratie op de anode. In het onomkeerbare regime treden secundaire oxidatiereacties op en wordt transport van materie naar de anode ook belangrijk. De onafhankelijkheid van de maximaal haalbare dikteverandering van kanaalbreedte, filmdikte en PEDOT:PSS verhouding wordt verklaard door elektrische afscherming in de dunne film. Uit de dikteafhankelijkheid van de elektrische afscherming komen we tot de conclusie dat de afschermingslengte van de orde van tientallen nm is. Vandaar dat de afschermingslengte in plaats van de laagdikte de maximale dikteverandering bepaalt.

Samenvattend zijn we erin geslaagd om de resolutieproblemen van scanning Kelvin probe microscopie op te lossen, waardoor een kwantitatieve vergelijking van gemeten en gemodelleerde oppervlaktepotentialen mogelijk is. De ontwikkelde gereedschappen en inzichten zijn toegepast op de potentiaal van een ambipolaire oFET. Hierin is de experimentele SKPM respons gebruikt om de breedte van de recombinatiezone te bepalen. In een volgende stap zou een potentieel ongekende ruimtelijke resolutie op organische halfgeleiders kunnen worden gerealiseerd met behulp van scanning tunneling potentiometrie. De eerste stap in deze richting, stabiel STM bedrijven op het kanaal van een werkende oFET, is gezet.



# Acknowledgements

Without the help of a lot of persons, this thesis would not have been as it is. I would like to thank René Janssen for giving me the opportunity to do my PhD in his group and for allowing me to go in many (and sometimes extra) conferences. I want to thank Martijn Kemerink who introduced me in the group in 2005. Under the daily supervision of Martijn I have learnt a lot, sometimes starting from zero in the experimental part, making a research full of challenge but full of beauty. At the beginning, I believed research consisted mainly of making devices, measuring physical values or modeling experimental data. In the end I realized what a huge impact the communication of new ideas through international journals and conferences has. I would like to thank both Martijn and René for discussions we had together, for their criticisms and advices along these years. The team work we have done together is the backbone of this thesis.

For your constructive suggestions in this thesis and for being members of my reading committee I would like to thank Sylvia Speller, Dago de Leeuw and Kees Flipse.

I would like to thank Gerard Wijers for his help in all mechanical issues and his creativity. When I have arrived, the actual UVH STM was a UHV SEM and Auger electron spectroscope. With the help of Martijn, Gerard designed the STM holder and installed the holder for optics and the primary, turbo and ion getter pumps. I would like to thank Wijnand Dijkstra for all cabling and noise problems on the UHV STM. A special thank goes to Peter Nouwens who instructed me how to use the bonding machine.

Since the clean room had no experience in making Au/Ti microstructures, a special thank goes to Barry Smalbrugge who, after a lot of trials such as wet etching, helped me to get the good recipe. I would like to thank Tjibbe de Vries for his help with the MA6 and the profilometer. I would like to thank Erik-Jan Geluk for teaching me how

to use the FC2000 and for the occasional SEM pictures. I would like to thank all three and the COBRA institute for letting me the freedom to prepare substrates.

The organic materials were deposited in chemistry department. I would like to thank both Alexandre Nardes and Martijn Wienk who instructed me how to deposit the PEDOT:PSS thin films and the pentacene layers. I would like to thank Jan Gilot and Stefan Oosterhout for their occasional help. Related to PEDOT:PSS, a special thank goes to Lukas Brinek who helped us during 6 months to elaborate new experiments.

Philips also played an important role in this thesis via different persons. I would like to thank Paul van Hal, Margreet de Kok and Bea Langeveld for materials supply. I would like to thank Edsger Smits and Dago de Leeuw for the collaboration on the ambipolar transistors. My roommate, Simon Mathijssen, is thanked for giving expertise in our home built oFETs and for discussions on SKPM.

I would like to thank Klára Maturová who let me occasionally use the glovebox. We shared a RHK controller and the same electronic problems. Joris Hagelaar, Jiří Červenka, Erwin Rossen, Kevin van de Ruit, Muriel Sicot and Oleg Kurnosikov are thanked for discussions related to the home built STM. Reinder Coehoorn and Edwin Jager are thanked for interesting discussions on transfer function and osmosis. I would like to thank Erik Roeling for the good time we spent in clean room, in chemistry (sometimes late in the evening), in San Francisco and for sharing the probe station. It is always nice to talk about everything (job interviews, cycling, California, politics...). I would like to thank all the other M2N colleagues / roommates through the years: Hans Gommans, Marta Fonrodona, Yingxin Liang, Rein Rumphorst, Wijnand Germs, Ron Willems, Siebe van Mensfoort, Rik van Laarhoven, Nick Podaru, Juan Amir, Kees Flipse, Ondřej Zháněl, Marco Carvelli, Rein de Vries. Through Friday morning group meetings, coffee and lunch breaks with crazy discussions, football tournaments with broken nails, making movies (from South Park theme to running ashore on a lost island) and other parties, the life of the group was really active. To all I really appreciated your help and friendship.

Finally, I would like to thank my parents for their encouragement and understanding. They always accepted my choices although the distance separating us is significant. My sister, Laetitia, thank you for the moral support. Anca, thank you for your support during these years. You have been always there to help me in everything.

Dimitri



# Curriculum Vitae

September 25, 1980 Born in Privas, France.

1998 Scientific Baccalaureate, Lycée Astier, Aubenas, France.

1998 – 2004 M. Sc. in Applied Physics, Université Joseph Fourier, Grenoble, France.

Traineeship at the Philips Research Laboratories, Eindhoven, The Netherlands. Subject: *Archival life study of phase-change optical discs*, supervised by dr. L. van Pieterse.

Traineeship at the Laboratoire de Cristallographie, Grenoble, France. A collaboration with Nexans-Superconductors GmbH, Hurth, Germany. Subject : *Synthesis and characterization of buffer layers CeO<sub>2</sub> in coated superconductors*, supervised by dr. P. Odier and dr. D. Isfort.

Master thesis project at the Laboratoire de Spectrométrie Physique, Grenoble, France. Subject : *Optical detection of single molecules and nanocrystals using a confocal microscope*, supervised by dr. J. Woehl and dr. S. Huant.

2005 – 2009 PhD project at the group of Molecular Materials and Nanosystems (M2N), department of Applied Physics, Eindhoven University of Technology, Eindhoven. Subject: *Potentiometry on organic semiconductor devices*, supervised by dr.ir. M. Kemerink and prof.dr.ir R.A.J. Janssen.



# List of publications

D.S.H. Charrier, M. Kemerink, B.E. Smalbrugge, T. de Vries, R.A.J. Janssen, Real versus measured surface potentials in Scanning Kelvin Probe Microscopy, *ACS Nano*, **2** (4) 622-626, 2008.

M. Kemerink, D.S.H. Charrier, E.C.P. Smits, S.G.J. Mathijssen, D.M. de Leeuw, R.A.J. Janssen, On the width of the recombination zone in ambipolar organic field effect transistors, *Appl. Phys. Lett.*, **93** (3) 033312, 2008.

K. Maturova, M. Kemerink, M.M. Wienk, D.S.H. Charrier, and R.A.J. Janssen, Scanning Kelvin Probe Microscopy on Bulk Heterojunction Polymer Solar Cells, *Adv. Funct. Mater.*, **19**, 1-8, 2009.

D.S.H. Charrier, T. de Vries, S.G.J. Mathijssen, E.-J. Geluk, E.C.P. Smits, M. Kemerink, R.A.J. Janssen. Bimolecular recombination in ambipolar organic field effect transistors, *Org. Electron.*, **10**, 994-997 (2009).

D.S.H. Charrier, M. Kemerink, R.A.J. Janssen, Giant out-of-plane ambient actuation of poly(3,4-ethylenedioxythiophene) : poly(styrenesulfonate) thin films, submitted.

D.S.H. Charrier, M. Kemerink, R.A.J. Janssen, Scanning tunneling microscopy via the accumulation layer of *p*-type organic field effect transistors, in preparation.